Project No. 12-3541

Accelerated Irradiations for High Dose Microstructures in Fast Reactor Alloys

Reactor Concepts Research Development and Demonstration

Zhijie Jiao
University of Michigan

William Corwin, Federal POC
Meimei Li, Technical POC

Final Technical Report
COVER PAGE

Federal Agency to which Report is submitted: DOE NE – Nuclear Energy University Program

Recipient: University of Michigan
Award Number: DE-AC07-05ID14517
Project Title: Accelerated Irradiations for High Dose Microstructures in Fast Reactor Alloys
Project Period: September 1, 2012-December 31, 2016

Principle Investigator: Zhijie Jiao, University of Michigan, zjiao@umich.edu, 734-615-7761
Report Submitted by: Zhijie Jiao, University of Michigan, zjiao@umich.edu, 734-615-7761

Date of Report: March 31, 2017
Covering Period: September 1, 2012-Decemeber 31, 2016
Report Frequency: Annually

Working Partners: Gary Was, University of Michigan, gsw@umich.edu
Emmanuelle Marquis, University of Michigan,
Roger Stoller , ORNL
David Hoelzer, ORNL
Stuart Maloy, LANL
Mychailo Toloczko, PNNL

Cost-Sharing Partners: NA

DOE Project Team: DOE TPOC – Meimei Li
DOE Federal POC – William Corwin

Signature of Submitting Official:

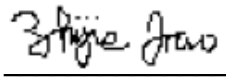

(electronic signature is acceptable)

ACCOMPLISHMENTS

Project Objective: The objective of this project is to determine the extent to which high dose rate, self-ion irradiation can be used as an accelerated irradiation tool to understand microstructure evolution at high doses and temperatures relevant to advanced fast reactors. We will accomplish the goal by evaluating phase stability and swelling of F-M alloys relevant to SFR systems at very high dose by combining experiment and modeling in an effort to obtain a quantitative description of the processes at high and low damage rates.

Project Goals:
1) A direct comparison between high dose rate ion and neutron irradiation using the same heats, 2) microstructure evolution of F-M alloys at high doses including advanced alloys NF616 and 14YWT ODS, and 3) fundamental understanding of the prospect of using ion irradiations to emulate neutron irradiation microstructures by a combination of experimental and modeling work.

Executive Summary

The objective of this project is to use high dose rate, self-ion irradiation as an accelerated irradiation damage tool to understand microstructure evolution in ferritic-martensitic (F-M) alloys at high doses and temperatures relevant to advanced fast reactors. One challenge of self-ion irradiation is the shallow irradiation depth and dose variation with irradiation depth. Techniques were developed to accurately analyze the microstructure of irradiated specimens at the targeted irradiation using a combination of focused ion beam (FIB) lift-out analysis and scanning transmission electron microscopy (STEM). A challenge in the program was carbon uptake during ion irradiation, which appears to be an outstanding problem in accelerator laboratories worldwide. The carbon uptake issue was mitigated by surface coating with ~100 nm alumina.

Ferritic-martensitic alloys including HT9, T91, NF616 and 14YWT were irradiated up to 450 dpa at a temperature range of 400-480°C using 5 MeV Fe^{++} to investigate their swelling behavior at high damage levels. The irradiated microstructure including cavities and precipitates was characterized. It was found that swelling was greatly affected by irradiation temperature with a peak around 460°C with much lower swelling at 440°C and 480°C and no swelling at 400°C and 420°C for HT9. The swelling curve as a function of temperature is consistent with literature and theory which have shown that the curve is typically bell-shaped. F-M alloys did not vary significantly in their swelling behavior at 460°C, although NF616 showed less swelling than T91 and HT9 at the same irradiation dose. The swelling rates at 460°C up to 450 dpa for the three alloys were in the range of 0.01-0.03 %/dpa, much lower than the hypothesized ultimate swelling rate of 0.2%/dpa in F-M alloys. G-phase precipitates were found to be the major irradiation-induced phase in HT9 and they were not found to be affected by the implanted helium level. No significant change of ODS particles was observed in 14YWT after irradiation at 400°C to 250 dpa by atom probe tomography. The oxygen content in the ODS particles appeared to decrease after irradiation to 80 dpa at 420°C. Segregation N, C, and P to grain boundaries were also revealed in 14YWT after ion irradiation.

The effect of pre-implanted helium on swelling behavior was also investigated in ferritic-martensitic steels HT9, T91 and NF616. 10 appm helium pre-implantation resulted in higher swelling and swelling rate than 1 appm helium pre-implantation in all three alloys irradiated at 460°C. Analysis of the contribution of void size and density to swelling at different damage levels suggested that the higher swelling and swelling rate in samples with 10 appm helium pre-implantation are mainly due to the higher number of voids nucleated. T91 was studied with a broader helium pre-implantation levels (0, 1, 10, 100 and 1000 appm) at 460°C. This study systematically varied the pre-implanted helium content in T91 to gain a more fundamental understanding of its role on both nucleation and the swelling rate. 10 appm helium showed highest swelling at low dose of 50 dpa. However, after further irradiation, the 0 appm He case overtook the higher He cases and showed the highest swelling. The 100 appm and 1000 appm helium cases showed very low swelling and swelling rate even at high dose. It appeared that suppression of void growth occurred at high helium levels due to a substantially increased bubble/void density.

Irradiated microstructure was compared to neutron irradiation to see how well self-ion irradiation can be used to mimic neutron irradiation. Based on comparison of the irradiated microstructures including dislocation loops, G-phase precipitates and voids, Fe^{++} irradiation at 460°C:188 dpa with 1 appm helium was found to yield the best overall microstructure agreement with the FFTF irradiation at 443°C:155 dpa in HT9. The temperature shift for ion irradiation to emulate reactor irradiation appears to be ~20°C for HT9. Temperature shift in T91 appeared to higher at about 30-50°C. The moderate temperature shift compared to that in austenitic stainless steels (>100°C) is believed to be linked to the high sink density in F-M alloys.

Cluster dynamics modeling was performed in simulated F-M alloys to investigate the peak swelling temperature and the temperature shift for high dose rate self-ion irradiations. The experimentally observed peak temperature could not be simulated by implementation of a simple Frenkel pair model. By addition of cascade damage and helium cogeneration, the resulting temperature distributions were much closer to the experimentally observed peaks at 420-460˚C in the ion-relevant case. The shift in temperature by modeling (~150°C), however, remains much larger than the experimentally observed 20-60˚C in F-M alloys.

Additionally, the phenomenon of carbon uptake during ion irradiation was discovered and it played a significant role in suppressing the nucleation of cavities, and thus the swelling was reduced as well. The effect of helium on swelling was shown to be affected by the presence of excess of carbon in the matrix by cluster dynamics modeling. In the case of carbon uptake, the swelling peak in T91 at 460°C appeared to be at 10 appm helium while without carbon uptake the swelling peak shifted to 0 appm at high doses.

This project has successfully emulated the neutron irradiated microstructure at high doses in F-M alloys using self-ion irradiations by adjusting irradiation temperature and the amount of pre-implanted helium. It has also demonstrated the importance to select the appropriate irradiation temperature, helium content, as well as to avoid carbon uptake when attempting to use ion irradiation as a surrogate for neutron irradiation.

1. Introduction

Understanding microstructure development in materials irradiated to high dose is, in a sense, the holy grail of materials performance in reactor systems. Fast reactor ducts will likely see damage levels of 200 dpa, and for the Traveling Wave Reactor to become a reality, the clad and some structural materials must withstand ~600 dpa. A prime difficulty in studying high dose microstructures is that test reactors cannot reach this damage level in reasonable time frames or at manageable costs. Water-based test reactors (ATR, HFIR) can provide ~3-5 dpa/yr level. Fast reactors accumulate damage more quickly but are limited to ~20 dpa/yr. Because of the low dose rate and high cost, the existing library of neutron-irradiated samples at high dose is extremely limited, making a systematic study of microstructure evolution at high dose nearly impossible. However, information on material response at high dose is very much needed to guide the development and selection of advanced irradiation-resistant alloys. As such, only ion irradiation is capable of providing the required levels of damage in reasonable time frames with negligible cost compared to neutron irradiations. Yet ion irradiation suffers from two potential drawbacks; the volume of irradiated material, and the relatively unknown effect of high damage rate on the resulting microstructure. Micro-sample fabrication and testing, while not a replacement for bulk property determination, holds the promise for minimizing the drawback of limited irradiated volume for property determination [1.1]. The capability of high damage rates to produce microstructures relevant to reactor conditions remains the greatest challenge. That is, can very high damage rates be used to explore the high dose microstructures that are relevant to fast reactor conditions?

The primary result of irradiation is the production of vacancies and interstitials. The key process that ultimately determines the irradiated microstructure is the preferential absorption of one defect over the other at sinks (grain boundaries, dislocations, etc). For instance, preferential absorption of interstitials at sinks will leave excess of vacancies in the matrix, leading to the formation of vacancy-type dislocation loops or voids. However, vacancy-interstitial recombination will not contribute to the microstructure thus lessen the impact of irradiation. The production rate of interstitials and vacancies is much higher at high dose rate (as is the recombination rate) but if the relative ratio of recombination rate and preferential absorption rate at sinks can be maintained, a microstructure comparable to that at low damage rate can be obtained. This typically can be done by increasing the irradiation temperature to enhance diffusion of defects to sinks. Guidance on determination of this temperature shift was provided by Mansur [1.2] in the form of invariance relations. These relationships have been used to underpin several recent studies [1.3-1.5] using proton irradiation (dose rate of ~10^{-5} dpa/s) to study neutron irradiation (dose rate of ~10^{-7} dpa/s) in metals at doses ≤ 10 dpa, in which damage rate enhancements of ~100x were shown to result in very similar microstructures and microchemistry if conducted at a temperature increment of 40-80°C. Recent work [1.6] also showed that dose rate enhancements of the order of 1000x can result in very similar swelling if conducted at a temperature increment of ~100°C in *austenitic stainless steels*.

For ferritic-martensitic alloys, evidence has shown that a considerably *smaller temperature shift* is needed compared to austenitic alloys. For instance, the peak swelling temperature of HT9 using heavy ions is ~450°C [1.7], which is similar to the peak swelling temperature of F-M steels irradiated in a fast reactor. Our preliminary work shows that radiation-induced precipitates also follow a much smaller temperature shift. Figure 1.1 compares the size and density of Ni/Si- rich precipitates formed at 10^{-3} dpa/s (proposed high dose rate) to those formed at 10^{-5} dpa/s in alloy T91. Compared to 400°C:7dpa irradiation at 10^{-5} dpa/s, high dose rate irradiation at the same irradiation temperature but to a higher dose of 30 dpa produced comparable precipitate size at slightly lower density. High dose rate irradiation at 440°C induced larger precipitates at a much lower density, indicating that even a modest of 40°C temperature increment appears too large for the 100x damage rate change. The absence of radiation-induced precipitates at high dose rate and 7 dpa implies a larger incubation dose at high dose rate. Experiments conducted on model reactor pressure vessel (RPV) alloys using neutron, electron and proton irradiation at very different dose rates (10^{-10}, 10^{-9}, 10^{-7} dpa/s, respectively) but at the same temperature (300°C) all showed nearly identical irradiation hardening at the same damage levels. [1.8] These data are consistent with a much lower temperature increment in ferritic and F-M steels vs. austenitic steels for equivalent dose rate acceleration. The reason for the small temperature shift in F-M alloys is the very high sink density in these materials. Even before irradiation, the starting microstructure of F-M steels contains a much higher sink density by virtue of fine microstructural features such as lath boundaries, subgrain boundaries (low angle grain boundaries within the lath), packet boundaries, prior austenite boundaries and numerous carbides and nitrides, and irradiation-induced loop formation adds to the sink density. The high sink density significantly reduces the temperature shift at high dose rates. Figure 1.2 shows a calculation of grain boundary composition change vs. dose rate using rate theory for the cases of a low sink density alloy (equivalent to solution annealed austenitic stainless steel) vs. a high sink density (F-M) steel. Note that in the high sink density case, the dependence of segregation on damage rate dependence disappears. Thus, microstructure evolution becomes independent of dose rate as predicted by Mansur [1.2] and shown for void swelling by Garner [1.9,1.10] among others. Rather, the challenge with high dose rate irradiations is that the incubation period is likely to be dose rate dependent. Figure 1.3 suggests that swelling will eventually reach the steady-state swelling rate regardless of dose rate, but the dose to reach this state is dependent on dose rate. Therefore, understanding the incubation dose is critical in applying high dose rate irradiation to emulate low dose rate neutron irradiations.

Whether high dose rate ion irradiations can produce the same type of precipitates as those in low dose rate neutron irradiations raises another concern. Precipitation can be either radiation induced or enhanced. Preliminary work has shown that both types of precipitates can be emulated by ion irradiations. Atom probe tomography (APT) examination of F-M alloy HCM12A irradiated in ATR to 3 dpa at 500°C shows the co-existence of two types of precipitates: radiation-induced Ni/Si-rich precipitates and radiation-enhanced Cu-rich precipitates (Figure 1.4a). Both types of precipitates are also found in the same heat of alloy following proton irradiation (Figure 1.4b) and Fe^{++} irradiation (Figure 1.4c) at the same temperature. Note that the spatial correlation of these two types of precipitates is also faithfully reproduced by ion irradiations.

In both LWR and SFR irradiation conditions, RIS and loop microstructure evolve and saturate quickly (<10 dpa) [1.11]. The void and phase microstructures are slower to develop and, as such, will be the key elements controlling microstructure evolution at high dose. In particular, phase stability, in the form of radiation-induced precipitation and precipitate dissolution/growth, is expected to be a key process impacting the integrity of cladding and structural material at high doses. Radiation-induced precipitation could lead to hardening, embrittlement, loss of protective solute and enhanced corrosion. Similarly, void formation results in dimensional instability and the generation of component stresses. Thus, for fast reactor core materials, the most important processes governing their high dose behavior are void swelling and radiation-induced precipitation, and will be the focus of this study.

The objective of this project is to determine the extent to which high dose rate, self-ion irradiation can be used as an accelerated irradiation damage tool to understand microstructure evolution at high doses and temperatures relevant to advanced fast reactors. Swelling and phase stability at very high doses (up to 500 dpa) in candidate reactor structural and duct materials (including both legacy (T91 and HT9) and advanced (ODS and NF616) ferritic-martensitic (F-M) steels) will be evaluated. Incubation doses for swelling and precipitation as well as swelling rate at high doses will be evaluated and results will be compared to those available from neutron irradiations. Experiments will be coupled with modeling to understand the effect of high dose rate on incubation dose and microstructure evolution at high doses.

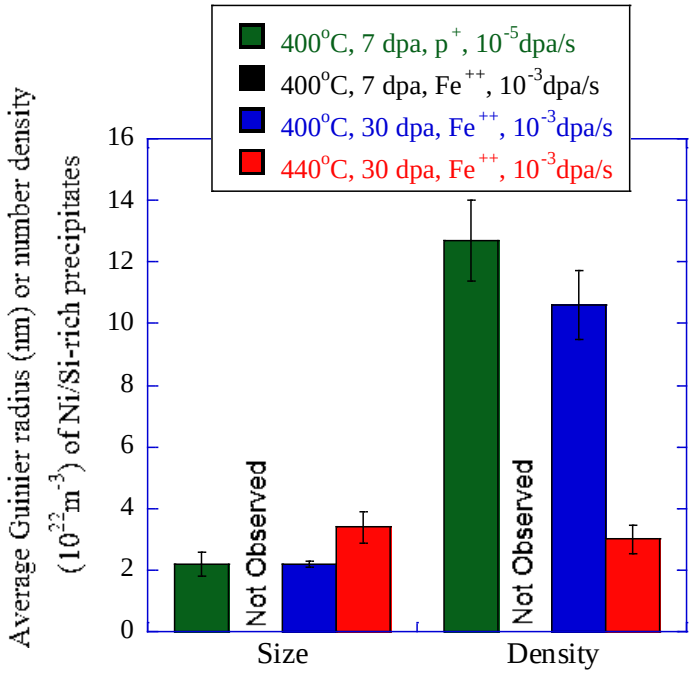

Figure 1.1. Comparison of average size and number density of radiation-induced Ni/Si-rich precipitate by APT in T91 irradiated at 400°C, and 440°C using protons (10^{-5} dpa/s) and Fe^{++} (10^{-3} dpa/s).

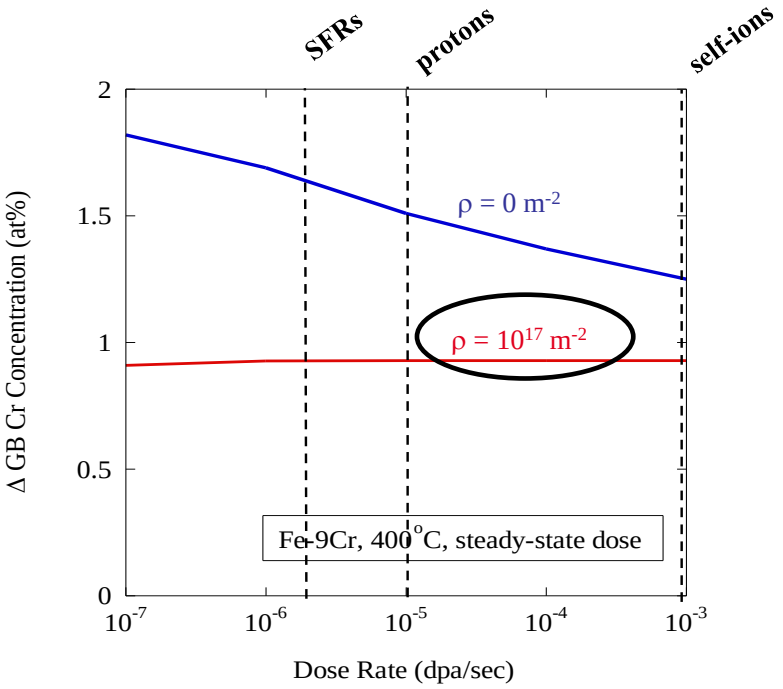

Figure 1.2. Effect of sink strength, as measured by equivalent dislocation density, ρ, on grain boundary RIS over a large dose rate range.

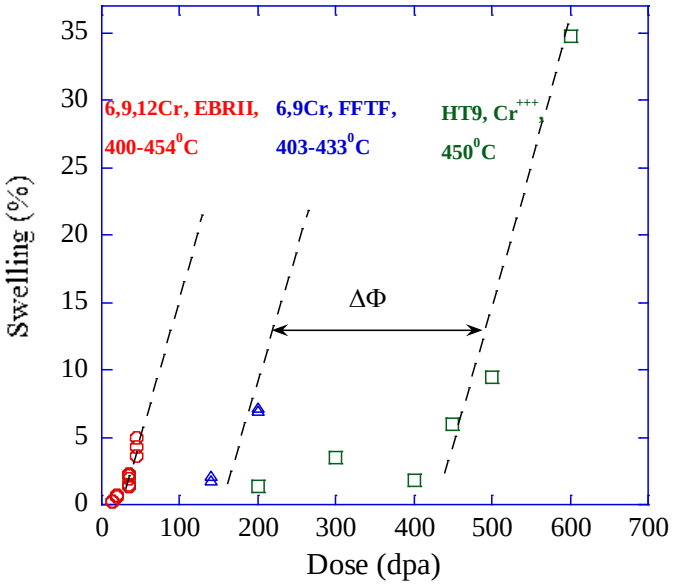

Figure 1.3. Insensitivity of steady-state swelling rate and strong dependence of incubation dose on dose rate [data from refs 1.7,1.9,1.10].The dashed lines indicate the 0.2%/dpa swelling rate at high dose. The difference in incubation dose between heavy ion irradiation and irradiation in FFTF is shown as ΔΦ.

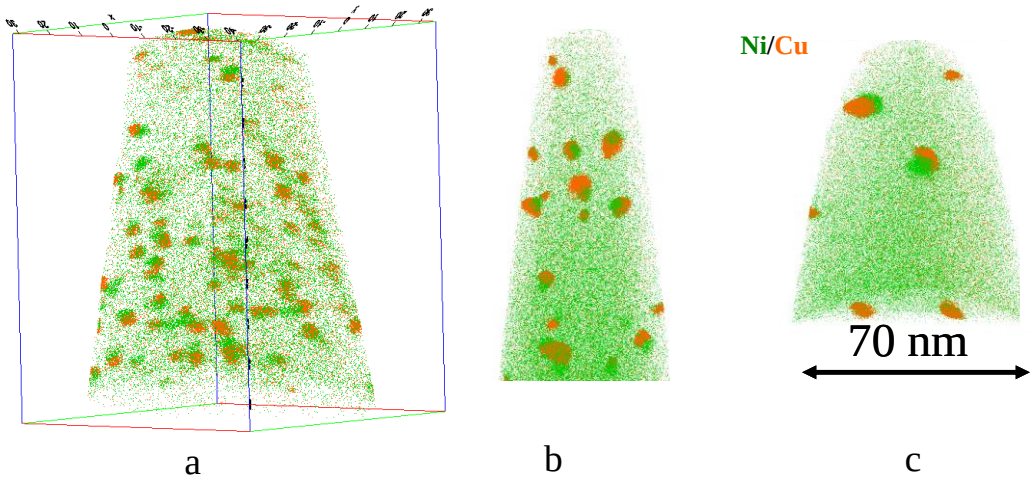

Figure 1.4. APT atom maps showing radiation-induced Ni/Si-rich (green) and radiation-enhanced Cu-rich (orange) precipitates in F-M alloy HCM12A following 500°C irradiation: (a) in ATR to 3 dpa (b) proton irradiation to 7 dpa (c) Fe^{++} irradiation to 100 dpa.

References:

1.1. P. Hosemann, C. Vieh, and S.A. Maloy et al. J. Nucl. Mater. 389 (2009) 239.
1.2. L. K. Mansur, J. Nucl. Mater. 206 (1993) 306.
1.3. L. Tournadre, et al.2011 TMS Annual Meeting, MPIM Symposium, San Diego CA., Mar. 2011.
1.4. G. S. Was, J. T. Busby, T. Allen, E. A. Kenik, et al. J. Nucl. Mater. 300 (2002) 198-216.
1.5. B.H. Sencer, G.S. Was, and F.A. Garner et al. J. Nucl. Mater. 323 (2003) 18.
1.6. A.S. Kalchenko, V.V. Bryk, and F.A. Garner et al, J. Nucl. Mater. 399 (2010) 114.
1.7. V.V. Bryk, A.S. Kalchenko, and F.A. Garner et al., unpublished work.
1.8. G.S. Was, M. Hash and G. R. Odette, Phil. Mag., 85, No. 4-7 (2005) 703-722.
1.9. F.A. Garner, V. V. Bryk, V. N. Voyevodin, paper #15-021, ICFRM-15, Charleston, SC, Oct. 2011.
1.10. F. A. Garner, M. B. Toloczko, B. H. Sencer, J. Nucl. Mater. 276 (2000) 123.
1.11. G.S. Was and J.T. Busby, Philos Mag. 85 (2005) 443.

2. Experiment

2.1 Alloys

Four alloys were used in this project, including T91, HT9, NF616 and 14YWT. Alloy T91 heat 30176 was provided by PNNL. Alloy HT9 (heat 84425, the ACO-3 duct) was received from TerraPower and it was originally from LANL. Alloy 14YWT heat SM10 was prepared at ORNL. Alloy NF616 was from University of Wisconsin which was made at ORNL. The compositions as well as the heat treatment history are given in Table 2.1.

T91

Two pieces of T91 heat 30176 with dimensions of 25 mm × 25 mm × 3 mm were prepared at PNNL and sent to University of Michigan for ion irradiations. The two pieces were cut from T91 heat 30176 and were heat-treated to match the thermomechanical treatment (TMT) of this same heat of material that was used for high neutron dose irradiation studies in FFTF/MOTA. The two pieces were encapsulated in quartz tube that was evacuated and then backfilled with 1/4 atmosphere of helium. The pieces were then normalized at 1038°C for 30 minutes and air cooled. Tempering was performed at 760°C for 30 minutes and then air cooled. The countdown for the heat treating began when the temperature of a thermocouple touching the quartz tube came within 5°C of the target temperature.

A different heat of T91 (C2269) obtained from American Alloy steel was also used in this study because of the limited material for heat 30176. This heat was normalized at 1066°C for 46 minutes and air cooled. Tempering was performed at 790°C for 42 minutes then air cooled.

14YWT

The 14 YWT-SM10 heat sample was prepared at ORNL. The material received from ORNL was not fully decanned. The 14YWT material sample was partially surrounded by the mild steel. Processing of 14YWT involves mechanical alloys, followed by extrusion and annealing.

HT9

The HT9 (heat 84425) was used to construct the ACO-3 hexagonal duct. The samples were received from TerraPower as 1.5mmx1.5mmx20mm bars and the material was originally from LANL. The HT9 duct was subjected to a heat treatment involving 1038°C/5 min/air cooling followed by 760°C/30 min/air cooling.

NF616

NF616 was obtained from University of Wisconsin and it was originally made at ORNL. The alloy was normalized at 1070°C / 2h/air cooling followed by 770°C/2h/air cooling.

Table 2.1. Compositions of T91, HT9 , 14YWT and NF616. The heat numbers are shown in the parenthesis.

Alloy	C	N	Al	Si	P	S	Ti	V	Cr	Mn	Ni	Cu	Nb	Mo	W	Others
T91 (30176)	.08	.054	-	.11	-	-	-	.21	8.6	.37	.09	-	.072	.89	-	
HT9 (84425)	.21	.006	.03	.21	.008	.003	<.01	.33	11.8	.50	.51	-	-	1.03	.24	
14YWT (SM10)	.065	.131	.02	.04	.003	.004	.24	-	13.19	.06	.03	.01	-	-	1.9	Y:.2, O:.173
NF616	.109	-	.005	.102	.012	.003	-	.194	8.82	.45	.174	-	.064	.468	1.87	O: .0042
T91 (C2269)	.10	.048	.022	.28	.009	.003	-	.22	8.37	.45	.21	.17	.076	.9	-	

T91 (30176)	(1) Normalizing 1038^{o}C x 30 min, air cooled (AC); (2) Tempering 760 ^{o}C x 30 min, AC
HT9	(1) Normalizing 1038^{o}C x 5 min, AC; (2) Tempering 760^{o}C x 30 min, AC
NF616	(1) Normalizing 1070^{o}C x 2 h, AC; (2) Tempering 770^{o}C x 2 h, AC
T91 (C2269)	(1) Normalizing 1066°C x 46 min, air cooled (AC); (2) Tempering 790 °C x 42 min, AC

2.2 Self-ion irradiation

Sample Preparation

Prior to irradiation, samples of each alloy were cut in the form of 1.5 x 1.5 x 20 mm bars using electro-discharge machining. The bar samples were then mechanically polished using successively lower grits of silicon carbide grinding paper from 240 to 1000 grit. Diamond slurries of 1 μm and 0.25 μm were used for a final polish, providing a mirror-like finish on the samples. To remove the damage layer induced during mechanical polishing, the samples were then electropolished. The electropolishing solution consisted of a 10% perchloric acid, 90% methanol solution which was cooled to between -40 and -50°C using a methanol bath and liquid nitrogen or dry ice. The samples were electropolished at an applied voltage of -40V for approximately 20 seconds. A magnetic stirrer rotating at 650 rpm was used to create a vortex which impacted the surface of the sample head on. This procedure was estimated to remove about 2 μm of material from the sample surface.

For some experiments, a coating of alumina was applied to the surface of the samples to prevent carbon uptake during ion irradiation. An ALD (atomic layer deposition) machine was used to apply the coating at a thickness of 100 nm.

For samples with helium pre-implantation, the implantation was conducted using a 400 kV implanter. Various energies ranging from 80 keV to 420 keV were used to achieve an approximately flat helium profile within the depth of 300-1000nm. The helium levels for experiments in this project included 0, 1, 10 100, and 1000 appm. Figure 2.1 shows the helium implantation profile overlaid with the expected damage profile (using 5 MeV Fe^{2+} ions). Since the damage rate changes with depth, it was necessary to choose a particular depth for the microstructural analysis. A depth of 600nm was chosen for the nominal damage rate for data taken from the 500-700nm depth range. This range avoids any effects due to the surface, due to injected interstitials, and is within the bounds of the desired helium level.

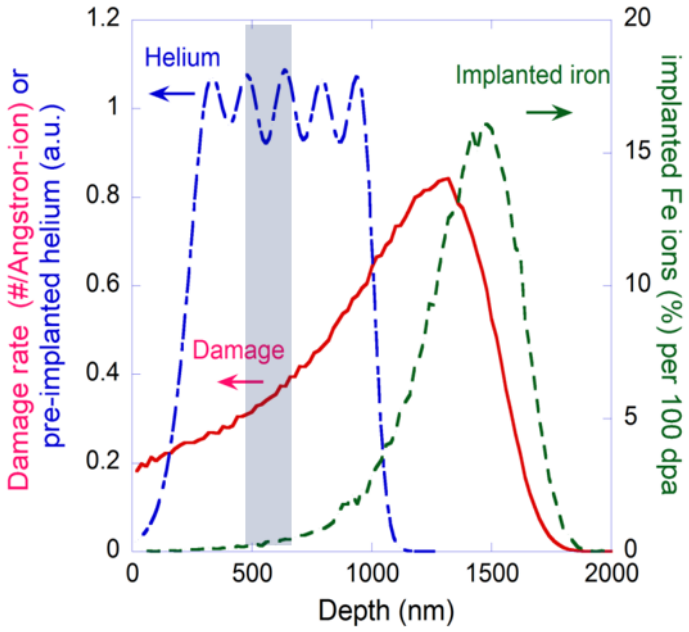

Figure 2.1. The helium implantation profile (blue) is overlaid with 5 MeV self-ion damage (red) and injected interstitial profiles (green)

Ion Irradiation Experiment

After helium implantation, samples were loaded onto an irradiation stage. A schematic of the stage is shown in Figure 2.2. The stage was designed with a nickel head to conduct heat from a cartridge heater mounted in the back of the stage. A 0.25mm thick copper foil was placed on the head to conduct heat between the samples and the stage. The samples were then aligned side-by-side on the stage and held in place using a pair of hold-down bars and a shim which tightened into the stage using screws. Extra dummy samples, called guide bars, were placed to bookend the irradiation samples of interest. Two thermocouples were then spot-welded onto the guide bars. Figure 2.3 shows an image of a completely built stage prior to irradiation.

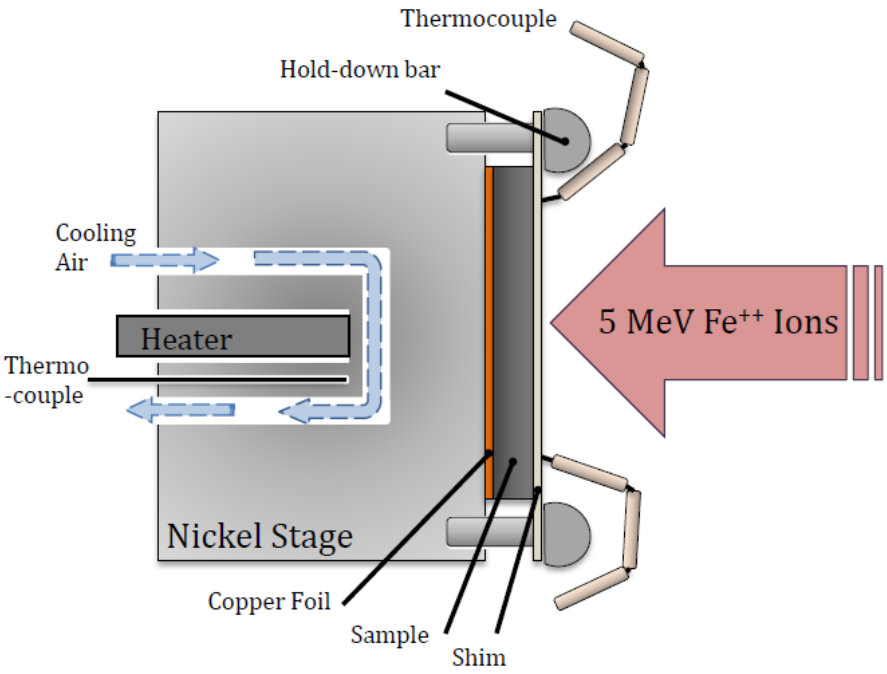

Figure 2.2. A schematic of the Nickel irradiation stage.

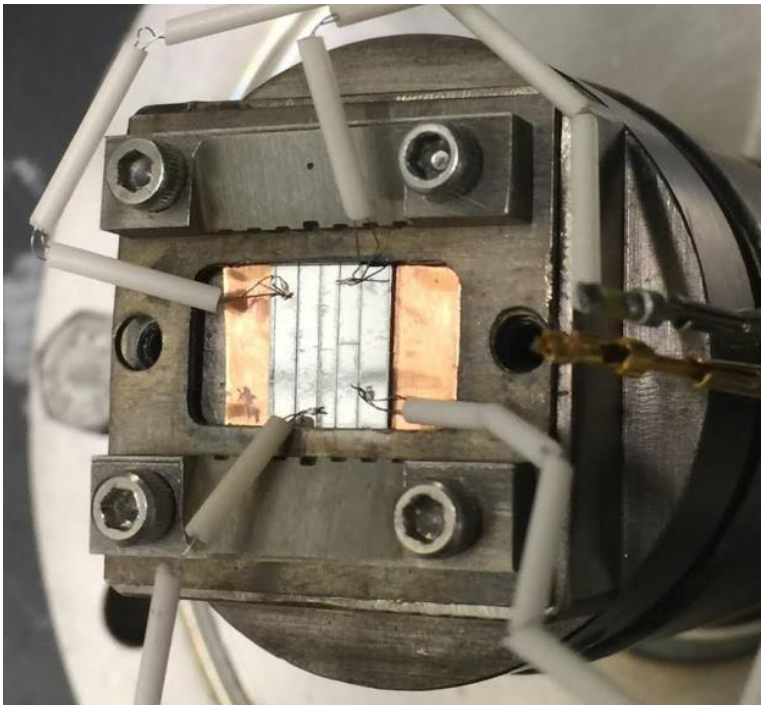

Figure 2.3. An image of a fully constructed irradiation stage.

After construction, the stage was then mounted on the end of a beamline. A laser was used to align the target irradiated area with the samples, and an aperture slit system was used to define

the area. The diagnostics on the beamline included a 2-D FLIR thermal imager to monitor in-situ temperature, ion gauges to monitor pressure, and faraday cups to monitor the current in the beamlines. The irradiation chamber was pumped down to a pressure of $<1x10^{-7}$ torr over the course of about 24 hours prior to irradiation. Additionally, the chamber was baked out at about 220°C for 12 hours. If the samples were not previously irradiated, they were outgassed at the irradiation temperature for approximately 4 hours.

The samples were irradiated with either 5 MeV or 4.4 MeV Fe^{2+} ions, depending on whether the 3 MV Pelletron accelerator was used or the 1.7 MV Tandem. During irradiation, the temperature was controlled using a cartridge heater in conjunction with cooling air through an airflow channel in the back of the stage. The voltage on the heater and the pressure of the cooling air could be controlled on a fine scale, allowing for overall temperature control during irradiation of ±10°C. A 2-D thermal imager was used to monitor the temperature on the surface of the samples during the experiment. The specific AOIs (areas of interest) on the samples were created in the software program and calibrated using the thermocouples either during the outgassing procedure, or just prior to irradiation. The pressure near the stage was maintained in the $1 \times 10^{-8} - 1 \times 10^{-7}$ torr range. The irradiation damage level was measured by periodically (every 30 – 40 minutes) inserting a faraday cup into the beam, just before the stage. The equation below shows how the total irradiation time was calculated, along with their appropriate units. The faraday cup measurement correlated to the "current on specimens" reading, which was time-averaged.

$$\frac{(\text{Desired DPA}) * (\text{Number Density}) * (\text{Ion Charge}) * (\text{Specimen Area Irradiated})}{(\text{Current on Specimens}) * (\text{Damage Rate})} = \text{Irrad. Time}$$

$$\frac{[\text{disp/atom}]* [\text{atom/cm}^3]* [\text{C/ion}] * [\text{uC/C}]* [\text{cm}^2]}{[\text{uA}]* [\text{disp/ion-angstrom}] *[\text{angstrom/cm}]} = [\text{seconds}]$$

Once the desired damage level had been achieved, the irradiation was terminated by inserting a faraday cup to block the beam, reducing the heater voltage to 0, and running the cooling air at high pressure. Using this method, the samples were typically able cool to below 100°C within 10 minutes.

Characterization of ion irradiated samples

Due to the shallow depth of penetration of ion irradiation, thin foils needed to be extracted from the surface of the samples to analyze the irradiated microstructure. An FEI Helios, Nova, or Quanta dual-beam focused ion mill was used to create the samples. A layer of platinum was deposited onto the irradiated surface, and trenches were milled out such that a sample of the surface could be extracted using an Omniprobe device. The extracted lamella was then thinned to at least 100nm in thickness as to be electron transparent in the TEM. Figure 2.4 shows a diagram of the FIB process and a resulting image from the TEM.

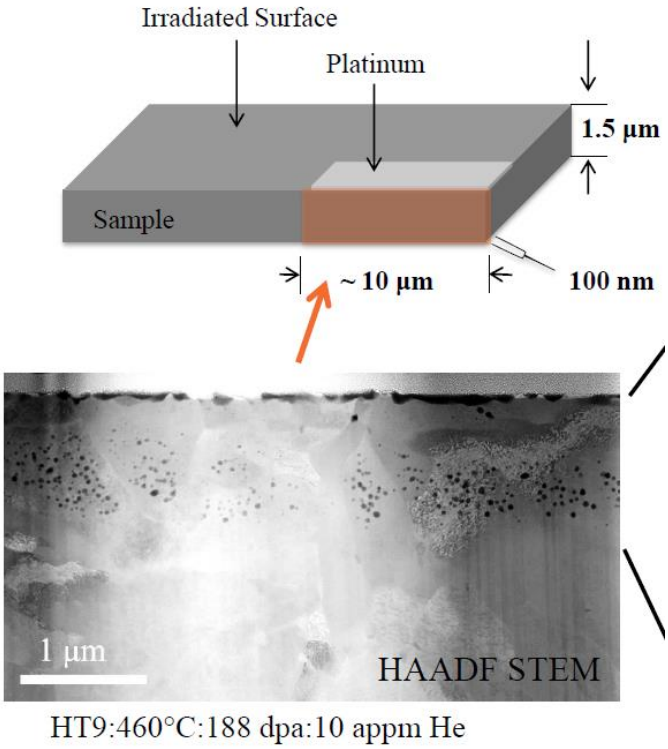

Figure 2.4. A schematic of the FIB process and a resulting HAADF image taken from the JEOL 2100F.

A 200kV JEOL 2100F TEM/STEM was used to image the irradiated foils. A combination of bright field STEM (scanning mode) and high angle annular dark field (HAADF) STEM was used to image cavities, dislocations, and precipitates in the irradiated microstructure. HAADF images derive their contrast mainly from Z-contrast (atomic number). These images provided the best contrast for cavity imaging due to the lack of material present in them. HAADF images were used to profile and count the cavities. Images were taken across each liftout and at least two liftouts were created for each condition studied in this project. Additionally, the thickness of each liftout was measured using EELS (electron energy loss spectroscopy). Each image was then profiled with depth, divided into 100nm deep bins. The cavities in each bin were sized and counted. An estimation of the swelling at each depth was obtained using the sum of the volume of all cavities in each bin. The swelling percentage was calculated as $\Delta V/V$, where ΔV was taken as the sum of the cavity volume and V was the original volume (calculated with the length, width, and thickness of the liftout). The swelling in the 500-700nm depth region was taken as the nominal swelling value.

3. Microstructure characterization of neutron irradiated alloys

Most neutron irradiated microstructure characterization results including swelling and precipitation were published and the results are briefly viewed in this section.

3.1 Neutron microstructure of HT9 (ACO-3)

Summary of the neutron irradiated microstructure of HT9 was based on reference [3.1] and [3.2]. Summary of voids and dislocations is given in Table 3.1. Summary of precipitate size and density is given in Table 3.2.

3.1.1 FFTF Irradiation

Neutron irradiated HT9 were cut from an ACO-3 duct that was included in a partial core loading of FFTF known as the Core Demonstration Experiment (CDE). The CDE ensemble was progressively moved inward in the FFTF core resulting in variations in both neutron flux and temperature. The ACO-3 subassembly was one of the CDE assemblies and was irradiated in three positions of the FFTF fast reactor, accumulating an exposure of 1524.2 equivalent full power days (EFPD) over a six-year period with a peak fast fluence of 38.9×10^{26} n/m^2, E > 0.1 MeV. Estimated dose and temperature profiles at the conclusion of the ACO-3 irradiation are shown in Figure 3.1. The conversion factors used to calculate dose from fast fluence were taken from analyses performed on dosimetry packets from Materials Open Test Assemblies (MOTA) located in comparable positions in the FFTF core. In the central core region (~443°C:155dpa), the conversion factors ranged between 4.1 and 4.5 dpa per 10^{26} n/m^2(E > 0.1 MeV), depending on the core power level, the local flux distribution and the surrounding assemblies. The temperature gradient across the duct was estimated to be less than 5 °C. The variations in temperature are not estimated but are probably within ±10 °C. The displacement dose is considered to be accurate within ±5%. The two irradiation conditions (410°C:100dpa and 443°C:155dpa) are indicated by arrows in Figure 3.1. In addition, irradiation conditions at 380°C:20dpa, 466°C:92dpa and 505°C:4dpa were also examined

3.1.2 Irradiation microstructure of ACO-3 at 410°C:100dpa

Precipitates

Precipitates in ACO-3 irradiated at 410°C:100dpa were characterized by both EFTEM and APT. Two types of precipitates, Cr-rich α'-phase and Ni/Si-rich G-phase, were observed. Average α' diameter and density measured from several EFTEM jump ratio images are 8.8 ± 1.3 nm and 2.2×10^{22} m^{-3} respectively. The average G-phase particle size is 16 ± 3.1 nm and the density is 3.2×10^{21} m^{-3}. α' is absent around the carbide, G-phase precipitates and around the voids. Other than these denuded zones, α' particles appear uniform in the matrix. Figure 3.2 are APT reconstruction images of HT9 at 410°C:100 dpa showing Cr-rich α′ and Ni/Si/Mn-rich G-phase. The average α' particle size and the density based on APT reconstructions are 5 nm and 1×10^{23} m^{-3} respectively. The G-phase density is measured to be 2×10^{22} m^{-3}. Due to the low number density of G-phase precipitates, no complete precipitate was found within analyzed volume. Therefore, average size

was not reported and the number density was estimated by counting each found precipitate as 1/2.

Voids

Voids were characterized using TEM in HAADF mode. Voids as small as ~6nm were imaged in this mode. As shown in Figure 3.3(a), void distribution appears inhomogeneous and clustering. Some grains show substantially more voids than others. The average void size is determined to be 18 nm with a density of 7.5×10^{19} m^{-3} corresponding to 0.02% void swelling.

Dislocations

(F/M) steel HT9 was previously irradiated as a component known as ACO-3 duct in FFTF. TEM revealed small dislocation loops for g=110 and back dot damage as seen in Figure 3.4 after irradiation at 410°C to 100 dpa. A void is also seen in the image. The numbers were limited for a reliable statistics on the loop size and density.

3.1.2 Irradiation microstructure of ACO-3 at 443°C:155dpa

Precipitates

Precipitates in ACO-3 irradiated at 440°C:155dpa were characterized by EFTEM only. Cr-rich α'-phase and Ni/Si-rich G-phase were observed. Average α' size and density measured from several EFTEM jump ratio images are 9.6 ± 1.9 nm and 1.1×10^{21} m^{-3} respectively. Note that α' precipitate distribution does not appear uniform anymore as under lower temperature irradiation conditions. Compared to the 410°C:100dpa irradiation , the average G-phase diameter increases to 26.5 ± 5.7 nm and the density slightly decreases to 1.1×10^{21} m^{-3}.

Voids

Both void size and density increase compared to the 410°C:100dpa irradiation as can be seen in the dark field HAADF image of Figure 3.3b. The average void size and the density are 28 nm and 2.5×10^{20} m^{-3}, respectively, void swelling based on the average void size and number density is calculated to be ~0.3%.

Dislocations

The network dislocations are assumed to contain only a<1 0 0> and (a/2)<1 1 1> components.
The total network dislocation density is estimated to be $\sim3\times10^{15}$ m^{-2} and (a/2)<1 1 1> dislocation density is estimated to be $\sim2.2\times10^{15}$ m^{-2} indicating the network dislocation structure is predominantly (a/2)<1 1 1> type. Dislocation loops are predominantly a<1 0 0> type, but their number density is relatively low. The mean loop size is estimated to be ~18 nm. Loop number density is estimated to be $\sim5\times10^{20}$ m^{-3}.

3.1.2 Irradiation microstructure of ACO-3 at 466°C:92dpa

Precipitates

No irradiation-induced precipitates were observed in this irradiation condition.

Voids

Some isolated voids were observed in HT9 irradiated at 466°C to 92 dpa (Figure 3.5). The voids appear to be in the carbide precipitates. Some very small bubbles were also observed.

Dislocations

Dislocations were examined in HT9 irradiated at 466°C to 92 dpa (Figure 3.6). Limited statistics indicates that the average loop size is ~17.5 nm at this condition.

3.2 Neutron microstructure of T91 (413°C:184 dpa)

The neutron irradiated microstructure data for T91 heat 30176 at 413°C:184 dpa was published in [3.3]. It was irradiated in the Fast Flux Test Reactor Facility (FFTF) as part of the Materials Open Test Assembly (MOTA) program. The investigated T91 sample was irradiated as a small scale Charpy specimen (KLST) with specimen code AF33.

Precipitates

Precipitates in T91 were examined using TEM. Other than $M_{23}C_6$ and MC carbides which are likely pre-existing precipitates, no significant populations of second phase particles were found. A few Ni/Si-rich precipitates, presumably G-phase particles, were observed in one zone but quantities were too low and the particle densities were not reliably obtained. No Cr-rich α′ or Laves phase were observed in any of the investigated zones. After irradiation, the $M_{23}C_6$ carbides were found to contain some unidentified internal features.

Voids

Voids inT91 were found to have an average size of 29 nm and an average density of 8.3×10^{20} m^{-3} based on a measurement of 933 voids over 5 different zones. This would correspond to 1.6 % void swelling. Figure 3.7 is a dark field (HAADF) image of T91 at 413°C:184dpa showing voids (dark contrast) within laths.

Dislocations

The dislocation microstructure was analyzed by transmission electron microscopy (TEM). TEM revealed microstructure containing dislocation loops (g=110) and black dot damage (Figure 3.8). Black dots may also contain damage due to FIB sample preparation. Quantities of loops were low to state reliable loop size or densities

Table 3.1. Summary of voids and dislocations in neutron irradiated HT9 and T91

	T (°C)	Dose (dpa)	Voids			Dislocation loop	
			Size (nm)	Density (m^{-3})	Swelling (%)	Size (nm)	Density (m^{-3})
HT9 84125	380	20	N.O.	N.O.	0	(~14)	(~9.3×10^{20})
	410	100	18	7.5×10^{19}	0.02	NA	NA
	443	155	28	2.5×10^{20}	0.3	18	~5×10^{20}
	466	92	~30*	NA	0*	NA	NA
	505	4	N.O.	N.O.	0	N.O.	N.O.
T91 30176	413	184	29	8.3×10^{20}	1.6	NA	NA

Table 3.2. Summary of precipitates in neutron irradiated HT9 and T91

	T (°C)	Dose (dpa)	α′-phase				G-phase			
			TEM		APT		TEM		APT	
			Size (nm)	Density (m^{-3})	Size (nm)	Density (m^{-3})	Size (nm)	Density (m^{-3})	Size (nm)	Density (m^{-3})
HT9 84425	380	20	7.8 ± 1.2	7.2×10^{22}	4	1.2×10^{24}	11.3 ± 2.3	9.3×10^{21}	8.5± 1.5	3.2×10^{21}
	410	100	8.8 ± 1.3	2.2×10^{22}	5	1×10^{23}	16 ± 3.1	3.2×10^{21}	-	2×10^{22}
	440	150	9.6 ± 1.9	1.1×10^{21}	NA	NA	26.5 ± 5.7	1.1×10^{21}	NA	NA
	466	92	N.O.	N.O.	N.O.	N.O.	N.O.	N.O.	N.O.	N.O.
	505	4	N.O.	N.O.	NA	NA	N.O.	N.O.	NA	NA
T91 30176	413	184	N.O.	N.O.	NA	NA		Very low	NA	NA

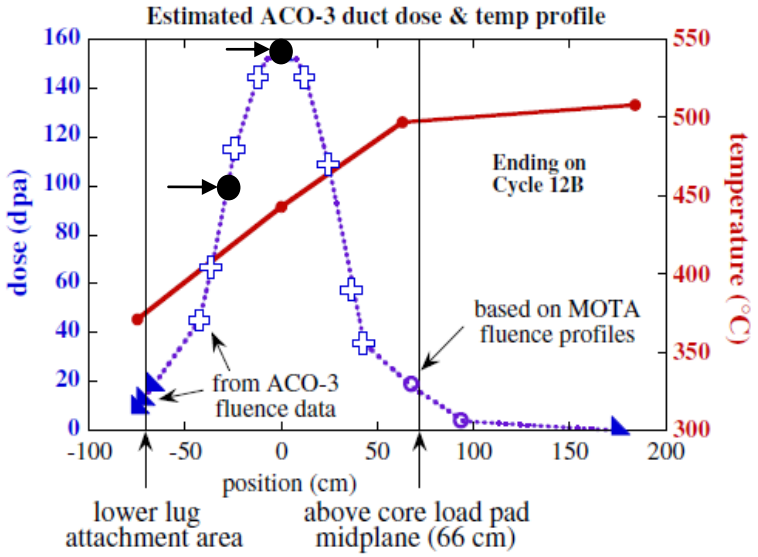

Figure 3.1. Estimated dose and temperature profiles of the ACO-3 duct.

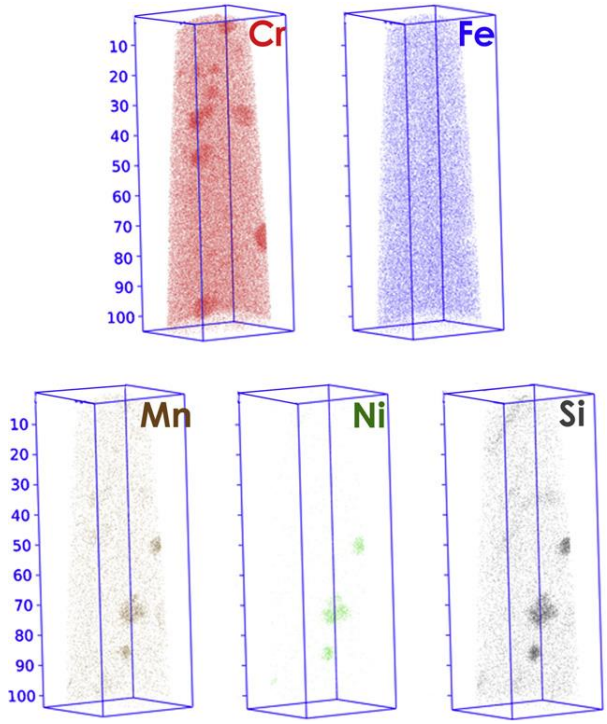

Figure 3.2. APT reconstruction images of HT9 at 410°C:100 dpa showing Cr-rich α′ and Ni/Si/Mn-rich G-phase.

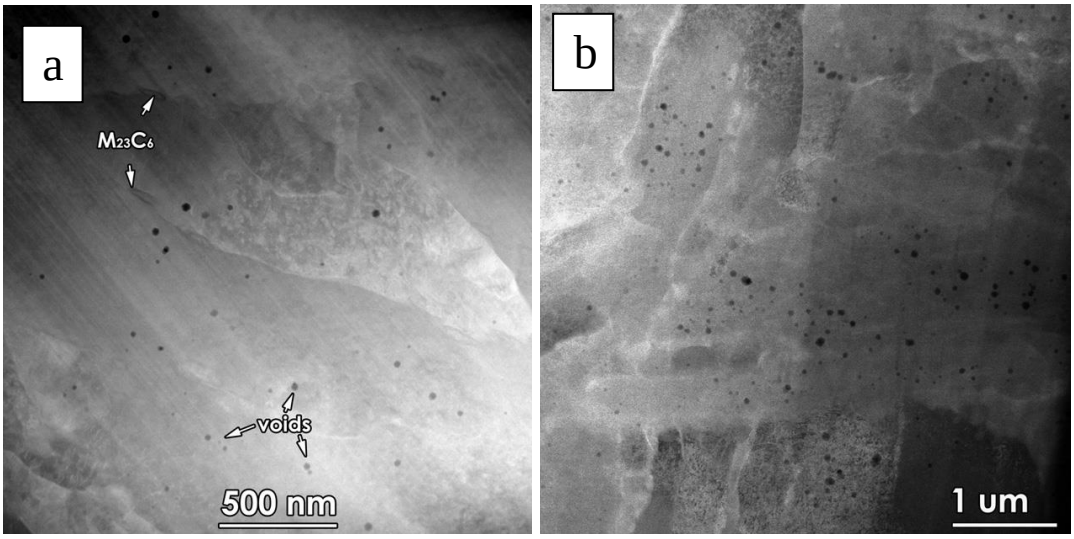

Figure 3.3. Dark field (HAADF) images of HT9 at low magnification showing voids (dark contrast) within some grains : (a) 410°C:100dpa, (b)440°C:155dpa.

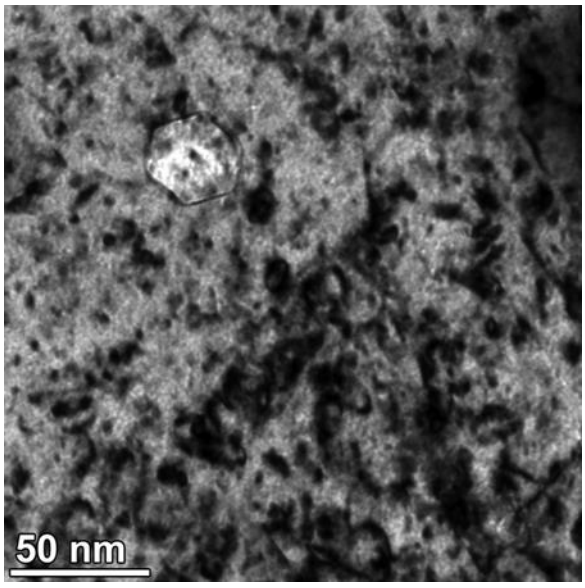

Figure 3.4. Dislocation microstructure of HT9 for g=110 irradiated at 410°C to 100 dpa.

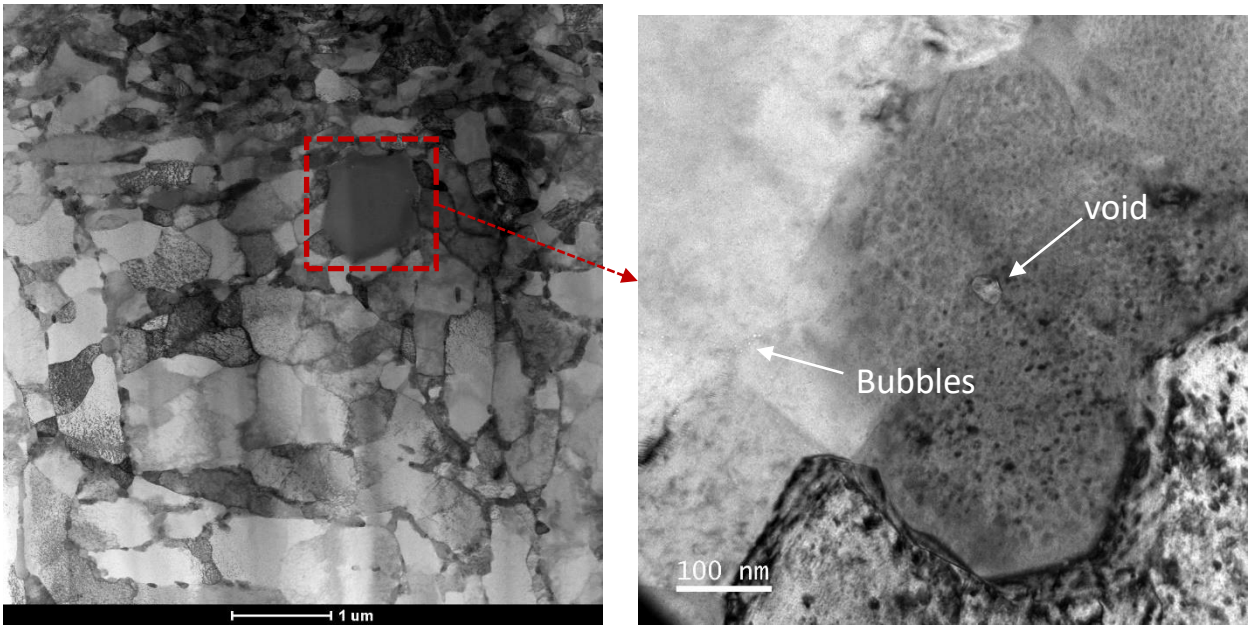

Figure 3.5. Some isolated voids were observed in HT9 irradiated at 466°C to 92 dpa. The indicated large void appears to be in the big carbide. There also some very small bubbles that appear to be along the grain boundary.

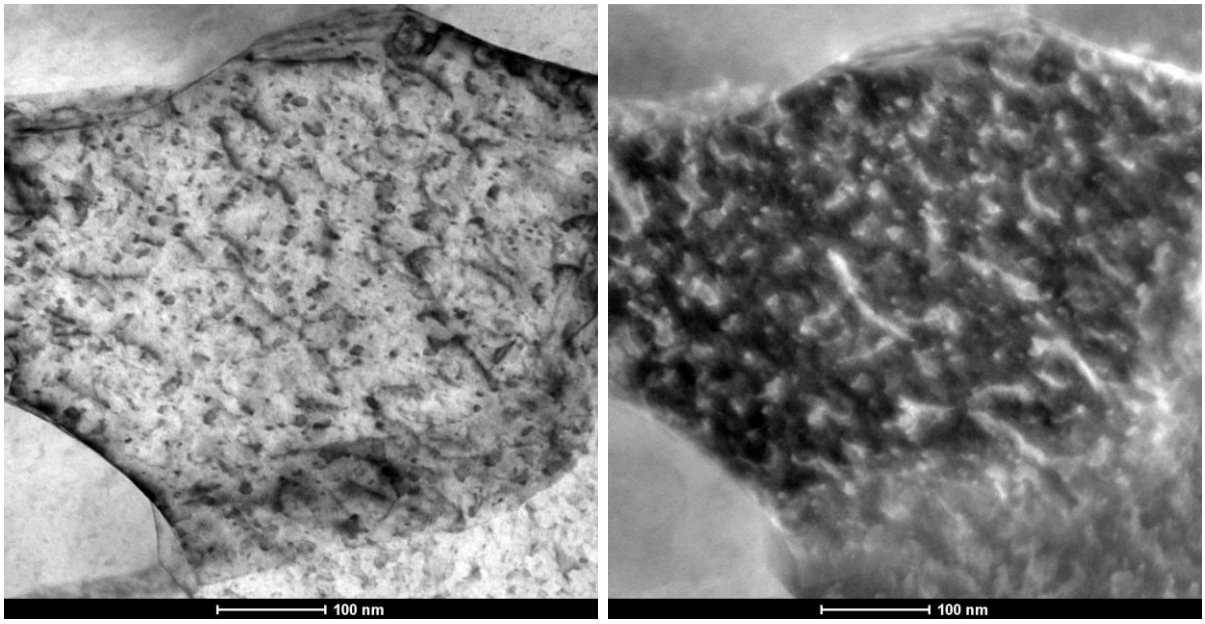

Figure 3.6. Dislocations in in HT9 irradiated at 466°C to 92 dpa. Limited statistics from the above image indicates that the average loop size is ~17.5 nm at this condition.

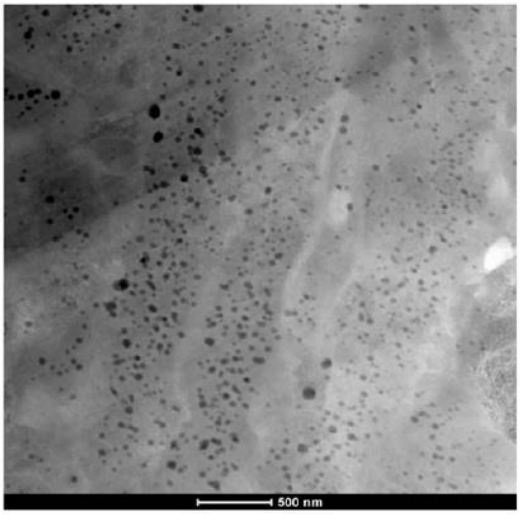

Figure 3.7. Dark field (HAADF) image of T91 at 413°C:184dpa showing voids (dark contrast) within laths.

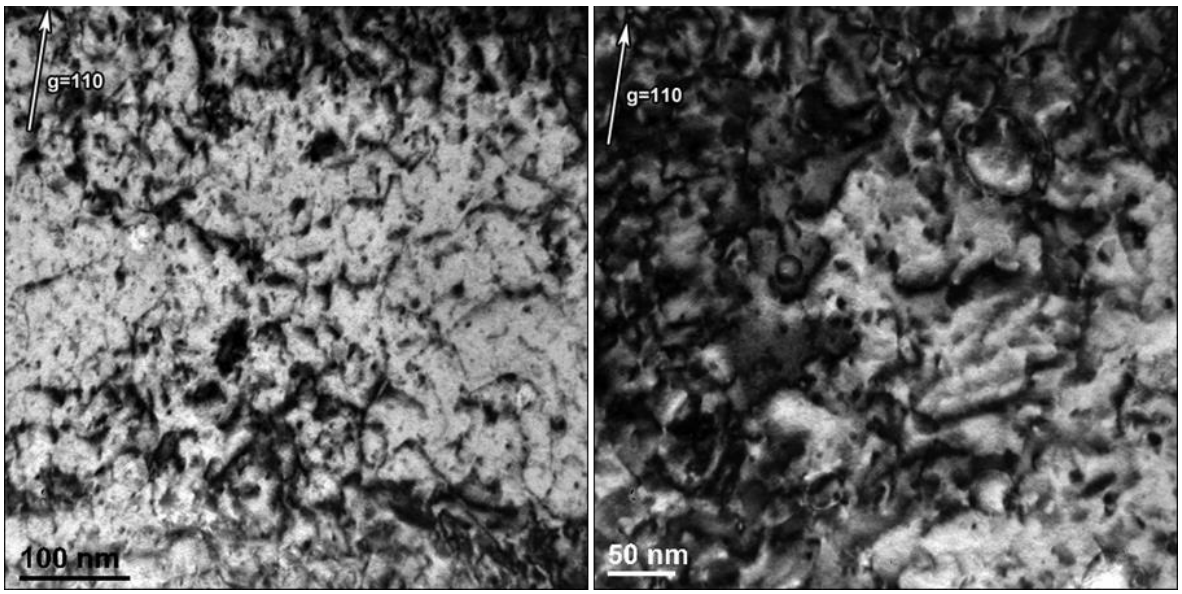

Figure 3.8. Dislocation microstructure of T91 for g=110 irradiated at 413°C to 184 dpa.

References:

3.1 O. Anderoglu, J. Van den Bosch, P. Hosemann, E. Stergar, B.H. Sencer, D. Bhattacharyya,R. Dickerson, P. Dickerson, M. Hartl, S.A. Maloy, Phase stability of an HT-9 duct irradiated in FFTF, Journal of Nuclear Materials 430 (2012) 194–204
3.2 B.H. Sencer, J.R. Kennedy, J.I. Cole, S.A. Maloy, F.A. Garner, Microstructural analysis of an HT9 fuel assembly duct irradiated in FFTF to 155 dpa at 443 °C, Journal of Nuclear Materials 393 (2009) 235–241
3.3 J. Van den Bosch, O. Anderoglu, R. Dickerson, M. Hartl, P. Dickerson, P. Hosemann, S.A. Maloy, SANS and TEM of ferritic-martensitic steel T91 irradiated in FFTF up to 184 dpa at 413°C, Journal of Nuclear Materials, 440(2013) 91-97

4. Ion irradiations and characterization

Throughout the project, 16 ion irradiation experiments were performed. The swelling results of these experiments are summarized in Table 4.1 (HT9 84425), Table 4.2(T91 30176) and Table 4.3 (T91 C2269). These irradiations were performed to achieve the project objectives and to explore the viability of using ion irradiations as a surrogate to neutron irradiations. The effects of dose, temperature, helium, and carbon uptake were explored and are discussed along with the relevant results in the discussion section.

Irradiations of HT9 84425 were conducted at 400°C to 250 dpa, 420°C up to 200 dpa, 440°C to 150 dpa and 460°C up to 450 dpa. Irradiations of T91 30176 were conducted at 420°C to 200 dpa and 460°C up to 450 dpa. Irradiations of T91 C2229 were conducted at 460°C up to 450 dpa. The purpose of the irradiations on T91 C2229 was to study the effect of helium on swelling and helium was pre-implanted to 1, 10, 100 and 1000 appm prior to irradiation. Note that there were three series of irradiation conducted for alloy T91 C2229 (Table 4.3). In series 1, irradiation was first conducted to 150 dpa and swelling was characterization. Samples were then irradiated to an additional 150 dpa to reach 300 dpa. Voids in most samples disappeared after 300 dpa, resulting in zero swelling. However, significant precipitation of carbide was observed. It was later on confirmed that there was carbon uptake during Fe^{++} irradiations, which suppressed void swelling. Series 2 irradiation was to repeat series 1 irradiation but there was still carbon uptake even though the amount could be less than that in series 1. Series 3 irradiations avoided carbon uptake by coating the sample surface with ~100nm alumina.

Table 4.1. Summary of the irradiations conducted and the resulted swelling behavior in HT9 84425.

Irradiation Condition				Voids (500-700nm)				
Date of Completion	**T (^{o}C)**	**Dose (KP)**	**He (appm)**	**Number of TEM Samples Prepared**	**Number of Voids**	**Void Diameter (nm)**	**Void Density ($10^{20}m^{-3}$)**	**Swelling (%)**
1/15/2013	400	250	0	1	0	0.0	0.000	0
4/14/2013	440	150	1	1	0	0.0	0	0
			10	2	8	10.9	0.274	0.00149
6/25/2013	460	188	1	2	65	26.4	3.028	0.485
			10	2	343	29.8	12.000	2.9
11/13/2013	460	188	1	1	46	17	2.04	0.076
			10	1	274	16.58	13.33	0.3035
		375	1	2	211	35.4	5.88	2.69
			10	2	286	39.95	14.11	8.36
		188	0	2	69	12.78	2.7	0.041
			10	2	282	10.92	11.8	0.13
10/29/2014	460	75	0	2	0	0	0	0
			1	2	0	0	0	0
			10	2	0	0	0	0
			100	2	5	10.64	0.417	0.0014
		450	1	3	200	51.4	2.75	2.87
			10	3	263	52.2	5.67	6.28
2/18/2015	420	40	1	2	0	0	0	0
			10	2	0	0	0	0
5/28/2015	420	80 (+40)	1	2	0	0	0	0
			10	2	0	0	0	0
8/26/2015	420	200(+120)	1	0				
			10	2				

Table 4.2. Summary of the irradiations conducted and the resulted swelling behavior in T91 30176.

Irradiation Condition				Voids				
Date of Completion	**T(^{o}C)**	**Dose (KP)**	**He (appm)**	**Number of TEM Samples Prepared**	**Number of Voids**	**Void Diameter (nm)**	**Void Density ($10^{20}m^{-3}$)**	**Swelling (%)**
6/25/2013	460	188	1	1	71	21.7	4.77	0.374
			10	2	512	27.8	16.19	3.15
11/13/2013	460	375	1	2	536	36.69	4.13	1.71
			10	2	1036	42.2	16.01	9.54
10/29/2014	460	75	1	2	0	0	0	0
			10	2	25	20.9	1	0.075
		450	1	2	114	44.95	3.11	2.15
			10	2	523	45.4	9.55	6.82
2/18/2015	420	40	1	2	0	0	0	0
			10	2	0	0	0	0
5/28/2015	420	80 (+40)	1	2	0	0	0	0
			10	2	0	0	0	0
6/26/2015	420	200 (+120)	1	0				
			10	2				

Table 4.3. Summary of the irradiations conducted and the resulted swelling behavior in T91 C2229.

Irradiation Condition				Voids				
Date of Completion	**Temperature (^{o}C)**	**Damage (K-P dpa)**	**He (appm)**	**Number of TEM Samples Prepared**	**Number of Voids**	**Void Diameter (nm)**	**Void Density ($10^{20}m^{-3}$)**	**Swelling (%)**
11/25/2015 (series 1)	460	150	0	2	21	30.1	0.76	0.14
			1	2	63	39.1	3.7	1.54
			10	2	298	33.2	11.6	2.83
			100	2	234	27.2	9.7	1.37
			1000	2	328	11.6	16.5	0.28
1/22/2016 (series 1)	460	300 (150+150)	0	1	-	-	-	-
			1	-	-	-	-	-
			10	2	242	26.5	5.87	0.78
			100	2	-	-	-	-
			1000	2	-	-	-	-
3/18/2016 (series 2)	460	150	0	2	74	15.7	2.2	0.056
			1	2	165	16.5	8.64	0.248
			10	2	290	14.17	17.95	0.34
			100	2	213	10.27	11.74	0.094
			1000	2	37	5.97	3.18	0.006
4/28/2016 (series 2)	460	300 (150+150)	0	2	121	26.6	3.416	0.433
			1	2	244	25.6	6.58	0.72
			10	2	208	22.4	13.24	1.02
			100	2	384	17.3	10.72	0.41
			1000	2	198	8.54	6.77	0.034
6/16/2016 (series 2)	460	450 (300+150)	0	2	83	27.8	2.63	0.422
			1	2	180	30.49	9.35	1.88
			10	2	294	28	10.34	1.65
			100	2	219	23.4	8.37	0.8
			1000	2	10	16.8	0.462	0.013
9/29/2016 (series 3)	460	300	0	2	540	29.3	20.1	3.909
			1	2	598	28.2	21.6	3.85
			10	2	535	26.4	18.9	2.75
			100	2	352	17.79	11.96	0.603
			1000	2	236	9.03	10	0.096
		300	10	2	65	21.6	2.45	0.17
11/2/2016	460	50	0	2	392	10.14	11.73	0.09

(series 3)			1	2	387	8.72	20.15	0.107
			10	2	453	8.49	24.2	0.12
			100	2	303	7	17.88	0.046
			1000	2	424	4.6	22	0.017
12/2/2016 (series 3)	460	150 (50+100)	0	1	765	19.2	17.6	0.92
			1	1	672	15.31	20.7	0.58
			10	1	868	14.3	24	0.56
			100	1	1037	9.54	24.7	0.188
			1000	1	1067	7.11	27.6	0.076

4.1 Ion irradiation at 400°C to 250 dpa, no helium pre-implantation

Cross-view of the TEM foils for HT9 and T91 that capture the whole irradiated depth were prepared using the FEI Helios FIB at EMAL (now Michigan Center for Materials Characterization, or $(MC)^2$). Analysis of the ion-irradiated microstructure of was conducted using the JOEL 2010F TEM with accelerating voltage of 200KV. Figure 4.1(a) and (b) show TEM micrographs of the HT9 and T91 microstructure respectively. Figure 4.1(a) is a high angle annular dark field (HAADF) image under which voids would appear as distinct dark regions (spots). Figure 4.1(b) is a bright field image of the irradiated T91microstructure. No voids were observed in either HT9 or T91.

NF616 and 14YWT used in this work were in the form of bar-shape specimens with the center ~10mm of one side ion-irradiated to 250 dpa at 400°C. TEM thin foil specimens were prepared from the irradiated surface by standard lift-out method and Ga ion milling using the Helios NanoLab DualBeam (FIB/SEM) Microscope. Prior to the lift-out procedure a 2 μm thick Pt protection layer was deposited on the irradiated surface to protect the microstructure underneath from ion milling damage. The TEM specimens were thinned down to less than 100 nm then low energy Ga beam at 1kV was used for surface cleaning and Ga damage removal. TEM observation was conducted on the JEOL 2010F microscope operated at 200kV.

Figure **4.2**(a) is the bright field image of NF616 showing that in this particular region of the specimen the irradiated depth reached ~1.3 μm, which is consistent with SRIM calculation.
Figure **4.2**(b) was taken from the irradiation damage boundary showing that there is significant difference in number density of defects between the irradiated region and the unirradiated region. Voids were not observed in NF616 at this irradiation conditions.

A bright field TEM image shown in Figure 4.3 indicates the extent of the ion irradiation damage. The position of the original irradiated surface is marked by the Pt layer deposited during FIB milling. High magnification BF images taken long the edge of the TEM specimen are shown in Figure 4.4 at different irradiation depths. In these images, black contrast of few nanometers in size and taken to be small clusters are observed.

The microstructure of high dose NF616 and 14YWT were characterized in more detail using APT. The primary goal is to compare the microstructures before and after iron implantation. Needle-shaped APT specimens were prepared from the irradiated surface by the standard lift-out method and annular Ga ion milling using the Helios NanoLab DualBeam (FIB/SEM) Microscope. The APT specimens can be prepared at any depth between 0-3μm from the surface by controlling the ion milling. A 5kV Ga milling was utilized to reduce the radius of tips to ~50nm and remove Ga damage. APT specimens were analyzed using a LEAP-4000XHR microscope operated in electrical mode with a voltage pulse fraction of 20%. Specimen temperature was maintained at 40K and detection rate was kept constant at 0.005 atom/pulse. Laser pulsing was not used for better spatial resolution and avoiding possible surface diffusion of trace elements. Reconstruction of the relative atom positions from the raw data was performed using the commercial software, IVAS 3.6.4 from CAMECA^{TM}. The data was reconstructed using the default evaporation field of 33 V/nm for Fe at cryogenic temperatures and an image compression factor of 1.1 which is determined assuming spherical shape clusters and flat grain boundaries. Data collection was stopped when the applied voltage on the specimens reached 6.5kV. The specimens were re-sharpened using low kV Ga milling for continue APT analyses, which allows to collect multiple datasets with gradually increase in depth from the same APT specimen.

As mentioned earlier, the irradiation depth is about 1.3 μm for 5 MeV Fe^{++} based on SRIM calculation. An APT reconstruction obtained from the unirradiated region in 14YWT which is 2.0 μm under the irradiated surface is shown in Figure 4.5(a). In the unirradiated region, oxide clusters are observed with sizes as large as 5-8nm in diameter. The same clusters are observed from a region about 1.8 μm under the surface by TEM bright field imaging as shown in Figure Figure 4.5(b). A uniform distribution of smaller oxide clusters of size about 2nm is found within the matrix, as well as at grain boundaries. In addition, clear C segregation at grain boundaries is also observed.

An APT reconstruction obtained at a depth of 1.1 μm (around the damage peak) under the irradiated surface is shown in Figure 4.6. The distribution of C, Si, TiO, YO and CrO are displayed in separate maps. Clear segregations of C, Si and Y at grain boundaries are observed. The absence of large oxide clusters in this region is confirmed in agreement with TEM observations. The smaller oxide clusters are still present but have become more diffuse and are only clearly seen at dislocations. Figure 4.7 shows the distribution of C, Si and oxides in a region at 450nm from the irrdiated surface. Y and Cr oxides cluster are still present in the matrix and at grain boundaries. The presence of C clusters seen in this region is stronger than that in Figure 4.6.

APT specimens of irradiated NF616 were also prepared at various depths from the irradiated surface. The Cr map in Figure 4.8 is obtained from the unirradiated region beyond 1.3 μm showing a uniform distribution of Cr. The APT reconstruction obtained from a region 280 nm deep from the irradiated surface reveals the formation of Cr-C-Si rich spherical and plate-like clusters, as shown in Figure 4.9. It is also observed that Mn appear to partition to the Cr-rich clusters. Figure 4.10(a) shows the presence of large CrC at a grain boundary obtained from the implanted region at about 240nm from the surface. The type of CrC is determined to be $M_{23}C_6$ based on the ratio of transition metal to carbon, which is 3.6 and close to the value of 3.8 in

$M_{23}C_6$ type carbide. Sillicon segregation at grain boundaries and surface of Cr carbides is confirmed. The presence of carbide at grain boundaries is in agreement with the TEM observation shown in Figure 4.10(b).

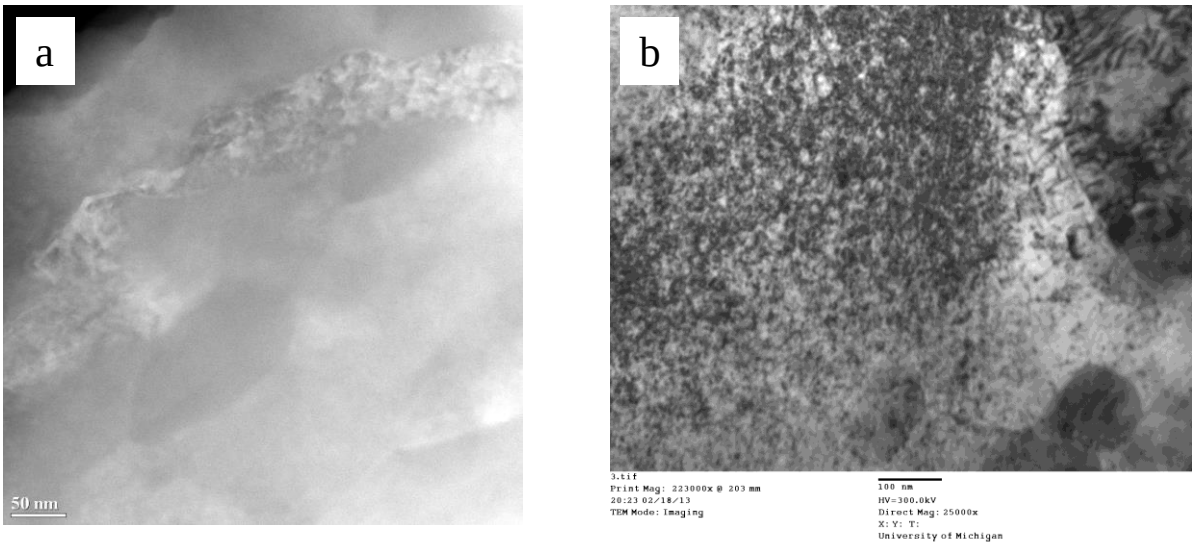

Figure 4.1. (a) STEM-Dark field (HAADF) image of HT9 at 400°C:250 dpa showing of the absence of voids. (b) Bright field TEM image of T91at 400ºC: 250 dpa showing a dense dislocation microstructure and no appearance of voids.

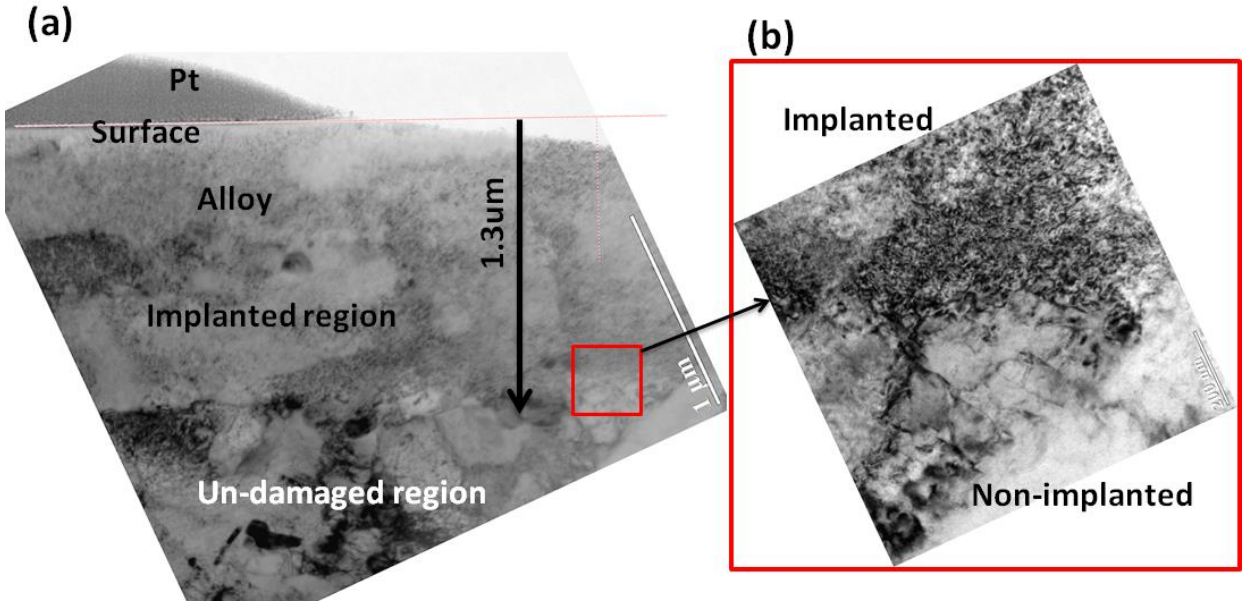

Figure 4.2. (a) bright field TEM image of NF616 irradiated to 250 dpa at 400°C (b) high magnification bright field image of the boundary between the irradiated region and the unirradiated region, indicating a damage depth of ~1.3 μm.

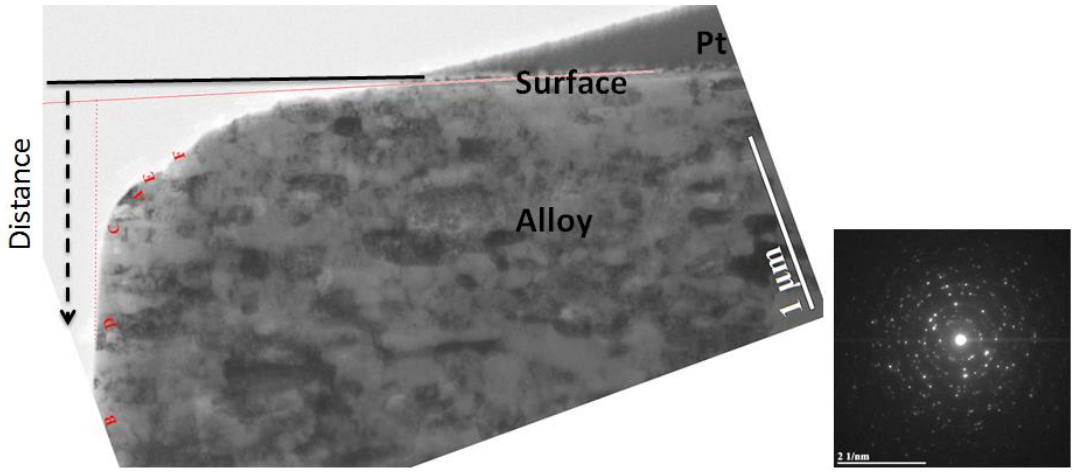

Figure 4.3. TEM bright filed image of 14YWT Fe^{++}-irradiated to 250 dpa at 400°C. The insert is the electron diffraction pattern showing the characteristic of nanocrystalline structure.

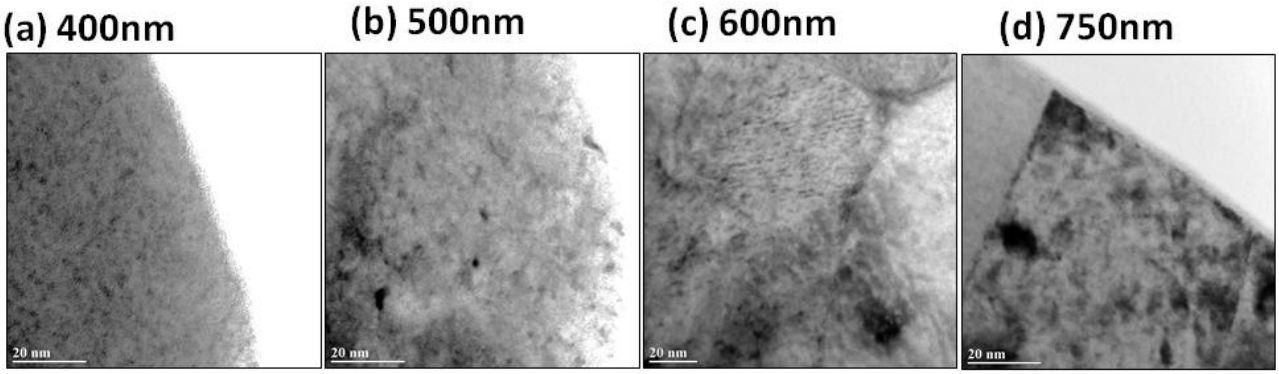

Figure 4.4. High magnification TEM bright filed images of 14YWT Fe^{++}-irradiated to 250 dpa at 400°C at different irradiation depth: (a) 400 nm, (b) 500 nm, (c) 600 nm, (d) 750 nm from the irradiated surface.

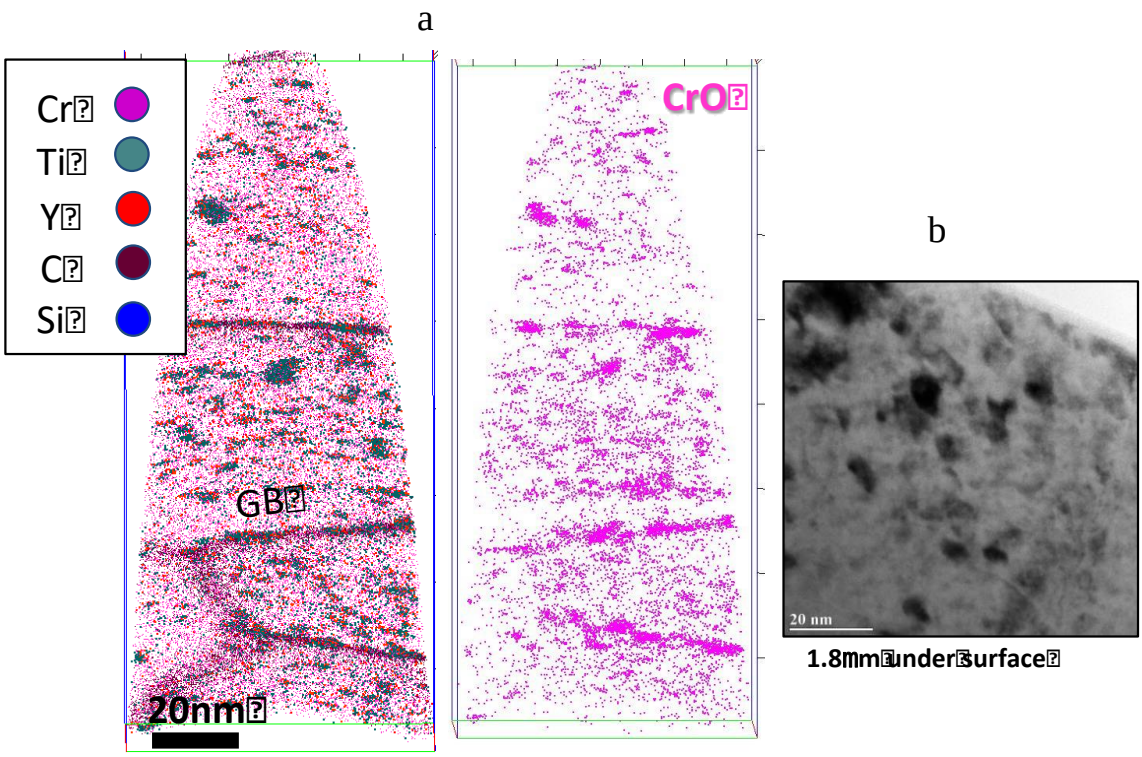

Figure 4.5. (a) APT reconstruction from the unirradiated region of 14YWT at a depth of 2 μm from the irradiated surface showing the distribution of oxide clusters and solute segregation at grain boundaries. (b) Bright field TEM image obtained from a depth similar as the APT reconstruction in (a) showing the presence of large clusters in black contrast.

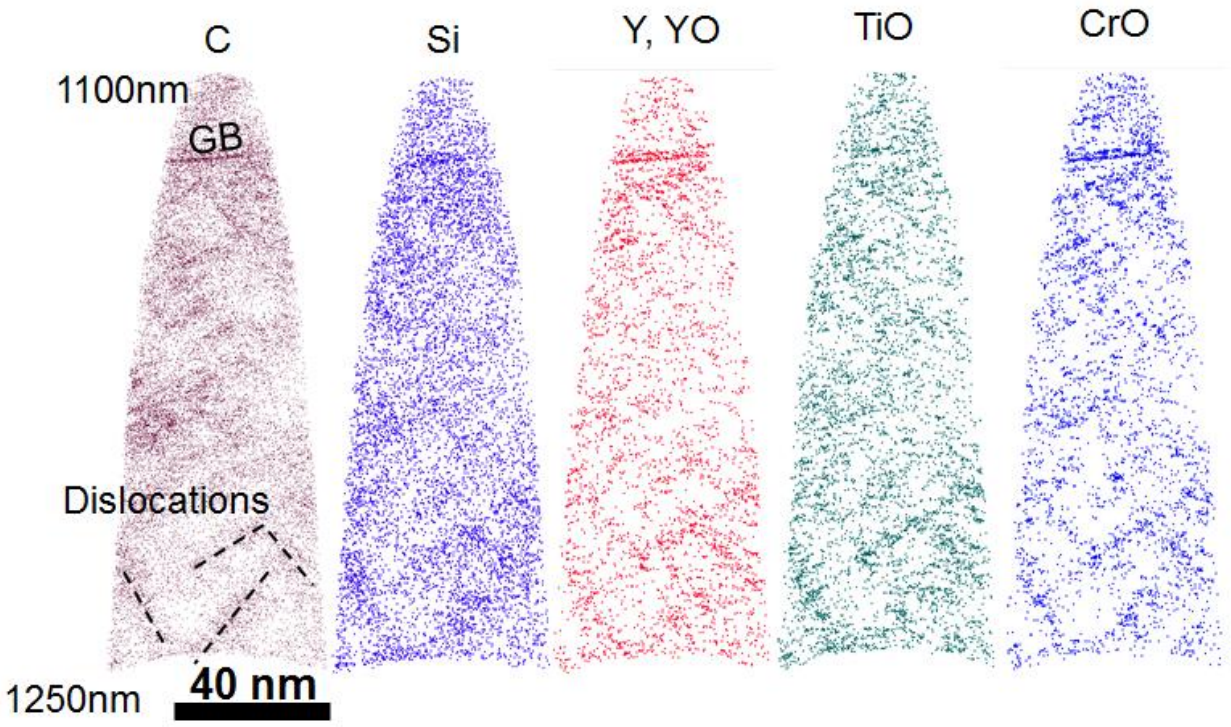

Figure 4.6. 10 nm slices of atom maps from 14YWT irradiated to 250 dpa at 400°C obtained from a region about 1.1 μm from the irradiated surface (near the damage peak).

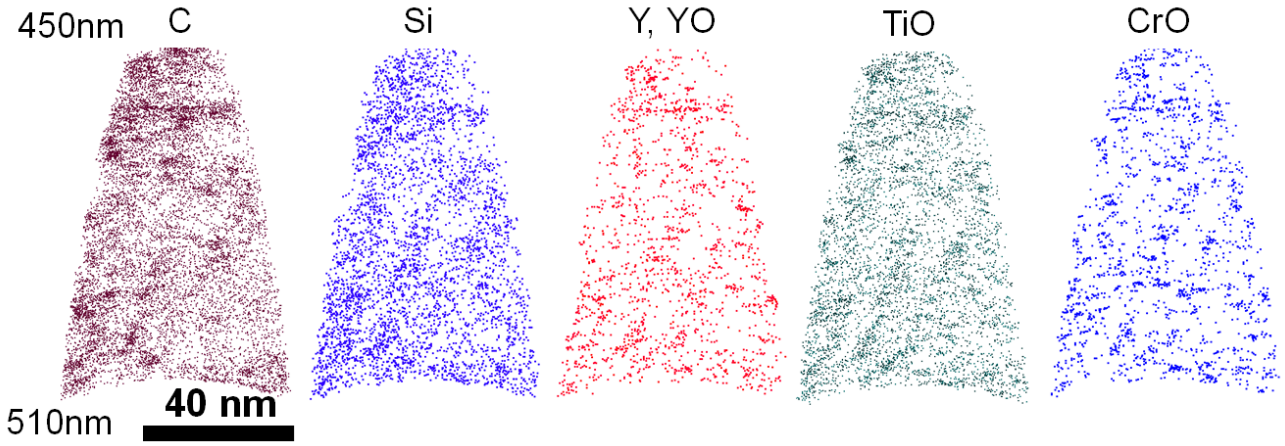

Figure 4.7. 10 nm slices of atom maps from 14YWT irradiated to 250 dpa at 400°C obtained from a region at 450 nm from the irradiated surface.

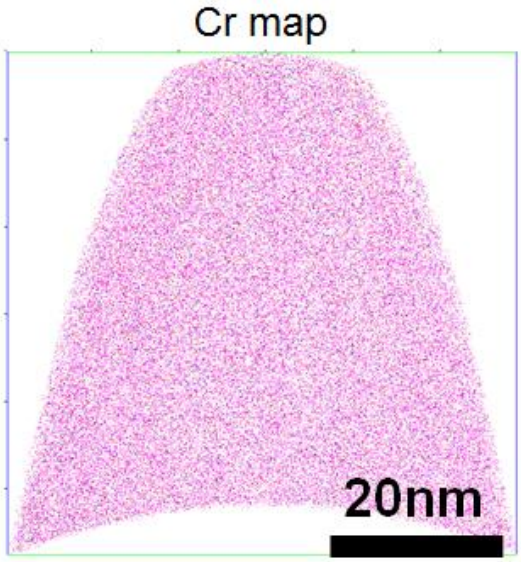

Figure 4.8. Cr map obtained from a region over 1.3μm from the implantation surface in NF616 showing a uniformed distribution of Cr.

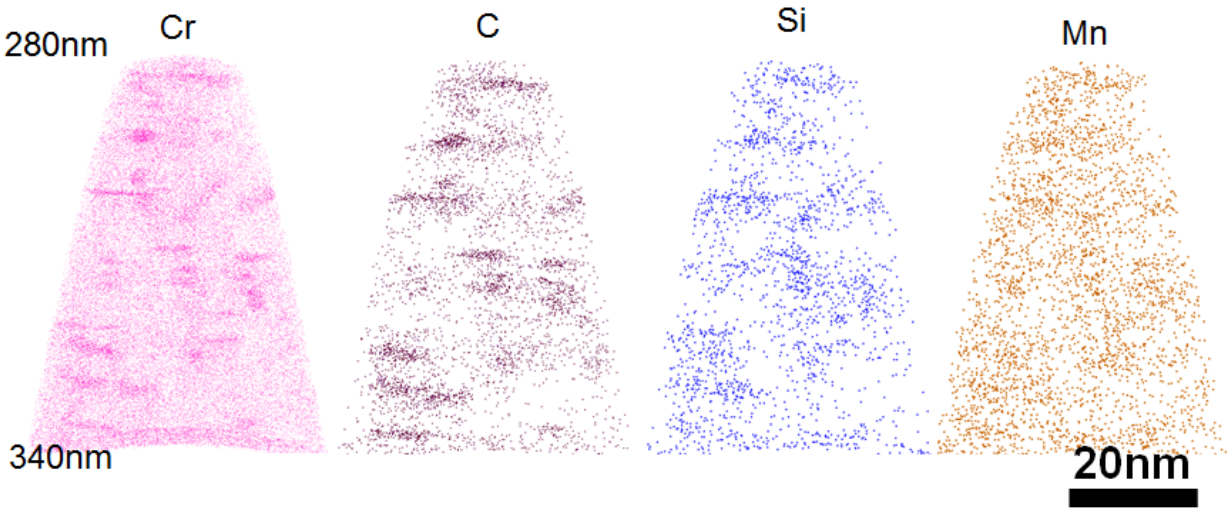

Figure 4.9. Distribution of Cr, C, Si and Mn in NF616 irradiated to 250 dpa at 400°C in a region about 280nm from the irradiated surface showing the formation of Cr clusters.

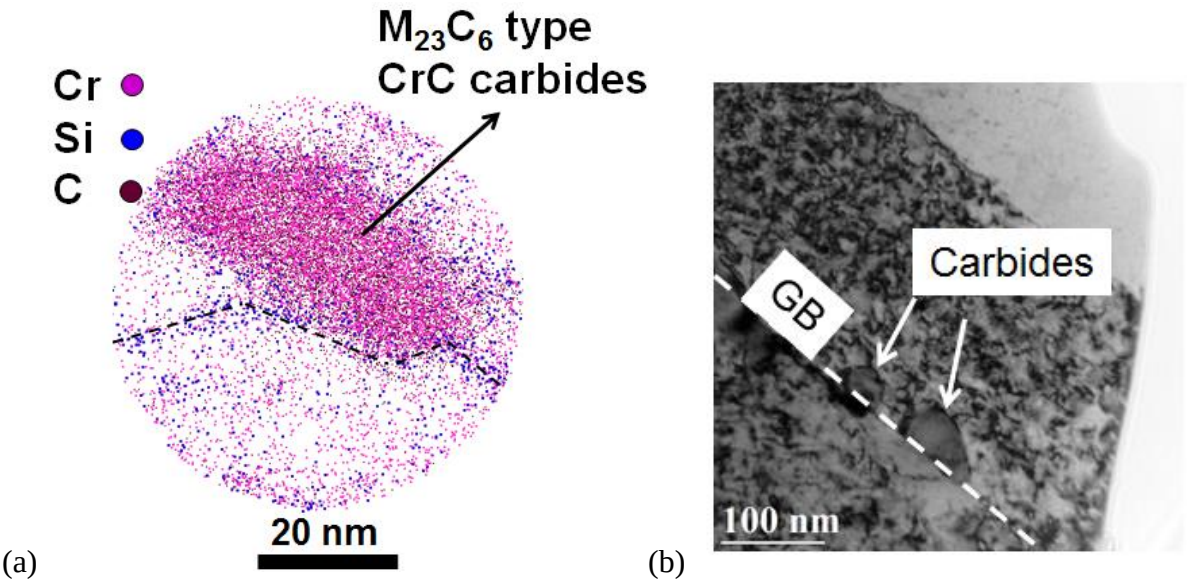

Figure 4.10. (a) Atom map of Cr, Si and C obtained from NF616 irradiated to 250 dpa at 400°C at an irradiation depth of 250 nm from the irradiated surface shows a large $M_{23}C_6$ type CrC at grain boundary. (b) bright field TEM image shows carbides at grain boundaries in a region at 500 nm from the surface.

4.2 Ion irradiation at 420°C up to 200 dpa with helium pre-implantation to 1 and 10 appm

With an estimated temperature shift of about 20°C, a set of irradiations was also performed at 420°C in an attempt to replicate the neutron data at 400 and 410°C. HT9, T91 and 14YWT samples implanted with helium levels of 1 and 10 appm were irradiated in successive experiments at 420°C. The first step at 40 dpa revealed no observable swelling in any of the samples. The second experiment brought the damage level to 80 dpa. Still no swelling was observed in the 500-700nm, however some cavities were observed in the deeper damage regions (see Figure 4.11), suggesting that higher damage levels were still necessary. An additional 120 dpa was added to the 80 dpa samples, bringing the total damage level to 200 dpa. However, an unexpected result occurred in that no swelling was observed. In fact, an extremely high amount of carbide precipitates was observed, as seen in Figure 4.12. This extreme amount of ion-beam induced carburization likely caused the loss of any potential swelling. Ion-induced carburization has been observed before in ion irradiation [4.1,4.2]. It is possible that the uptake due to the ion beam is caused by an interaction with residual carbonaceous gasses in the vacuum system or with organic hydrocarbons on the surface of the samples. Through separate experiments at the Michigan Ion Beam Laboratory, it was demonstrated that a 100 nm thick layer of alumina deposited on the surface of the samples would prevent the uptake of carbon into the bulk of the sample.

The compositions of small clusters was characterized using APT in 14YWT that was Fe^{++}-irradiated at 420°C to 40 and 80 displacement per atom (dpa) after pre-implanted helium level of 1 He appm and 10 He appm. Analyses of the non-implanted materials were also performed for reference. APT and TEM specimens were prepared using the lift-out technique using a FEI Helios 650 Nanolab SEM/FIB dual beam. For the irradiated conditions, the specimens were prepared at 600 nm below the surface. The atom probe tomography analysis was done using a CAMECA LEAP 4000 HR. Specimens were evaporated in either voltage mode at 50K with a 20% pulse fraction or laser mode at 30K with a laser power of 20pJ. Three dimensional data reconstruction was done using the IVAS 3.6.6. software, with the evaporation field fixed at 33V/nm and the image compression factor (ICF) ranging from 1.5 to 1.65.

The maximum separation method [4.3] was used to identify solute clusters, this method involves the selection of 5 different parameters: d_{max}, O, N_{min}, L, and e. If O core atoms are within the distance d_{max} of each other then they are part of the same cluster. Any cluster containing fewer core atoms than N_{min} is discarded. Any other atom that is within the distance L of a core atom is also considered to be part of the cluster. Any cluster atom within the erosion distance, e, from a matrix atom is then removed from the cluster. The clusters were defined by the following ions: Y^{+}, Y^{2+}, Y^{3+}, YO^{+}, YO^{2+}, CrO^{2+}, CrO^{+}, TiO^{+}, O^{+}, and O^{2+}. The nearest neighbor distribution was used to inform on the selection of O and d_{max}. Then the cluster size distribution was used to determine the value of N_{min}. The cluster count distribution was used to check that the combination of parameters (order, d_{max}, N_{min}) is reasonable. In addition, d_{max} was varied between 0.6 nm to 1.2 nm to check on the sensitivity of the result is to the choice of parameters.

To determine the composition of the clusters, the envelope method was used with the parameter L equal to d_{max} and e equal to 0. It was previously observed that significant trajectory aberrations can affect the composition of the clusters [4.4]. Therefore a matrix correction was applied as described in [4.5]. Any Fe present in the cluster and all other solute atoms in proportion to the matrix composition are removed from the cluster atom count. Clusters might have irregular shape so the number of solute core ions was used as a size estimate.

The undamaged region specimens were prepared below 2000 nm from the irradiated surface. Figure 4.5 shows a representative atom probe data set and a bright field TEM image of the undamaged region. Nanoclusters enriched in Cr, Ti, Y and O are clearly observed throughout the matrix, along grain boundaries. In addition, C and N segregate to grain boundaries.

Two pre-implantation conditions were investigated in 14YWT irradiated to 40 dpa at 420°C : 1 appm He and 10 appm He. For the 1 appm He condition, three data sets were collected. For the 10 He appm condition, two data sets were collected under laser mode. No distinction between the two He conditions is made in the subsequent APT data analyses. In general, the distribution of the clusters is inhomogeneous with regions of very high densities and regions almost free of clusters or with large carbide particles along grain boundaries (e.g. left reconstruction in Figure 4.13). Nanoclusters are present along grain boundaries similarly to the non-irradiated region. N, C, and P are also found segregate at grain boundaries. The compositions of the large oxide

precipitates (Figure 4.14), determined using proxigram is consistent with M_2O_3 where M=$Cr_{0.92}$, $Fe_{0.08}$

Similarly to the 40dpa samples, the two pre-implantation conditions are analyzed together. The dataset obtained after 1appm He are shown in Figure 4.15 . As previously, Y, Yo, TiO and CrO are used to highlight the clusters, which are distributed along grain boundaries and within grains. Because of the non-uniformity of the spatial distribution, no conclusion could be drawn as to the effect of irradiation on the structure of the nanoclusters.

The composition of the clusters was measured as given in Table 4.4, although the results need to be interpreted carefully as grain boundary and matrix clusters were combined. The results suggest that the O content in the cluster decreases as a result of irradiation.

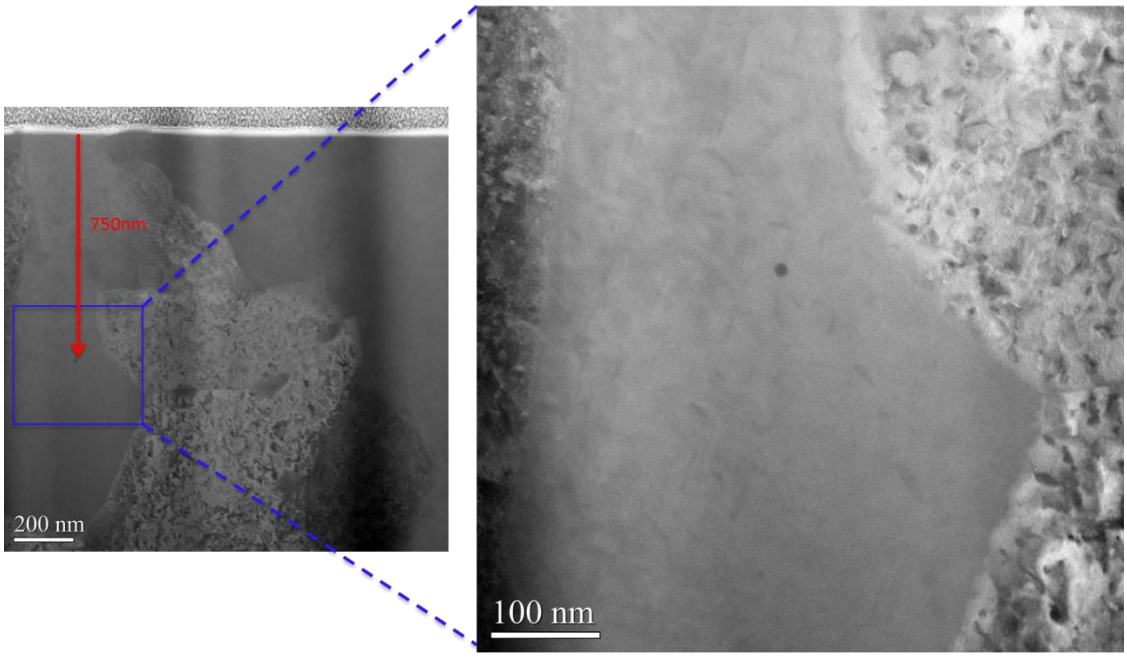

Figure 4.11. HAADF STEM image shows cavities were observed just beyond the analysis region HT9 irradiated at 420 ºC:80 dpa:10He.

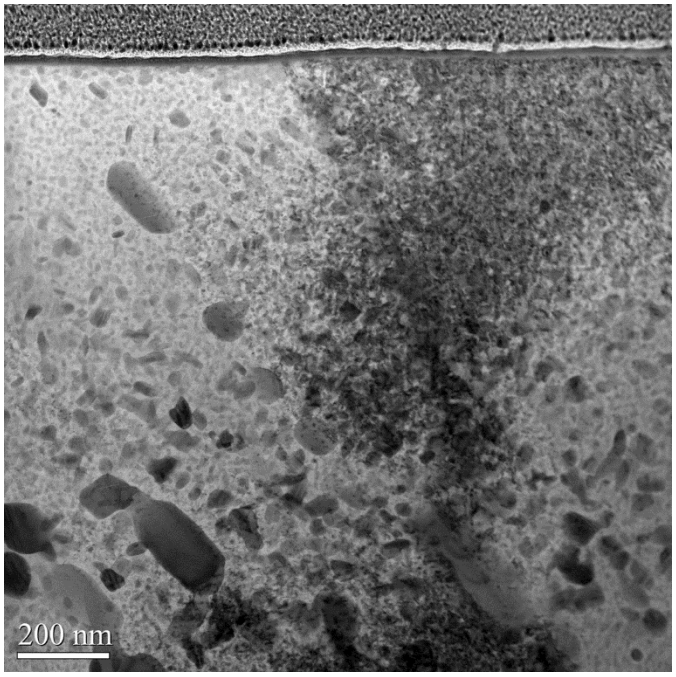

Figure 4.12. BF STEM image of HT9:420C:200dpa:10He is shown above. An extremely high density of precipitation was observed.

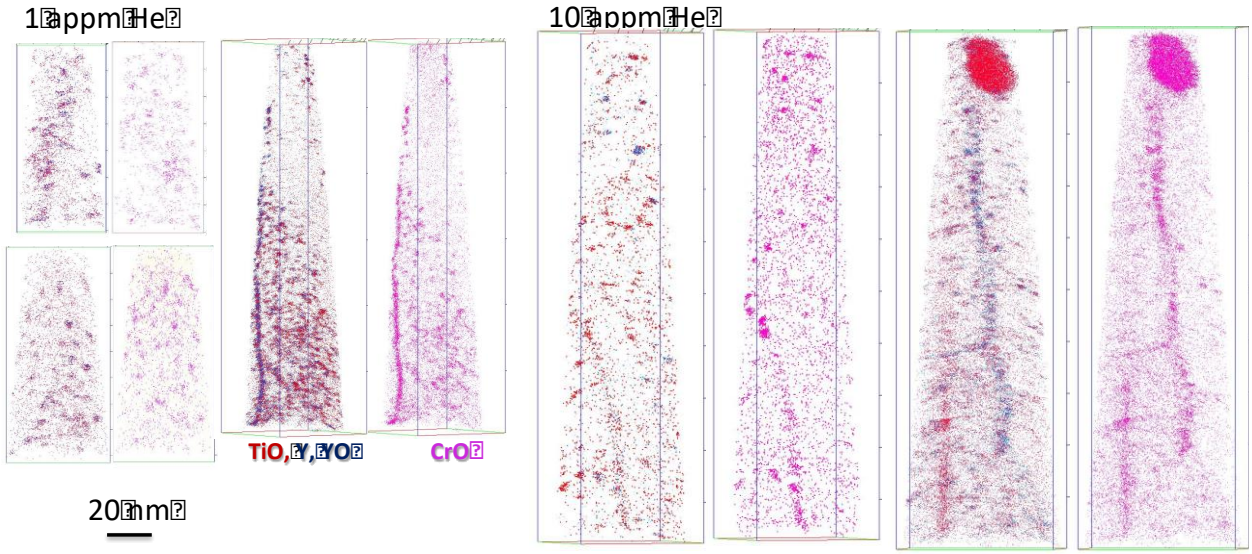

Figure 4.13. APT reconstructions obtained in 14YWT after irradiation to 40 dpa at 420°C. Only the elements partitioning to the clusters are shown (Three tips shown for 1 appm He and two tips shown for 10 appm He. For each tip the left image shows Y, YO and TiO all together; The right image shows the CrO clusters). The linear features correspond to grain boundaries imaged edge on.

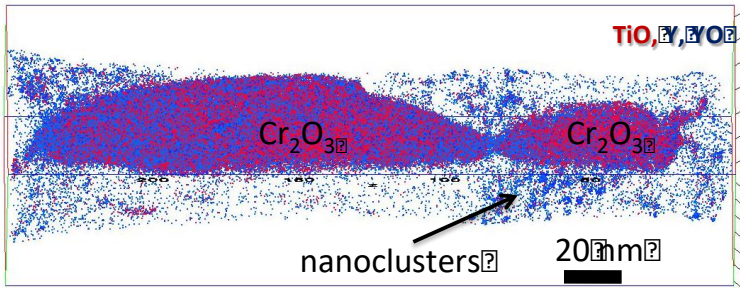

Figure 4.14. reconstruction containing larger oxide particles along a grain boundary in 14YWT.

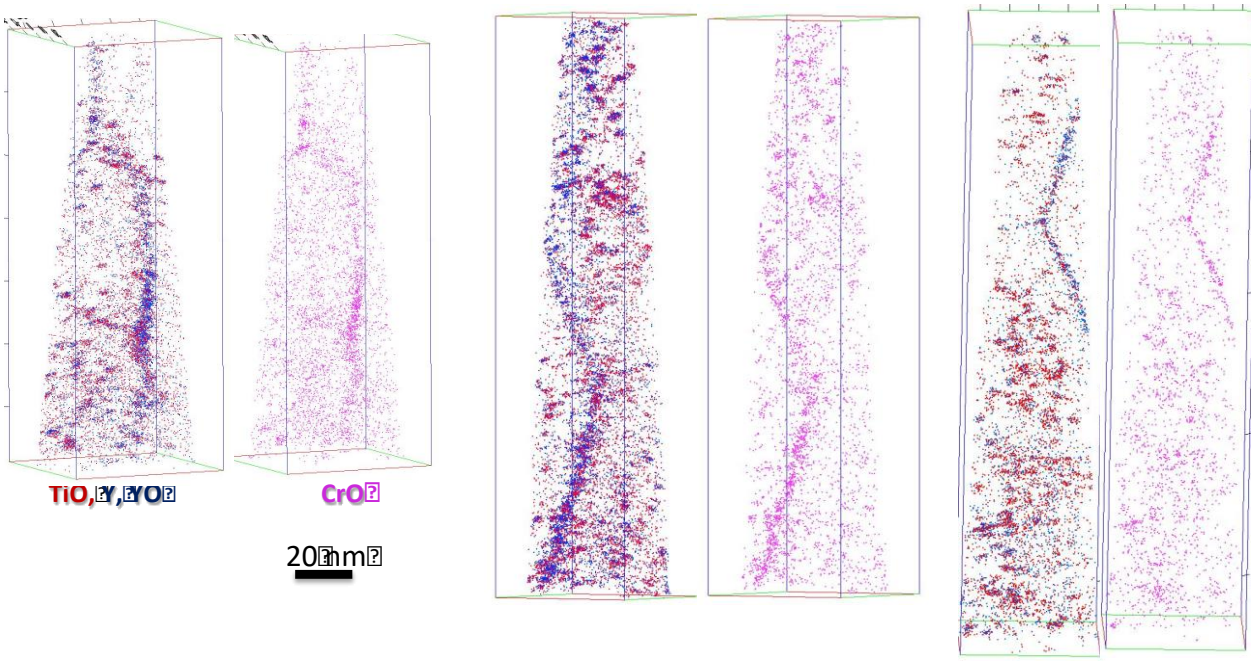

Figure 4.15. Reconstructions obtained after 80dpa and 1 appm He implantation. The left boxes are showing Y, YO and TiO while the right reconstructions show CrO. The linear features correspond to grain boundaries.

Table 4.4. Cluster compositions. The standard deviation was calculated from the different datasets.

	As received	**40 dpa**	**80 dpa**
Y	5.4	9.8 ± 0.9	10.8 ± 4.1
Ti	11.3	18.2 ± 1.8	20.3 ± 3.2
O	64.4	37.8 ± 7.4	44.8 ± 5.7
Cr	18.9	34.1 ± 6.3	24 ± 1.0
(Y+Ti)/O	0.9	0.8	1.3

4.3 Ion irradiation at 440°C to 150 dpa with 1 and 10 appm helium pre-implantation

TEM foils for HT9 irradiated at 440°C:150 dpa with 10appm He were prepared using FIB. Figure 4.16 shows a cross-sectional view of the entire foil, and Figure 4.17, at higher magnification, shows a view of some small voids (~10nm) seen near 600 nm deep. Only 8 voids/bubbles were observed in two lift-out samples and the average void size of 10.9 nm with a void density of 2.7×10^{20} m^{-3}. This results in a negligible swelling value of 0.0015%. The swelling value is in agreement with a previous irradiation of the same heat of alloy at a similar dose (440°C:140 dpa) with 0.0024% swelling. Characterization results of HT9 through the irradiated depth in 100nm increments are presented in Figure 4.18 and Figure 4.19, for 1 appm He and 10 appm He pre-implantation, respectively. The highest amount of swelling is observed near the surface (~0.004%) for both cases of He pre-implantation. However, voids at the surface are likely a surface effect. Preference on annihilation of interstitials at the surface due to their high mobility results in oversaturation of vacancies near the surface, which promotes nucleation of small voids. Furthermore, the dose of interest and target helium concentration are not represented within the first 300nm of the depth. Therefore the relevant swelling data should be considered beyond 300nm. Additionally, to avoid the effect of implanted interstitials, the area of interest must further be limited to less than 700nm. The resulting valid range for swelling is then 300nm – 700nm. To be more accurate in terms of irradiation dose, which was calculated at a depth 600nm, the range is further reduced to depth range of 500-700nm. Considering these limitations, the maximum swelling for this 1 appm He condition occurred in the range of 500-700nm is zero. For the case of HT9 at 440°C:150dpa:10appm He (Figure 4.19), the swelling is ~0.0015% at 500-700nm. Swelling is clearly higher in the 10 appm He implanted sample.

Figure 4.20 shows the formation of Ni/Si clusters in all four HT9 samples to similar doses at 440°C. The irradiations were conducted at three different dates (two of the irradiations (irradiation dates: 03/28/12 and 06/04/13) are from other project). The Ni/Si cluster size (2-3nm), density ($2\text{-}5\times 10^{22}/m^3$) are all in reasonable agreement. Note that samples were pre-implanted with two different levels of helium (10 appm and 100 appm). The amount of pre-implanted helium does not appear to affect formation of the Ni/Si-rich G-phase precipitates.

Swelling of NF616 irradiated to 440°C:150dpa and to 460°C:188dpa with 1 and 10appm helium were analyzed with TEM. He implantation was carried out prior to the irradiation experiment with 1 appm He on one half of the bar and 10 appm He on the other half. TEM specimens were prepared by the standard lift-out method and Ga ion milling. Prior to the ion milling the specimens were deposited with a Pt layer to protect the materials underneath from ion beam damage. In the final step of the TEM sample thinning a 5kV Ga milling cleaning was utilized for one minute on both sides of the TEM foil to further reduce the beam damage. TEM observations were conducted on a JEOL 2010F microscope operated at 200kV.

Dislocations along various zone axes were observed using bright field STEM (BF-STEM). STEM observations were conducted on the same microscope using a probe size of 0.2nm with a camera length of 15cm. Bright-field STEM images were acquired using a GATAN circular bright filed detector.

No voids were observed in NF616 at 440^{o}C:150dpa:1 appm He. Voids in 440^{o}C:150dpa:10appm He are indicated with arrows in Figure 4.21(a). Voids can be clearly observed from bright field images in a slightly under focus condition. The size distribution obtained from 153 voids indicates an average size of 6 nm in diameter, with a maximum void density at 650 nm from the sample surface, Figure 4.21b and c. Number density and swelling as a function irradiation depth are shown in **Figure 4.22**. There were about 60 voids in the 500-700 nm depth region with an estimated number density of ~4 × 10^{20} m^{-3} and swelling of ~0.006%. The average void size is smaller but the density is higher in NF616 compared to HT9. However, the resulting swelling values are very comparable. As shown in Figure 4.23, dislocations along [111] and [001] were observed using BF-STEM. In Figure 4.23(a), the linear features with dark contrast about 40-50nm in length could be 1/2a <110> dislocation loops, but further confirmation is needed as this type of loops is not commonly observed in irradiated F-M alloys

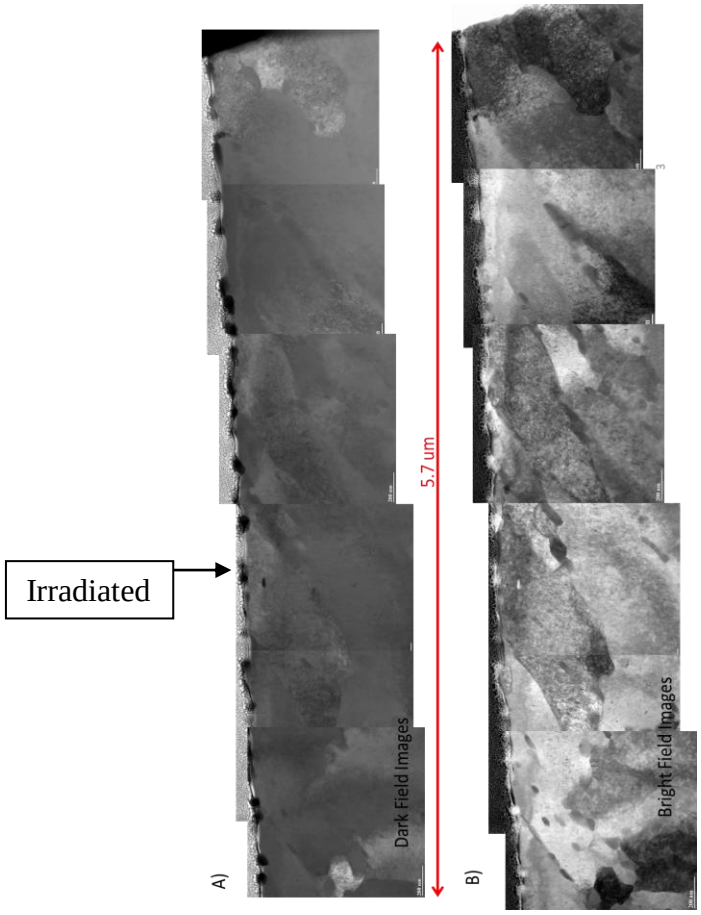

Figure 4.16. Cross-sectional TEM images of the HT9 440°C:150dpa with 10 appm He pre-implantation condition in both A) high annular dark field and B) bright field are shown above.

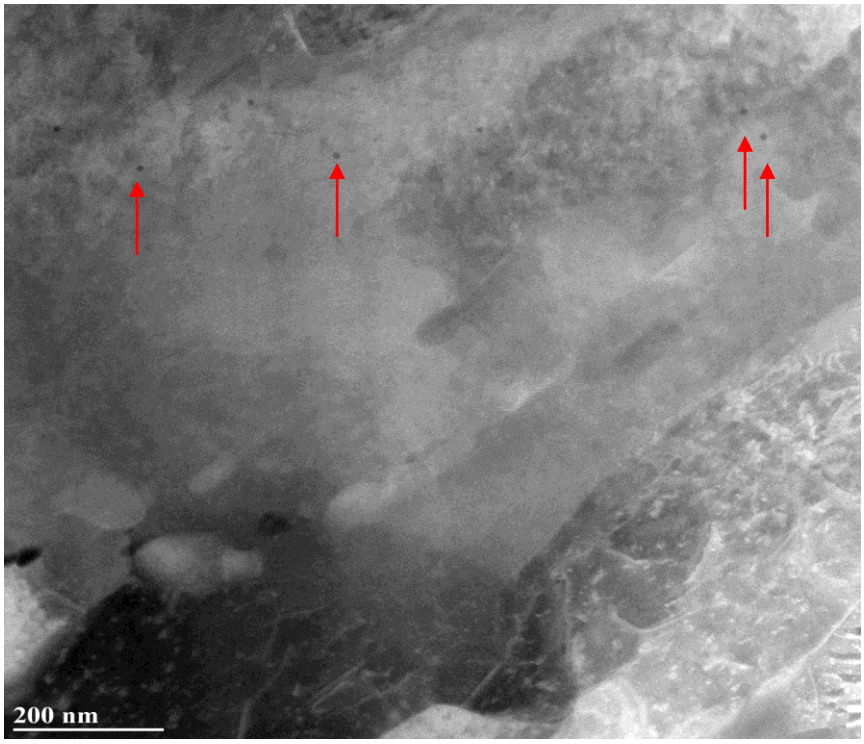

Figure 4.17. Voids (some indicated by red arrows) in HT9 irradiated at 440°C:150 dpa at a depth corresponding to the implanted helium (0.5-1µm). The irradiated surface is above the image, which is not shown.

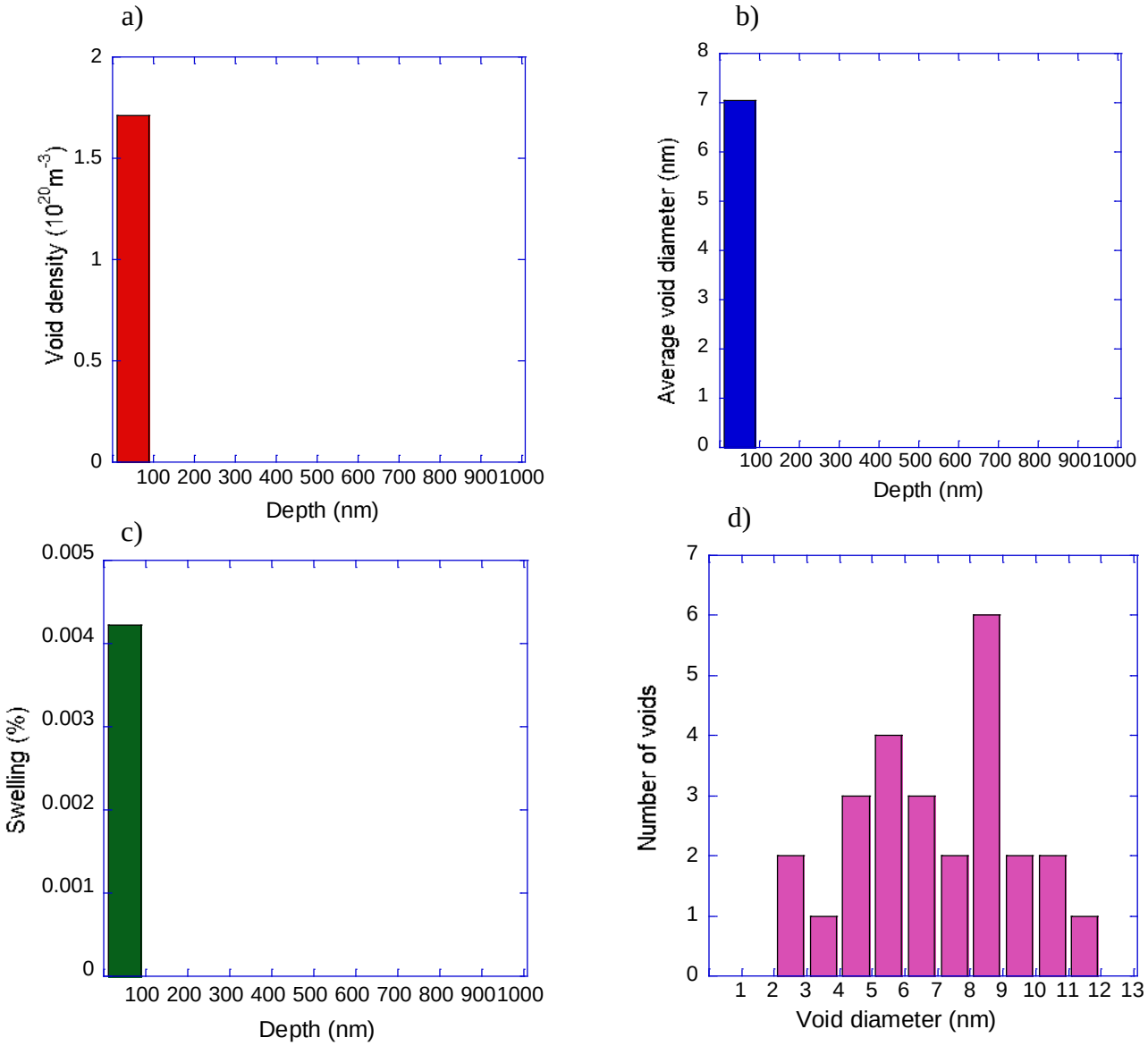

Figure 4.18. Analysis of a) void density, b) average void diameter and c) swelling in 100nm increments through the depth of the HT9:440C:150dpa:1 appm He condition is shown. Plot d) shows the size distribution of the void.

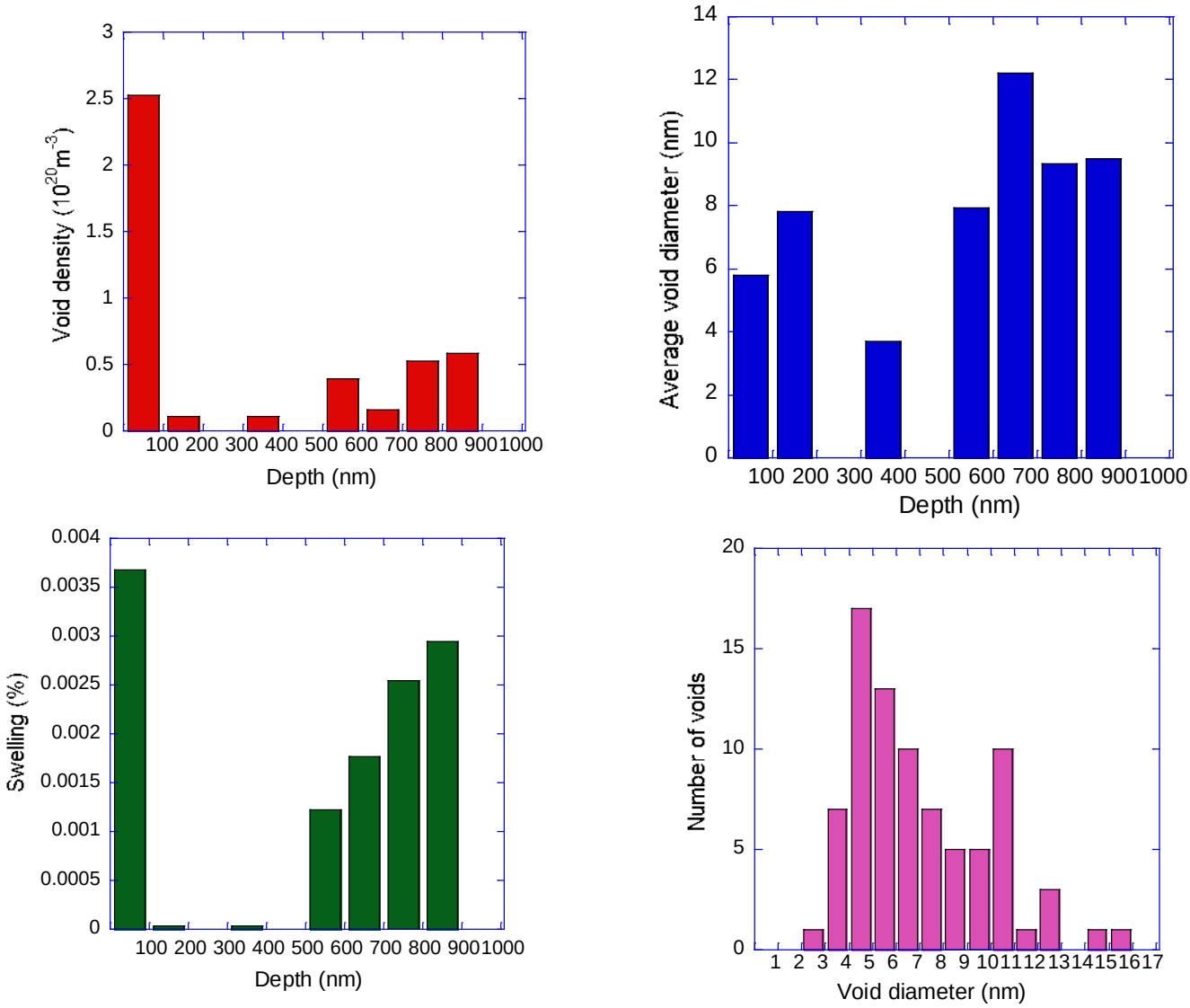

Figure 4.19. Analysis of a) void density, b) average void diameter and c) swelling in 100nm increments through the depth of the HT9:440C:150dpa:10 appm He condition is shown. Plot d) shows the size distribution of the voids.

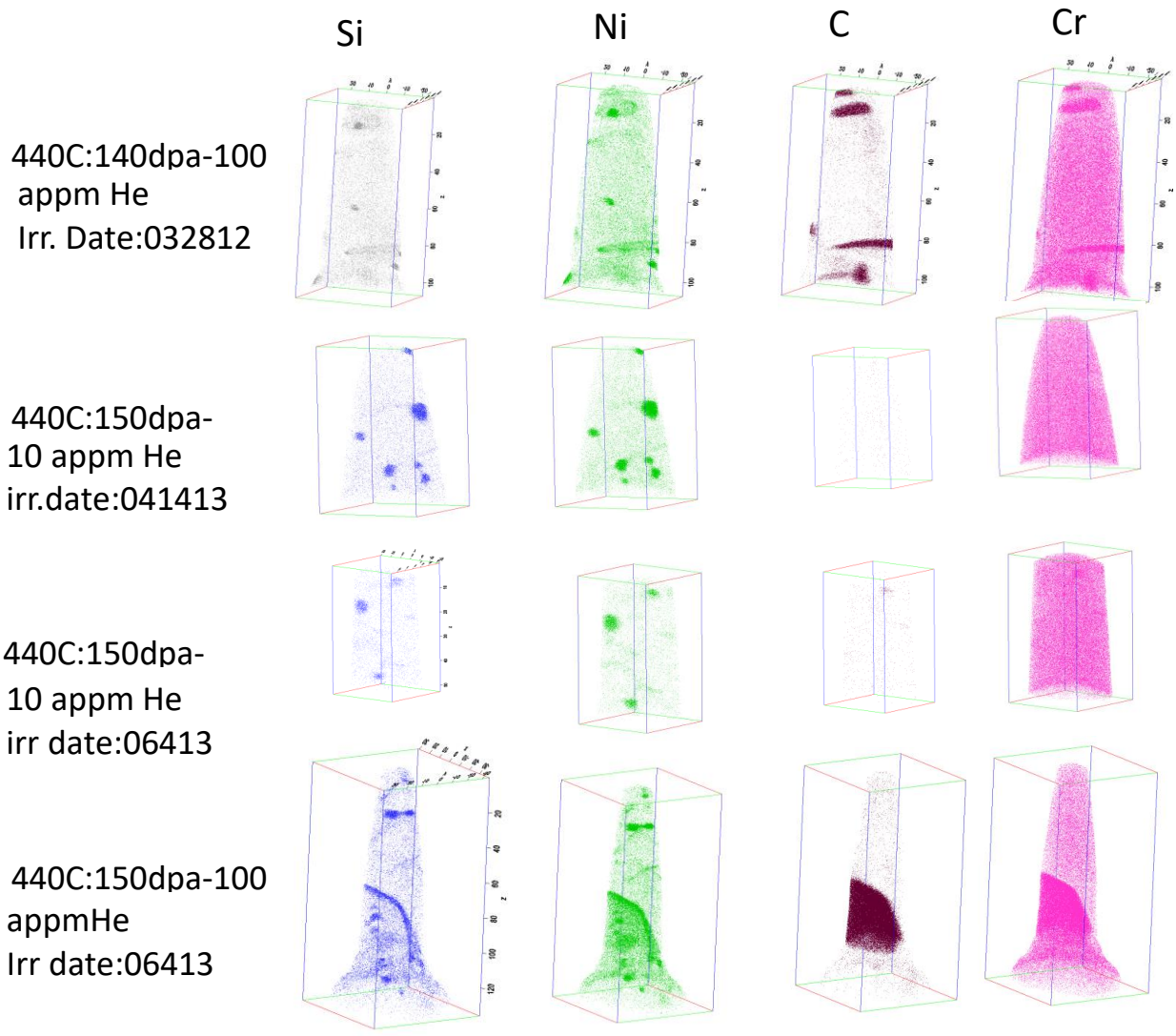

Figure 4.20. APT showing formation of Ni/Si clusters in all four HT9 samples to similar doses at 440°C conducted at different irradiation dates.

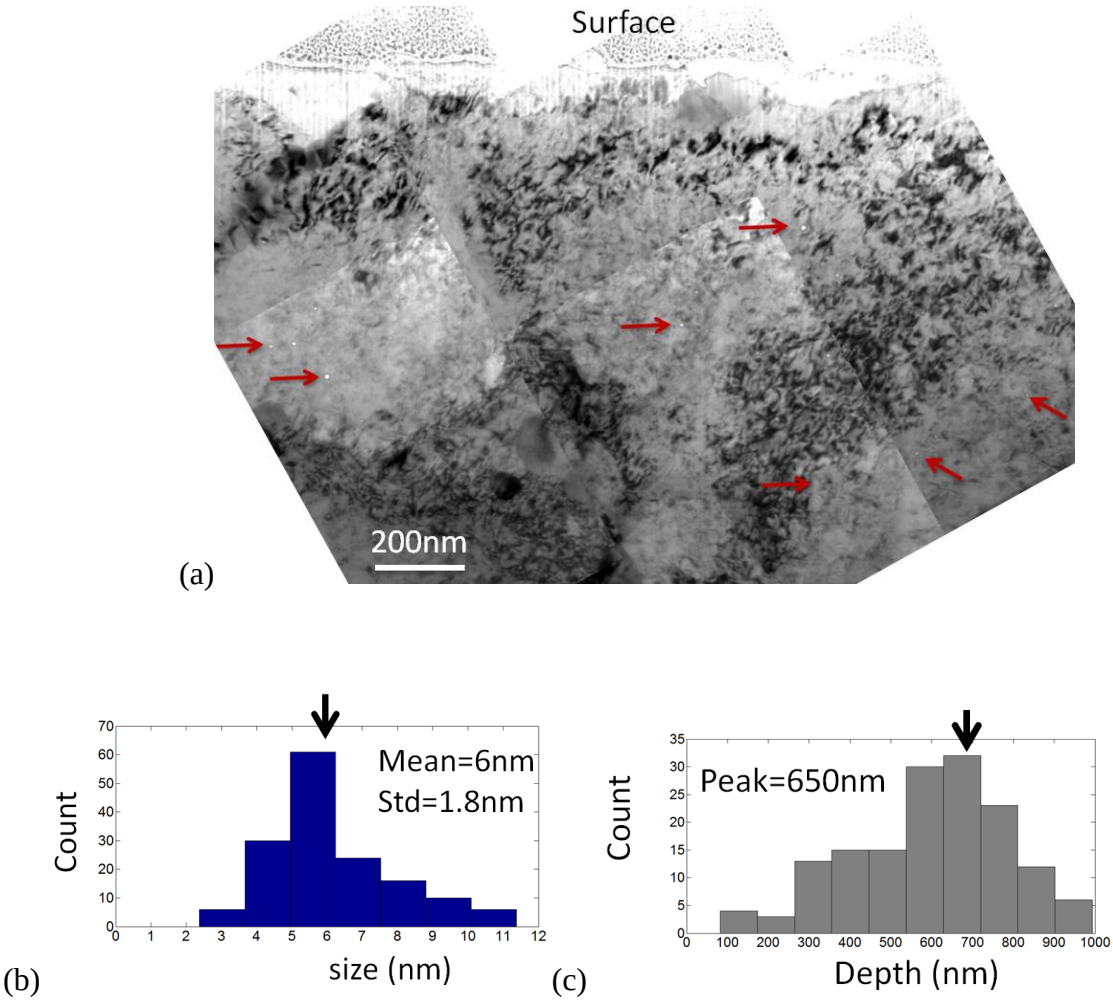

Figure 4.21. (a) Bright filed image of nano-sized cavities in NF616 at 440°C:150dpa:10 appm He. (b) size distribution (in diameter) and (c) depth distribution of 153 voids observed.

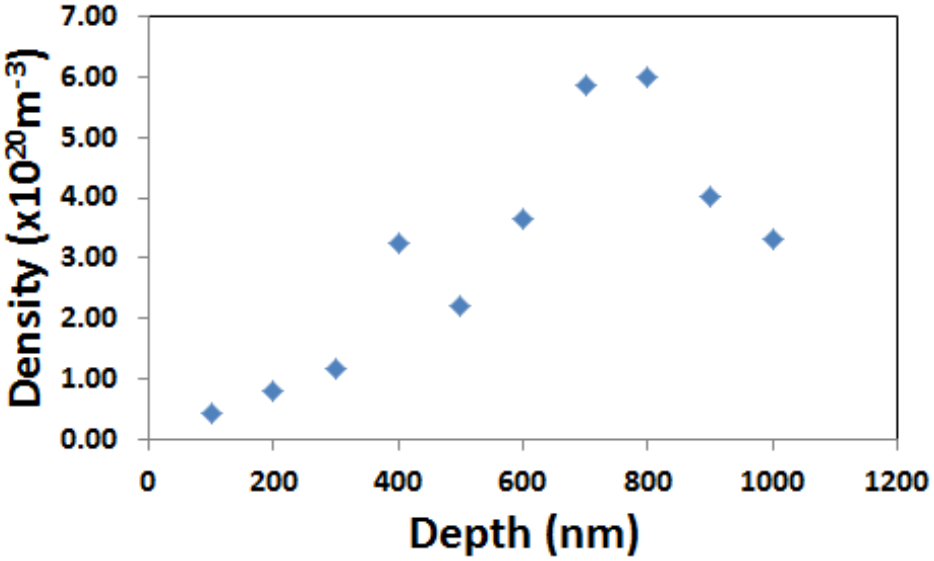

a

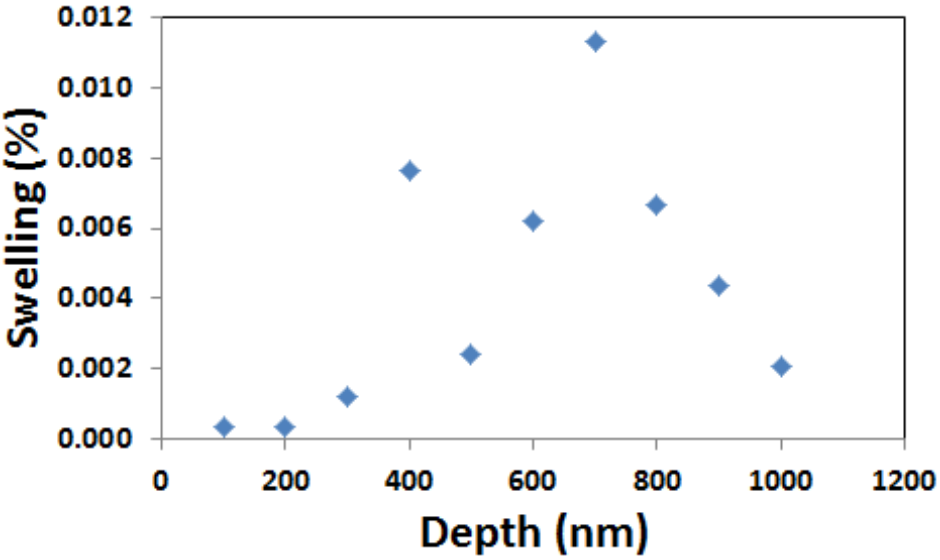

b

Figure 4.22. (a) Number density and (b) swelling as a function irradiation depth in in NF616 at 440°C:150dpa:10 appm He.

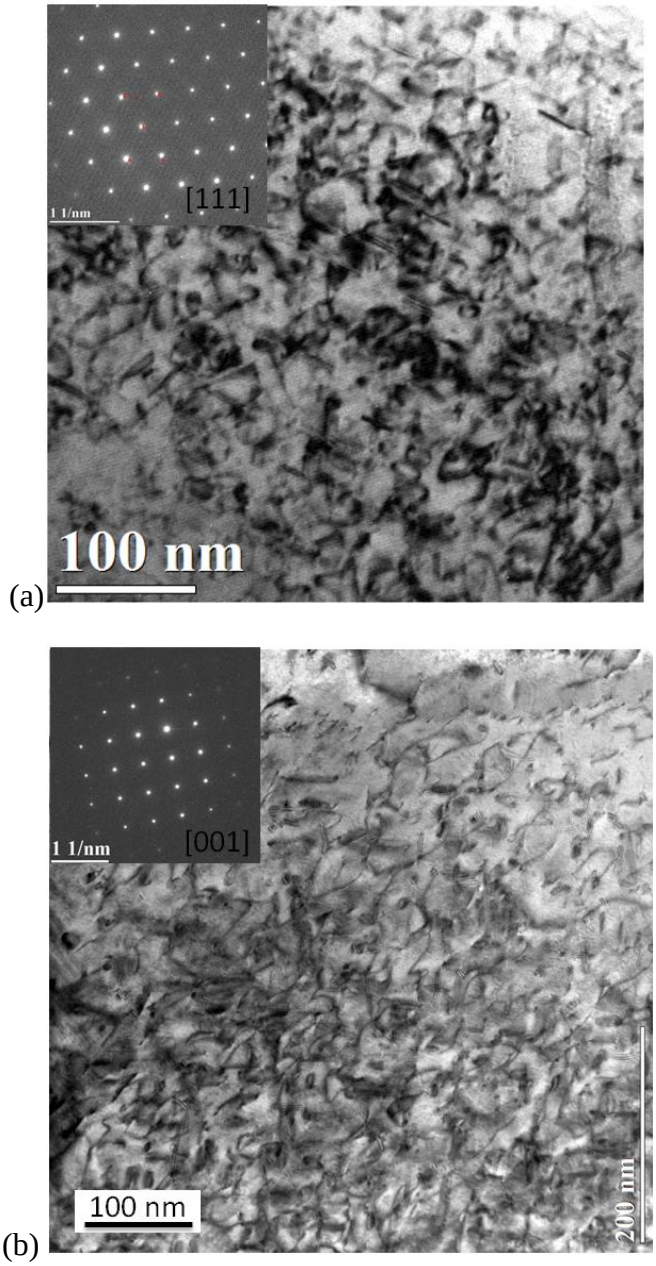

Figure 4.23. BE-STEM images obtained from NF616 at 440°C:150dpa:10 appm He. BF-STEM image along (a) [111] and (b) [001] colleted from a region about 500-700 nm from the surface showing dislcoations.

4.4 Ion irradiation at 460°C up to 450 dpa with 10 appm helium pre-implantation

Analysis through the depth of the lift-out was first performed on HT9 at 460°C:188dpa with 10 appm helium pre-implantation. Dark field HAADF images were taken along the length of the entire lift-out, and are shown in Figure 4.24. The number density, average size, swelling and distribution plots are shown in Figure 4.25. Similar to the previous results, a high concentration of voids was observed at the surface. However this condition exhibited considerably higher densities and average void sizes, resulting in much higher swelling values in the region of 300-700nn. A peak swelling value of 5.47% was observed in the 600-700nm band. An important feature to note is the drop in swelling after the 700-800nm band, following the 600-700nm band. This is likely due to the effect of implanted iron ions as the dose is higher and the helium concentration is 10 appm in this region. Figure 4.26 shows the STEM images taken for HT9 at 460°C:188dpa with 1 appm helium pre-implantation. Clearly fewer voids were observed in the 1 appm He case than in the 10 appm He case, but they are still very noticeable in the region of interest. Figure 4.27 shows the compiled depth distributions for the 1 appm He case. Maximum swelling occurred in the 500-600nm region with a value of 0.68%. Images of T91 from the 460°C:188 dpa irradiation have also been taken from both the 10 appm He and 1 appm He regions. These images are shown in Figure 4.28 and Figure 4.29, respectively. However, visually the T91 seems to behave similarly to the ACO3 in response to the amount of implanted helium, with a much larger void sizes and densities in the 10 appm He case than in the 1 appm He case.

Figure 4.30 shows HT9 irradiated to 450dpa at 460°C with 1 appm He pre-implantation. A slight increase in swelling from 375 dpa was observed (2.69% to 2.88%). The increase in swelling was due to growth of the voids, as the diameter increased from 35.4nm to 53.4nm. The number density showed a small decrease from 5.88 x $10^{20}m^{-3}$ to 2.39 x $10^{20}m^{-3}$. Swelling was also observed in T91 at 450 dpa, with 1 appm He. A swelling value of 2.15% resulted from voids of diameter of 45.4nm and a density of 9.55 x $10^{20}m^{-3}$. A summary of the data (including all of the 375 dpa data) is given in Table 4.1 (for HT9) and Table 4.2 (for T91).

To examine the void incubation dose for HT9 and T91 at 460°C, irradiation was conducted at a much lower dose of 75 dpa. HT9 implanted with 100 appm He exhibited a swelling value of 0.0014%, with an average void diameter of 10.6nm, a density of 0.42 x $10^{20}m^{-3}$ resulting from only 5 voids counted in the valid region. T91 implanted with 10 appm He exhibited higher swelling, with a value of 0.075%, with an average void diameter of 20.9nm, a density of 1.0 x $10^{20}m^{-3}$, resulting from a total of 25 voids. Except the HT9 implanted with 100 appm He, and T91 implanted with 10 appm He, no void was observed in any other conditions in the valid 300-700nm region at 75 dpa, resulting in 0% swelling. This irradiation condition (460°C:75dpa) probably mark the lowest dose where swelling was observed with either 10 or 100 appm of implanted helium. The densities at this condition are much lower than that observed at 375 dpa, which indicates that voids are still in the nucleation phase and that steady state has yet to be reached. However, steady-state swelling is likely achieved before 188 dpa where densities have reached their highest ($4.77 \times 10^{20}m^{-3}$) and where they remain through 375 dpa. Thus, this irradiation has provided valuable bounds on the incubation dose required for void swelling.

Figure 4.31(a) shows voids in NF616 at 460°C:188dpa:10appm He that are densely concentrated at the region of 500-1000 nm from the surface. The depth distribution of 503 voids indicates a maximum density is reached at 650 nm from the surface, which agrees with the result obtained from sample at 440°C. Number density and swelling as a function irradiation depth in NF616 at 460°C:188dpa:10appm He is shown in Figure 4.32. The number density was estimated to be $1.0x10^{22}$ m^{-3} and the swelling was estimated to be 0.7% at the depth of 500-700 nm. The average diameter of void was 20-30 nm. The size distributions of voids for both temperatures with 10 appm are compared in
Figure **4.33**, showing a clear shift to larger voids as irradiation temperature and dose level increase.

Voids in NF616 irradiated at 460°C to 375 dpa with 1 appm and 10 appm helium pre-implantation are shown in Figure 4.34a and b, respectively. The void number density and swelling as a function of irradiation depth are shown in Figure 4.35 and Figure 4.36, respectively. The void number density was estimated to be 3.0×10^{21} m^{-3} and the swelling was estimated to be ~1.0 % at the depth of 500-700 nm for the case of 1 appm helium pre-implantation. Both void number density and swelling are higher in the 10 appm helium case with a number density of 1.6×10^{22} m^{-3} and swelling value of ~4%.

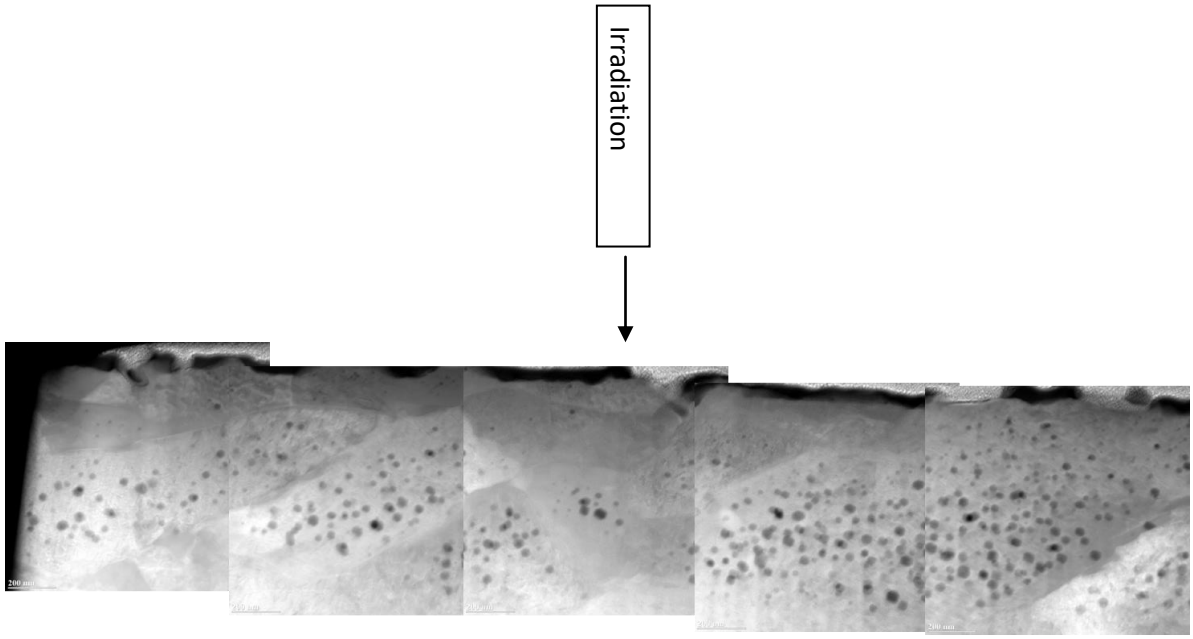

Figure 4.24. An overview of the HT9 sample with 10appm helium at 460°C:188dpa. A high density of voids was observed in the irradiated region.

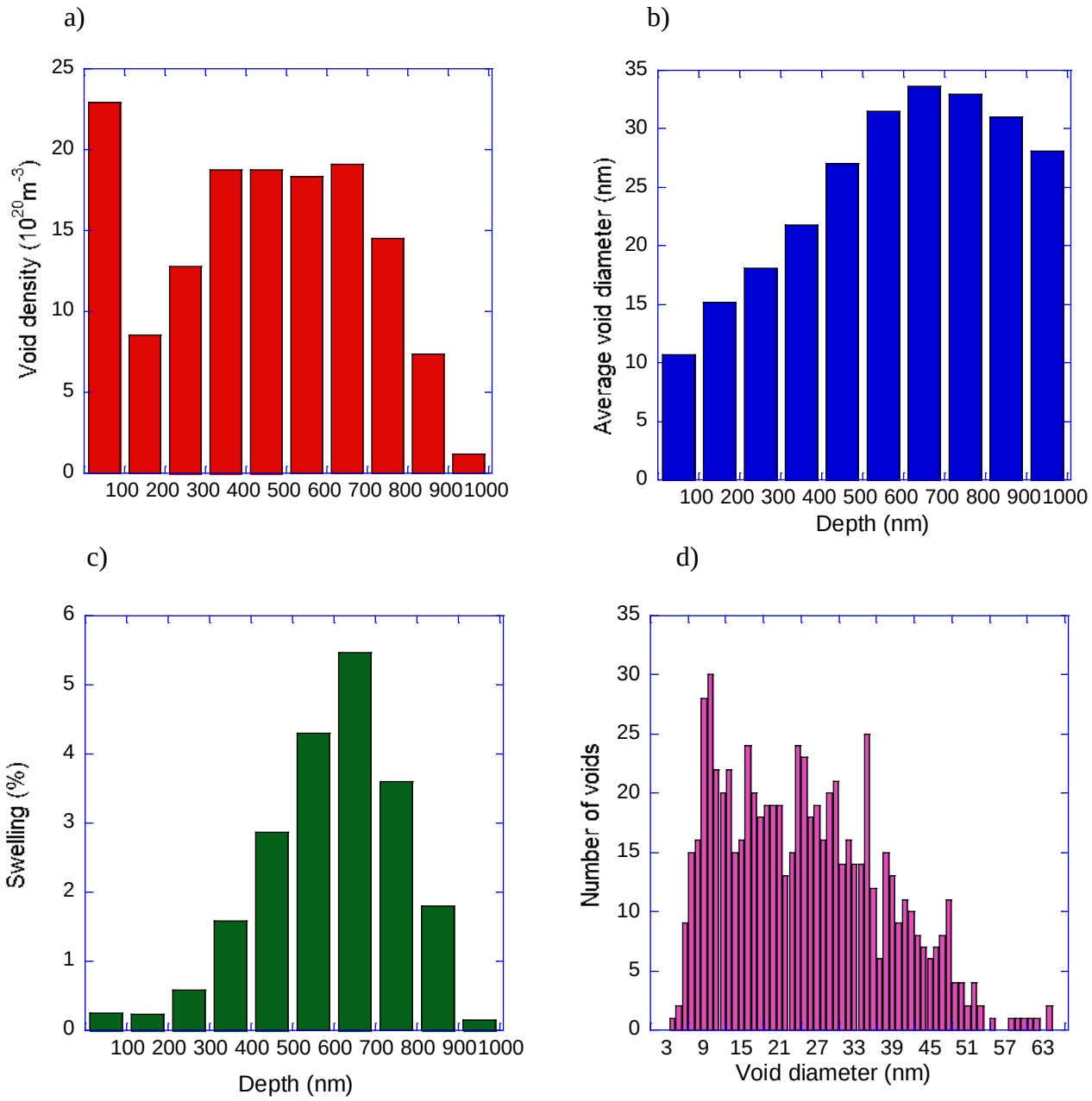

Figure 4.25. Analysis of a) void density, b) average void diameter and c) swelling in 100nm increments through the depth of the HT9:460°C:188dpa:10appm He condition is shown. Plot d) shows the size distribution of the voids.

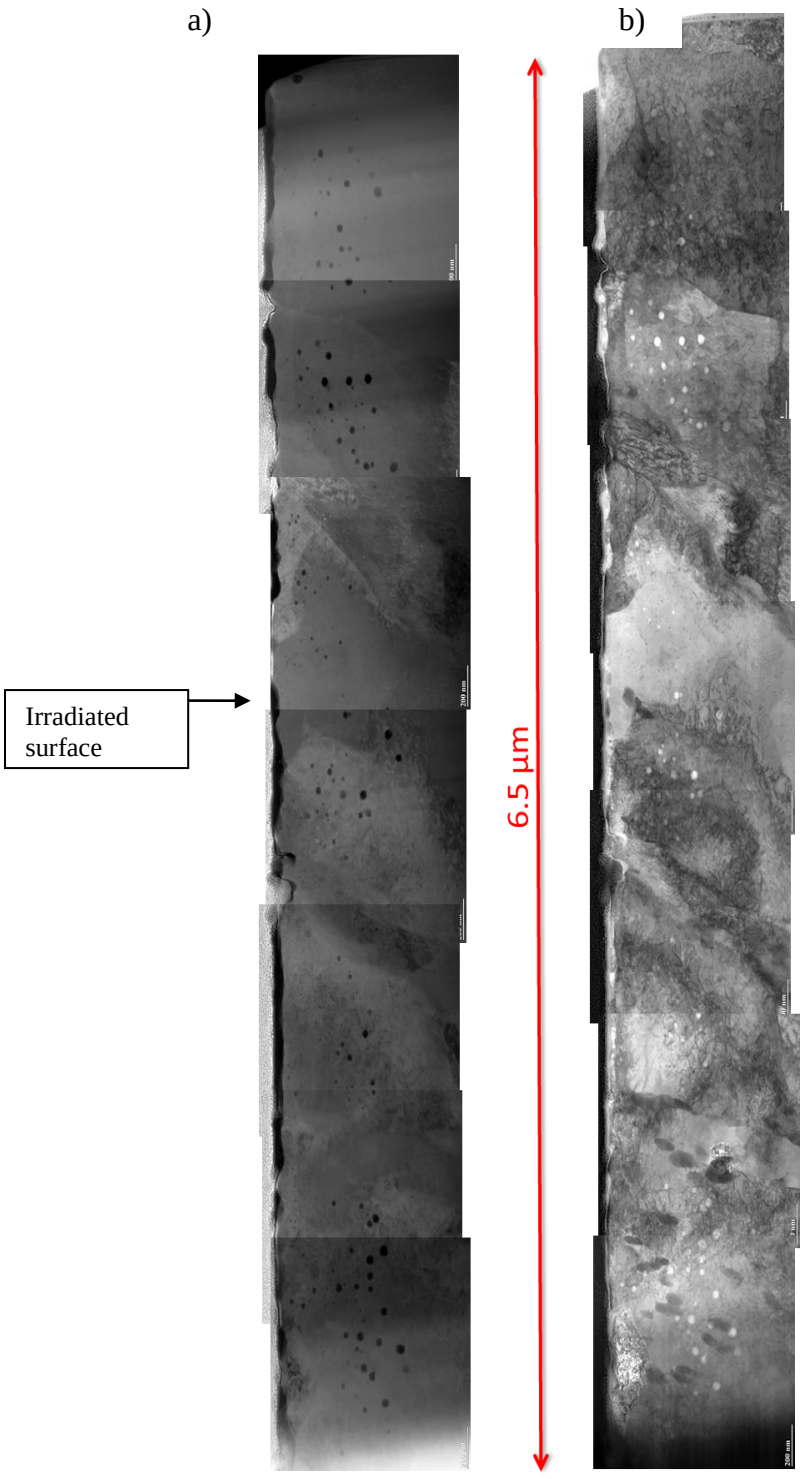

Figure 4.26. a) STEM dark field and b) bright field images of the HT9:460C:188dpa:1appmHe samples.

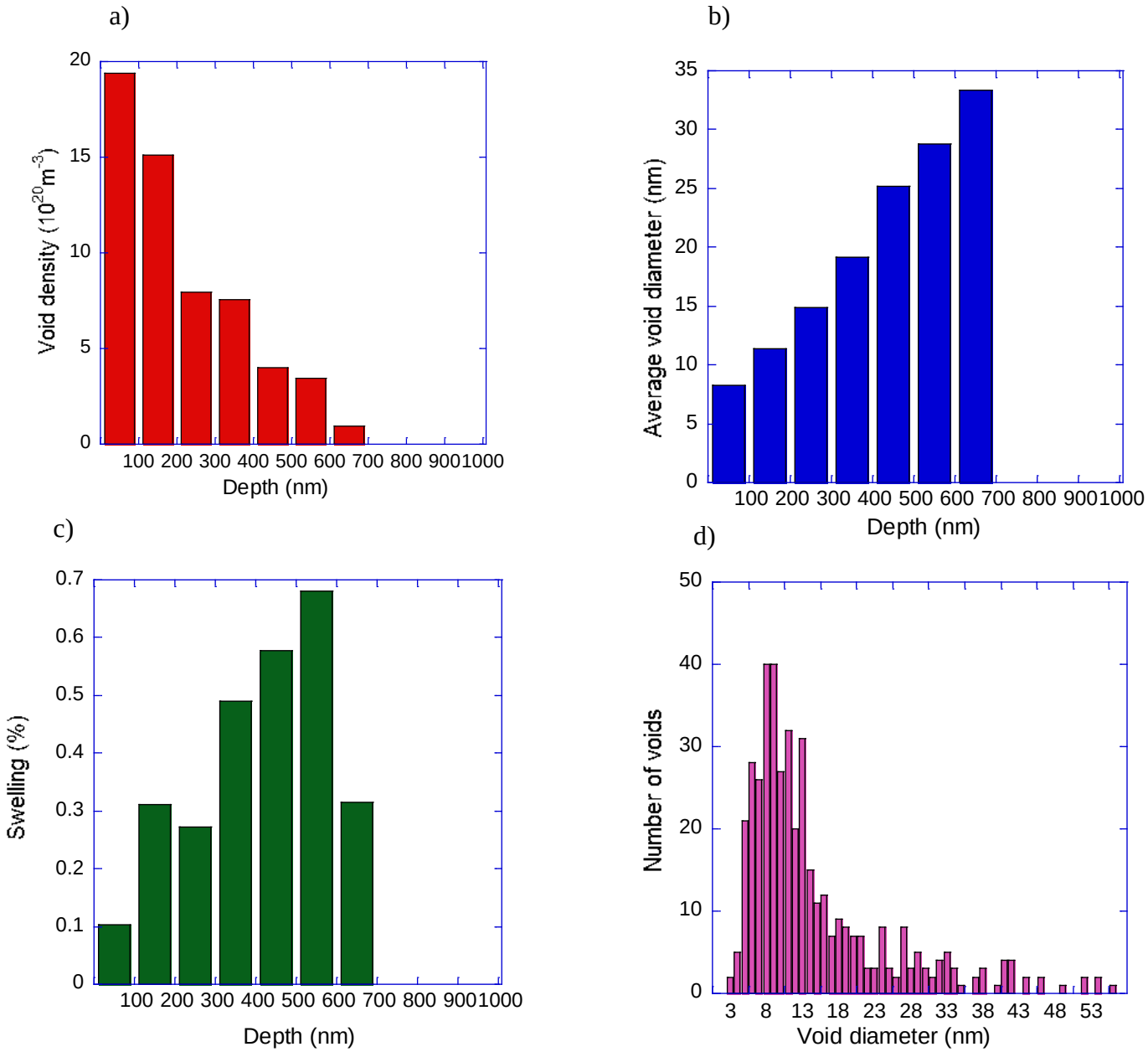

Figure 4.27. Analysis of a) void density, b) average void diameter and c) swelling in 100nm increments through the depth of the HT9:460°C:188dpa:1appm He condition is shown. Plot d) shows the size distribution of the voids.

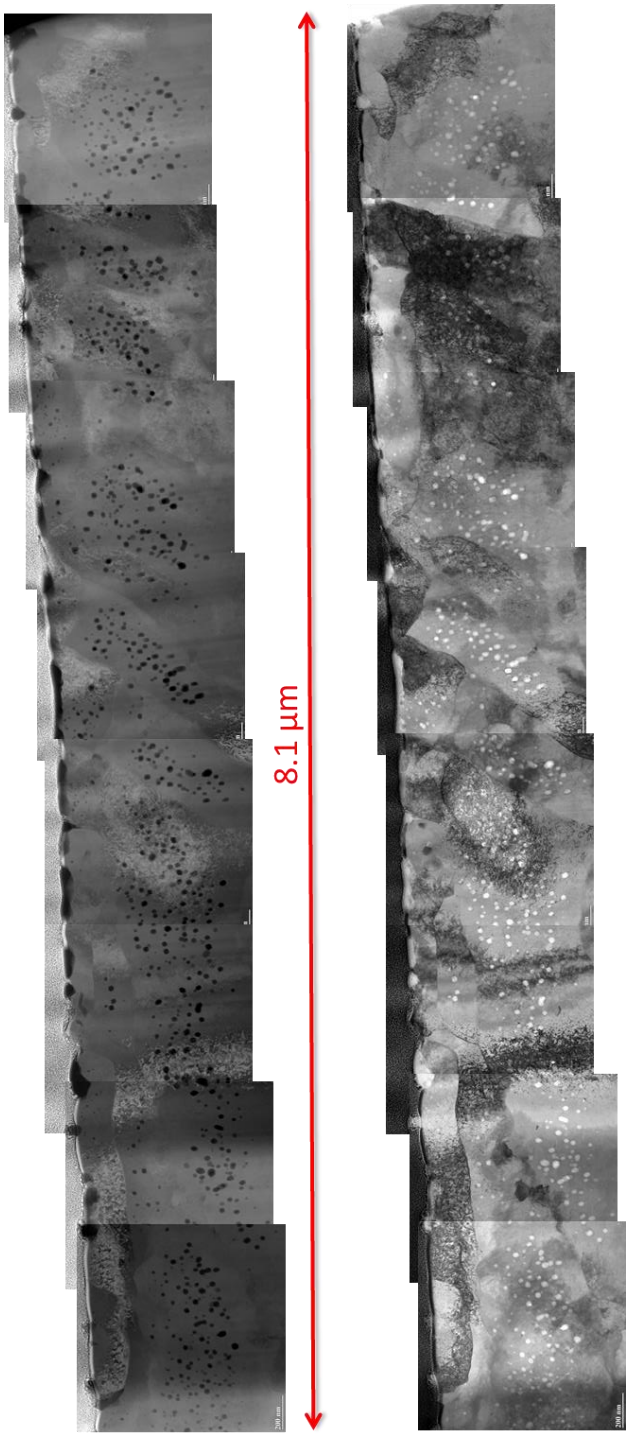

Figure 4.28. a) Dark field and b) bright field images of the T91:460°C:188dpa:10appm He samples.

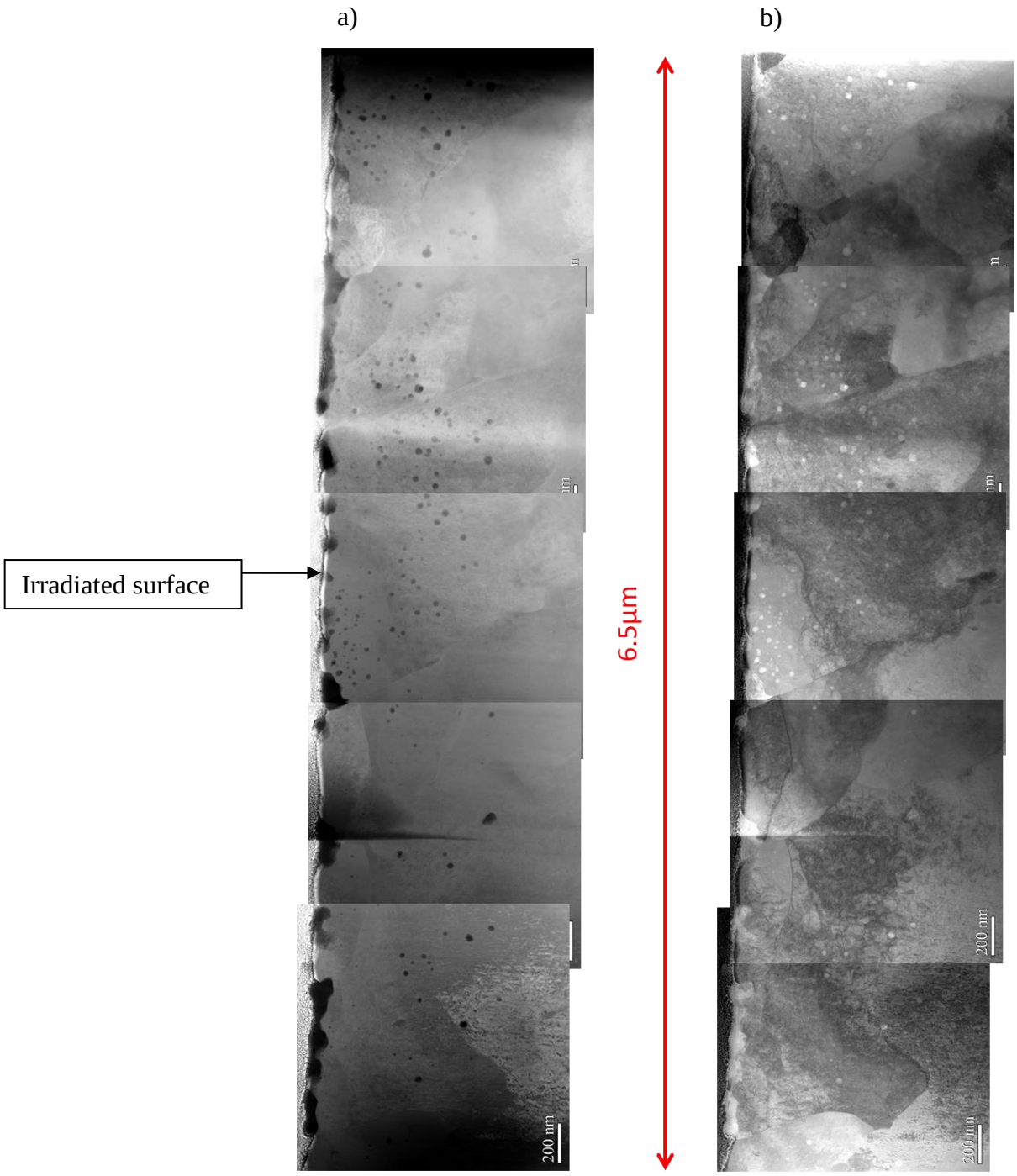

Figure 4.29. a) Dark field and b) bright field images of the T91:460°C:188dpa:1appm He samples.

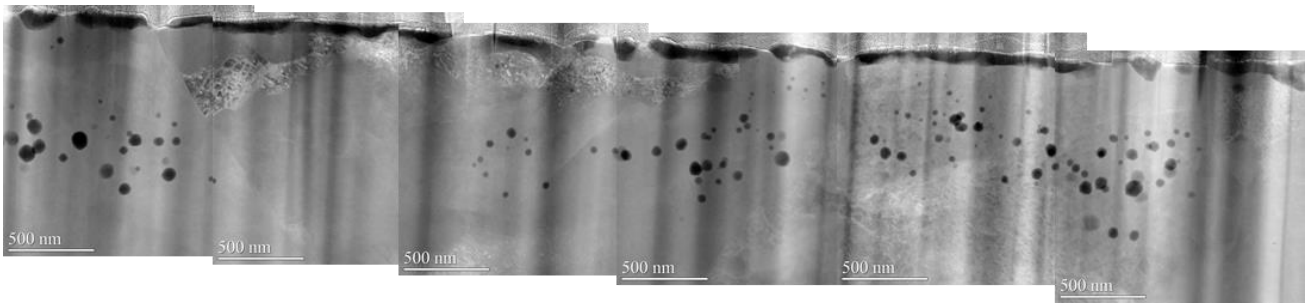

Figure 4.30. A HAADF image of the HT9:460ºC:450dpa:1He condition is shown above.

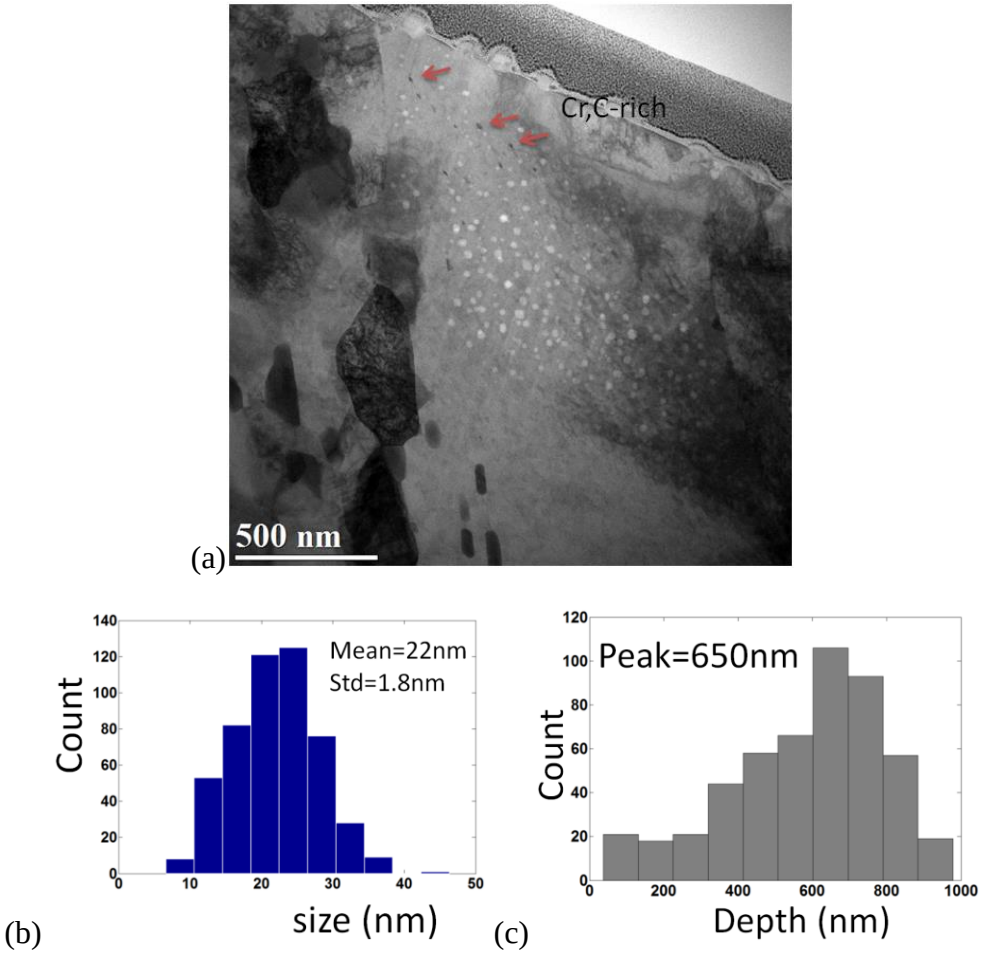

Figure 4.31. (a) Bright filed image of voids in NF616 at 460°C:188dpa:10 appm He. (b) size distribution (in diameter) and (c) depth distribution of voids calculated from 503 voids.

(a)

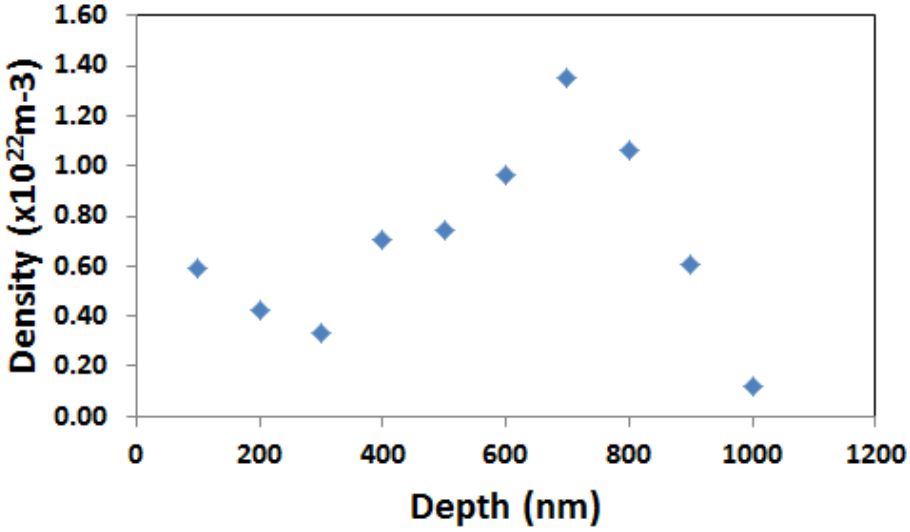

(b)

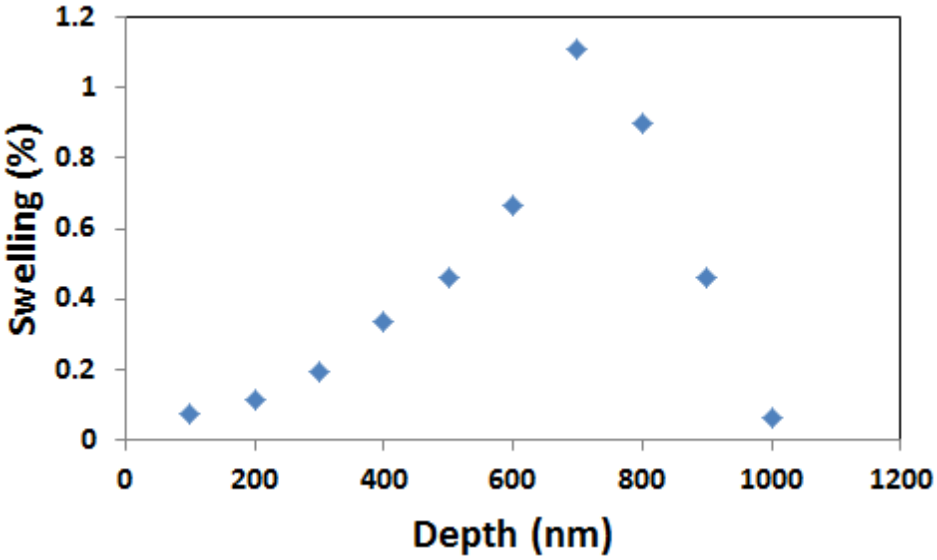

Figure 4.32(a) Number density and (b) swelling as a function irradiation depth in in NF616 at 460°C:150dpa:10 appm He.

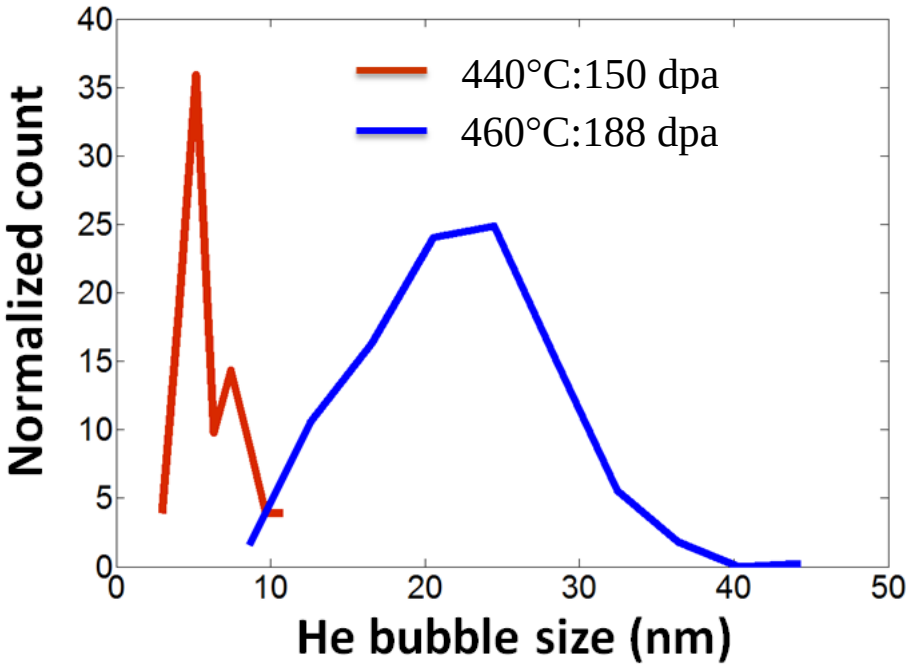

Figure 4.33. Comparison of void size distirbution for NF616 at 440°C:150dpa:10appm He and 460°C:188dpa:10 appm He .

(a)

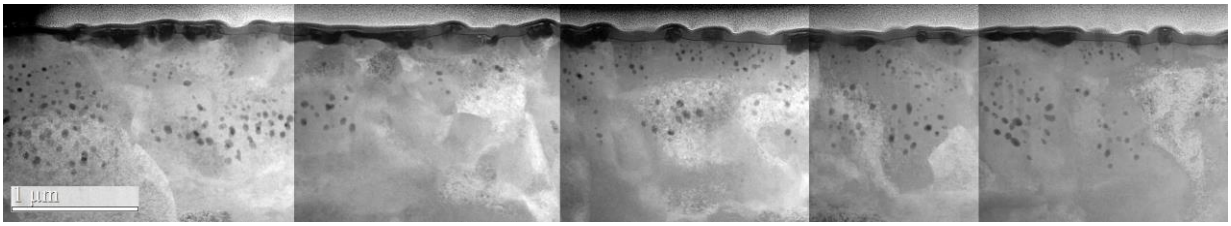

(b)

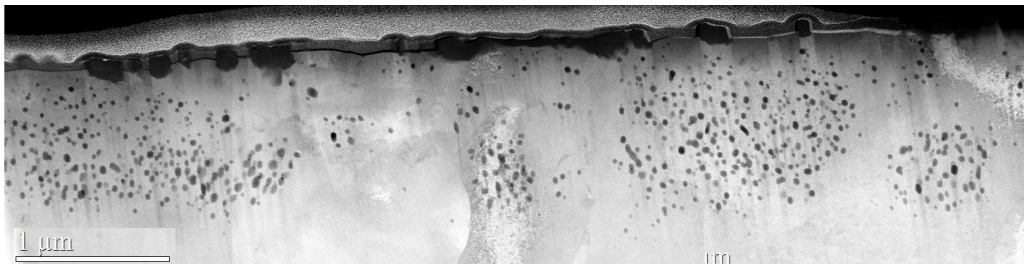

Figure 4.34. STEM HAADF image showing voids in NF616 irradiated at 460°C to 375 dpa with (a) 1 appm and (b) 10 appm helium pre-implantation.

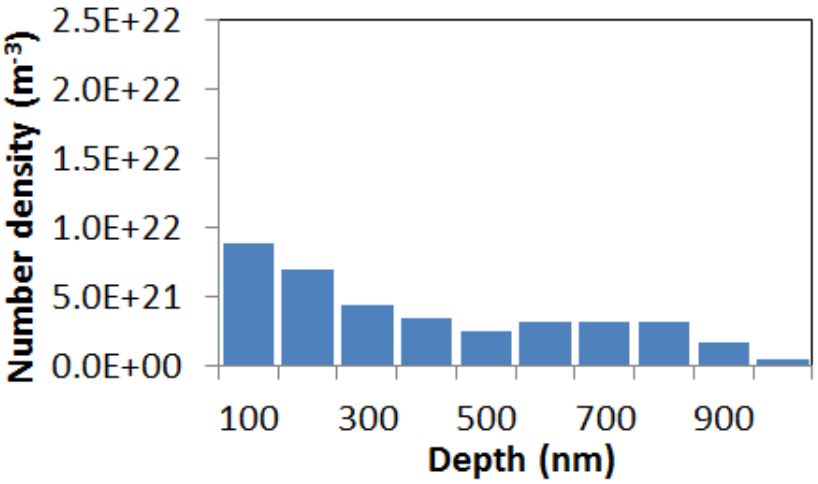

6.1

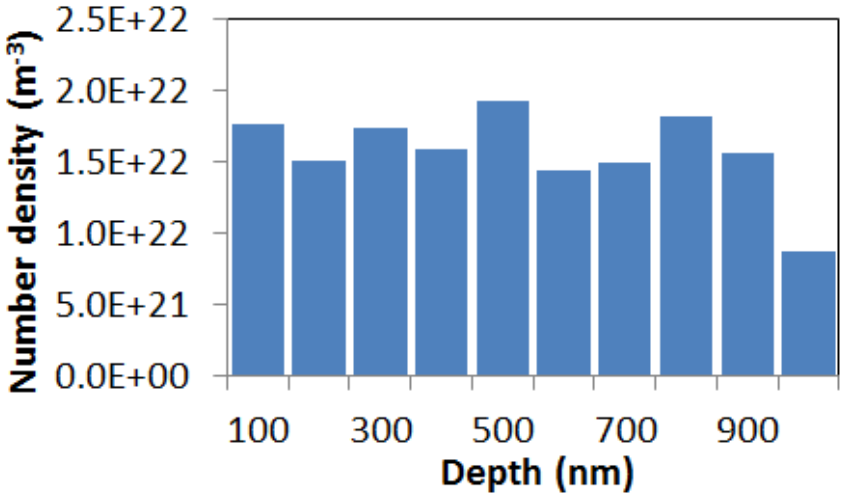

(b)

Figure 4.35. Void number density as a function of depth for NF616 irradiated at 460°C to 375 dpa with (a) 1 appm and (b) 10 appm He pre-implantation. There are 472 voids in (a) and 751 voids in (b).

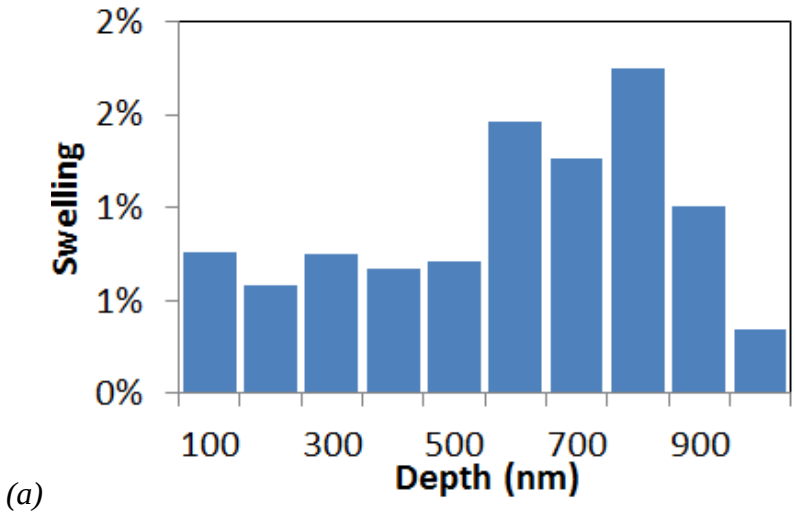

(a)

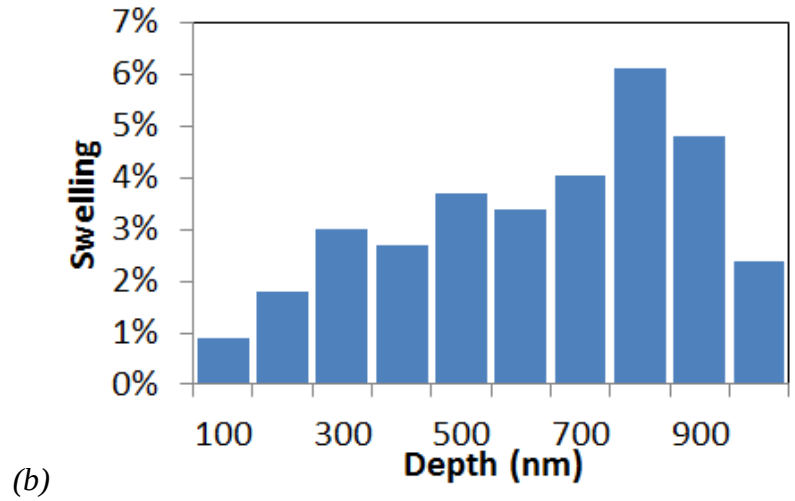

(b)

Figure 4.36. Swelling as a function of depth in NF616 irradiated at 460°C to 375 dpa with (a) 1 appm and (b) 10 appm He pre-implantation.

4.5 Swelling in T91 heat C2269 with helium pre-implantation up to 1000 appm at 460°C

In addition to studying the effects of temperature and alloy, it was also very important to explore the effect of different levels of pre-implanted helium to understand its effect on the cavity microstructure from nucleation to growth. A series of irradiations was performed at 460°C using alloy T91 C2269 with helium levels varying from 0, 1, 10, 100, and 1000 appm He. The samples were coated with 100nm alumina to prevent carbon contamination during self-ion irradiation. Figure 4.37 show the swelling behavior as a function of damage for the coated samples. Sample without helium shows the highest swelling at 300 dpa, followed by 1, 10, 100 and 1000 appm in decreasing swelling order.

Figure 4.38 shows how the cavity densities (including nanocavities) in the coated samples evolve with damage. In all of the helium implanted cases, the density is already established by 50 dpa and does not change with increases in damage up to 300 dpa. However, the 0 appm He case appears to slowly approach the density of 1 and 10 appm He cases by 300 dpa. Figure 4.39 shows how the size of cavities varied with damage. At all observed damage levels, the 0 appm He case exhibited the largest size, suggesting that the cavities were growing faster than the pre-implanted conditions. The swelling drops with increasing helium levels because the excessive nucleation causes the vacancies to be diluted between many cavities, thus suppressing growth overall. This is especially evident in the 100 and 1000 appm He cases, which exhibited an extremely high density of nanocavities (see Figure 4.40). These nanocavities in aggregate do not contribute much at all to swelling, but are likely the cause of the reduction of swelling as they serve as sites for recombination and dilution of vacancies. Figure 4.41 shows swelling as a function of helium level at 50 dpa. The swelling peaked at 10 appm helium, which is different than swelling peak at high dose (peaked at 0 helium).

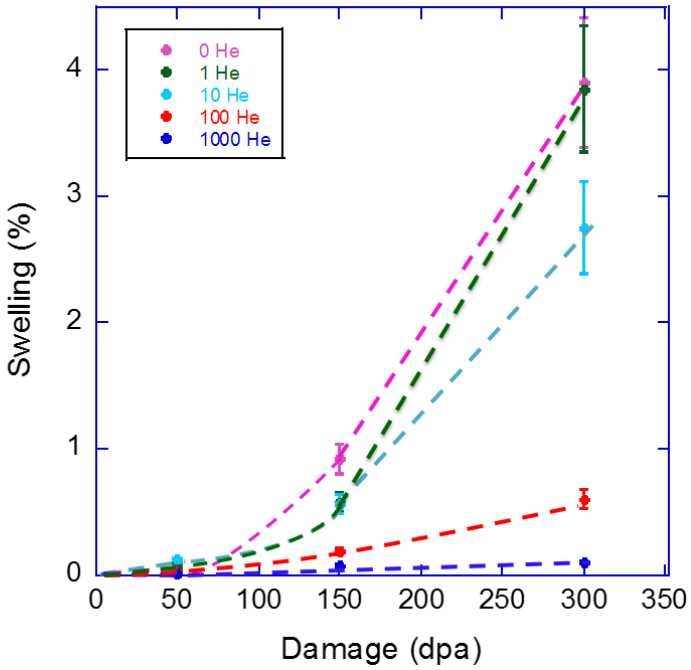

Figure 4.37. Swelling as a function of damage is shown for the alumina-coated T91 C2269:460°C condition

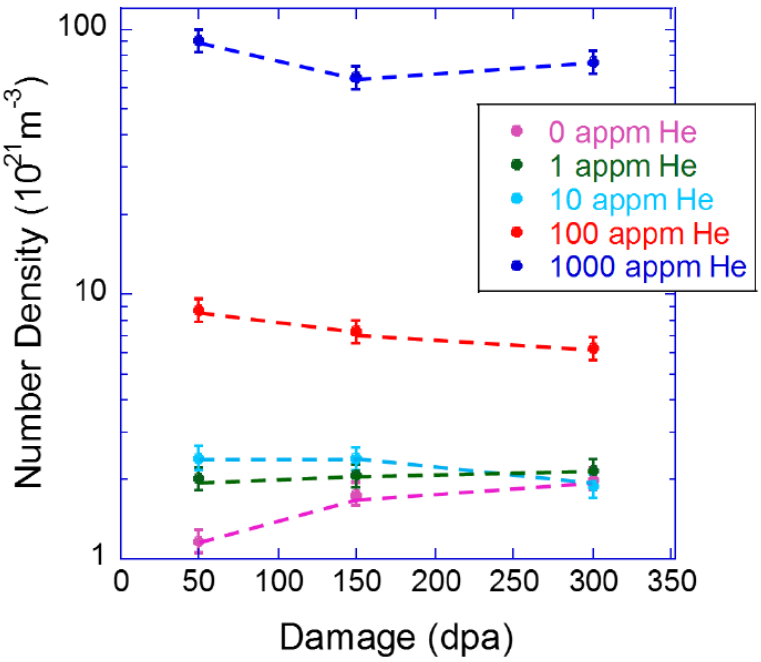

Figure 4.38. Number density (including nanocavities) as a function of damage is shown for the alumina-coated T91 C2269:460°C condition.

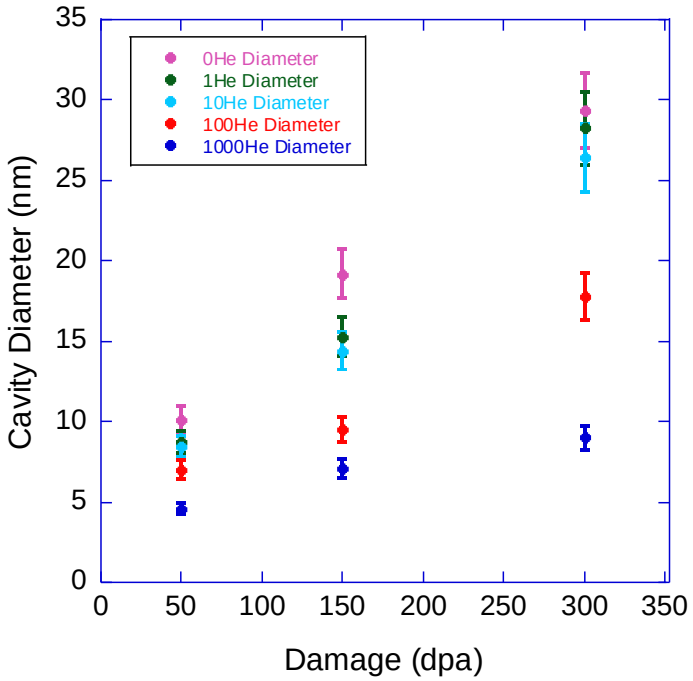

Figure 4.39. Number density (including nanocavities) as a function of damage is shown for the alumina-coated T91 C2269:460°C condition.

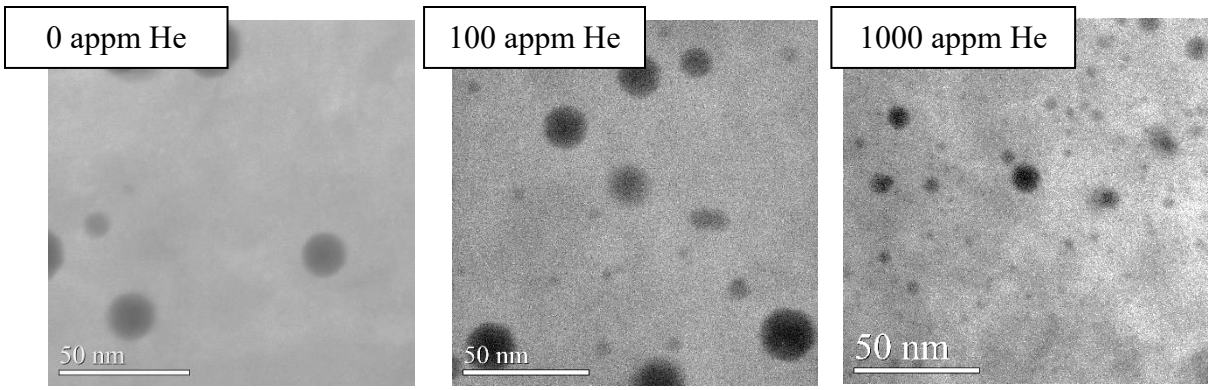

Figure 4.40. 1Mx magnification HAADF images reveal a significant density of nanocavities in the 100 and 1000 appm He conditions.

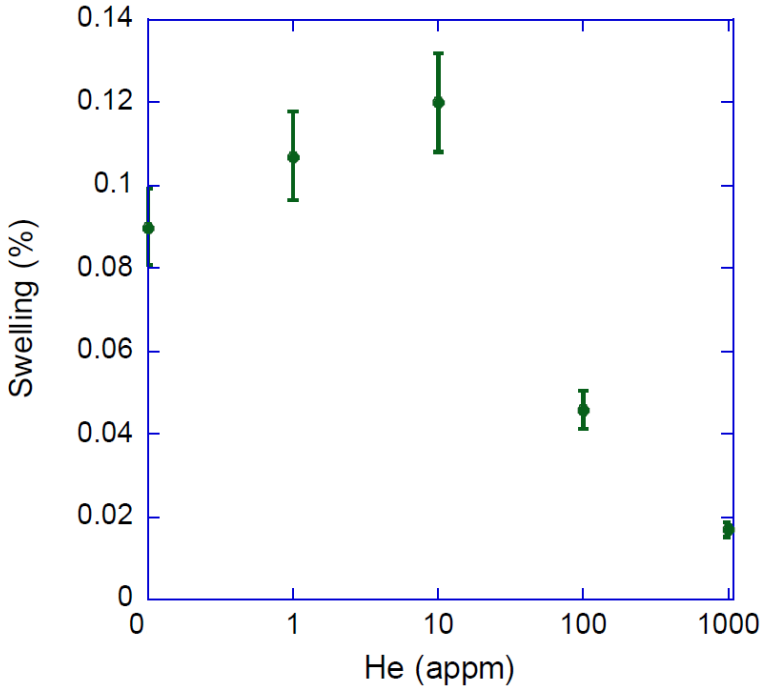

Figure 4.41. Swelling shows a peaked behavior in the coated samples only at 50 dpa.

4.6 Swelling suppression due to carbon uptake during ion irradiation

To demonstrate this effect of carbon uptake on swelling, irradiations up to 300 dpa were performed using both alumina-coated (carbon uptake prevented) and bare (with carbon uptake) T91 heat C2269 implanted with 10 appm He. A considerable difference in the swelling behavior was observed (see BF STEM images in Figure 4.42). The coated sample resulted in much higher

density of cavities than the bare sample that was subject to carbon uptake ($18.9 \times 10^{20} m^{-3}$ vs. $13.2 \times 10^{20} m^{-3}$). Additionally, there were no observable Cr_2C carbides in the sample with the coating, while a high density appeared in the bare sample. A comparison of the swelling, number density, and diameter at a variety of helium levels is shown in Figure 4.43-Figure 4.45. Figure 4.43 shows the dependence on swelling as a function of helium for the bare and coated samples at 300 dpa. The bare samples show a peaked behavior of swelling, with the maximum swelling occurring at about 10 appm He. However, the coated samples show a drop off with swelling, with the maximum occurring at 0 appm He and only falling with further additions of helium. Suppression of cavity density, size and swelling was observed at all helium levels, even though the effect of carbon at high helium level appears to be minimal. Figure 4.46 shows swelling as a function of irradiation dose in the bare sample. Compared to the coated sample (Figure 4.37), it is clear that lower swelling was evident in the bare sample across the dose range.

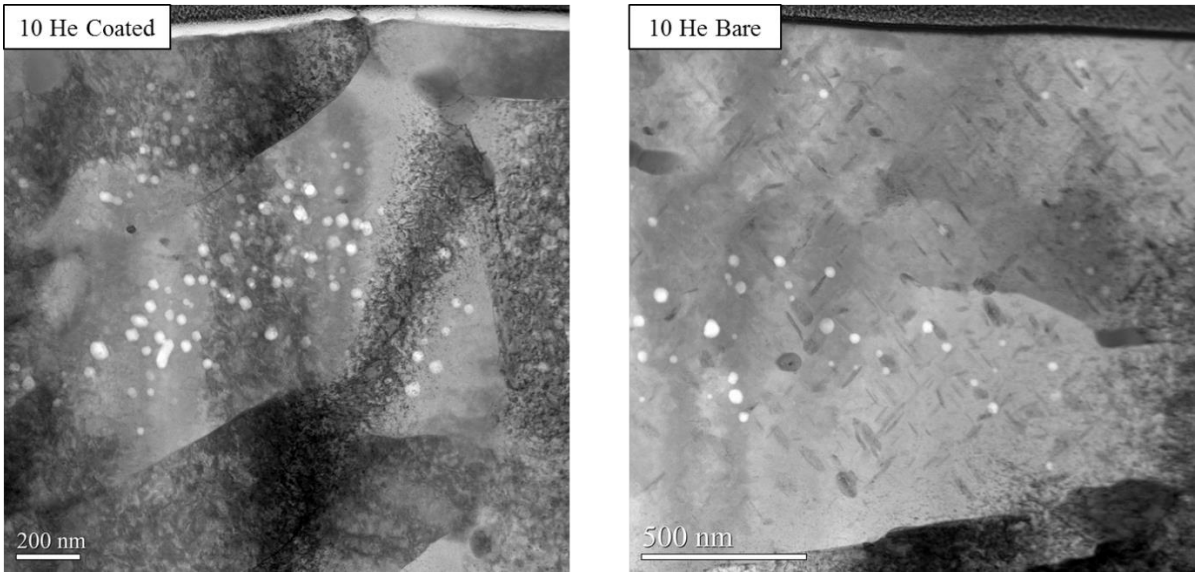

Figure 4.42. Bright field STEM images of T91 C2269 at 300 dpa, implanted with 10He in both the coated and bare condition. Many carbides and lower density of cavities are observed in the bare condition.

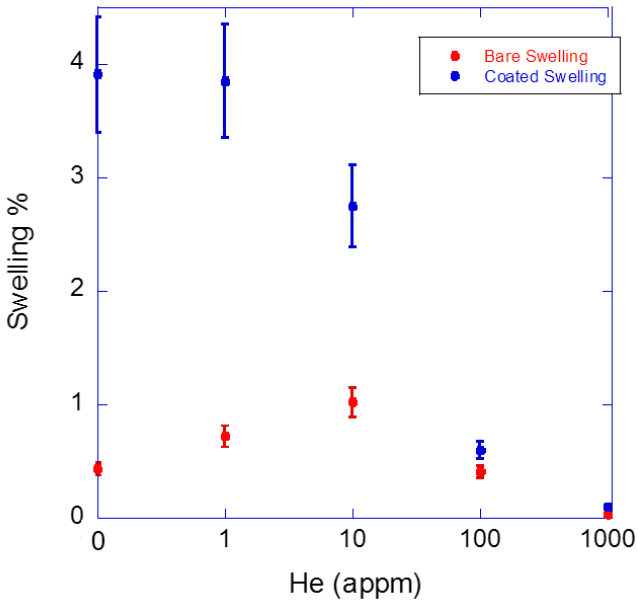

Figure 4.43. Swelling is plotted with increasing helium level for both the bare and coated T91 samples at 300 dpa:460°C.

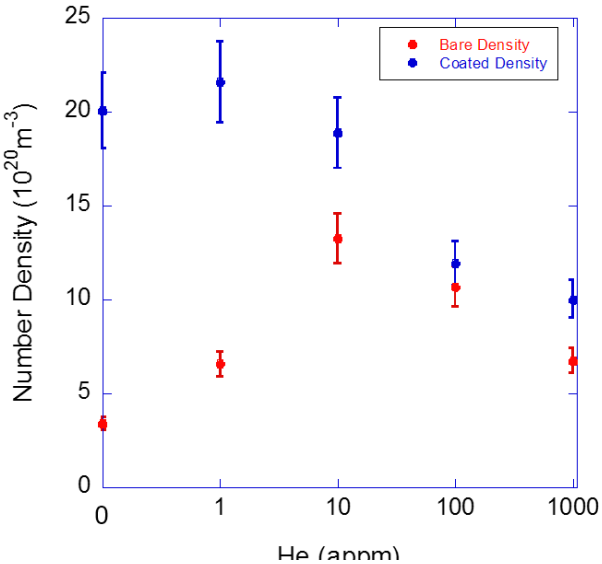

Figure 4.44. Number Density (not including nanocavities) is plotted with increasing helium level for both the bare and coated T91 samples at 300 dpa:460°C.

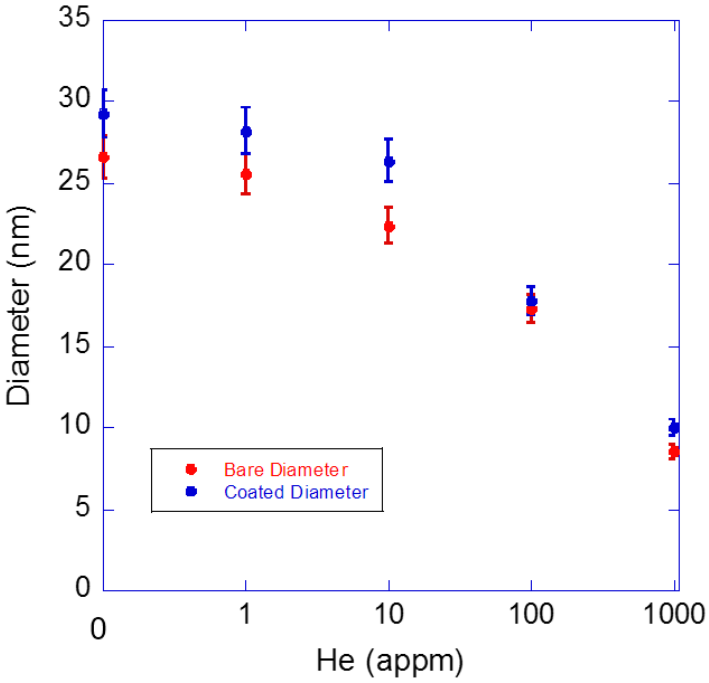

Figure 4.45. Cavity diameter is plotted with increasing helium level for both the bare and coated T91 samples at 300 dpa:460°C.

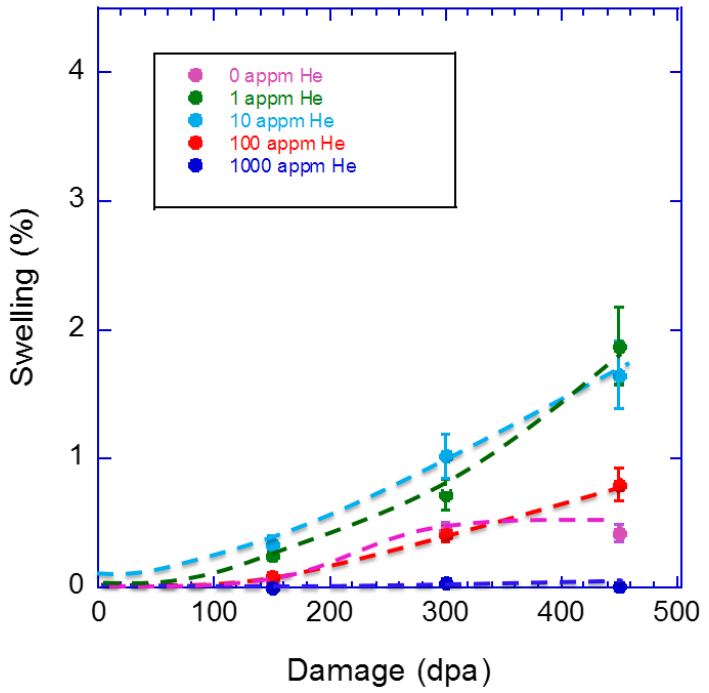

Figure 4.46. Swelling as a function of damage is shown for the bare T91 C2269:460°C condition

References:

4.1 L. Singer, “Absorption of carbon from residual gases during Ti implantation of alloys,” Appl. Phys. Lett., vol. 43, no. 5, p. 457, 1983.

4.2 I. L. Singer, “Carburization of steel surfaces during implantation of Ti ions at high fluences” vol. 419, 1983.

4.3 Vaumousse D, Cerezo A, Warren PJ, Court SA. An atom probe study of fine scale structure in AlMgSi(Cu) alloys. Aluminum Alloys 2002: Their Physical and Mechanical Properties Pts 1-3 396-4 (2002) 693.

4.4 Marquis EA. Core/shell structures of oxygen-rich nanofeatures in oxide-dispersion strengthened Fe-Cr alloys. Applied Physics Letters 93 (2008).

4.5 Williams, C. A., Marquis, E. A., Cerezo, A., & Smith, G. D. (2010). Nanoscale characterisation of ODS–Eurofer 97 steel: An atom-probe tomography study. *Journal of Nuclear Materials*, *400*(1), 37-45.

5. Modelling of Swelling in a Simulated F-M Alloy

The temperature that maximizes swelling rate will be a focus of this effort, because it synthesizes a large amount of information on cavity nucleation into a single useful measure. Temperature's strong control over the density of stable cavities effectively modifies the sink strength ratio given by

$$(5.1)\quad Q_{\mathrm{i,v}} = \frac{\rho_{\mathrm{d}} Z_{\mathrm{i,v}} D_{\mathrm{i,v}}}{4\pi \overline{r_{\mathrm{V}}} N_{\mathrm{V}} D_{\mathrm{i,v}}}$$

where *D*'s denote defect diffusion coefficients, ρ_d is dislocation density per unit volume, *Z*'s are capture efficiencies for each defect type, $\overline{r_V}$ is the mean cavity radius, and N_V is the number density of cavities. At temperatures above the peak, cavities are thermally unstable, and dissociation impedes the formation of a significant density, increasing *Q*. Below the peak, cavities are so stable that they almost never dissociate, resulting in large densities of small clusters that act as powerful recombination sites, decreasing *Q*. Between these two extremes lies a window of stability where a density is sustained that can compete with biased sinks to drive a net flux of vacancies to the cavity. This parity where *Q* =1 constitutes the optimal swelling condition.

The fundamental theoretical framework for understanding these phenomena is mean field rate theory (MFRT) and the void growth equation. In its simplest form, MFRT predicts the fate of non-equilibrium defects with only two differential equations that describe how vacancies and interstitials partition between recombination and competing defect sinks. These rates are described by solving the diffusion equation in an effective, lossy medium to generate concentration-independent rate constants [5.1]. These point defect balance equations are given by

$$(5.2)\quad \frac{dC_v}{dt} = G - R_{iv} C_v C_i - K_v C_v ,$$

and

$$(5.3)\quad \frac{dC_i}{dt} = G - R_{iv} C_v C_i - K_i C_i ,$$

where v and i subscripts denote vacancies and self-interstitials, G denotes Frenkel pair generation rate, and *C*'s denote concentration of defects per unit volume. $R_{iv} = 4\pi r_{iv}(D_i + D_v)$ is the recombination constant and r_{iv} is the recombination radius. *K*'s are the total sink strength for each defect type. The total sink strength is the sum of dislocation and cavity absorption according to $K_i = \rho_d Z_i D_i + 4\pi \overline{r_V} N_V D_i$ and its vacancy analogue.

Cluster dynamics models are the intuitive logical extension of the classical MFRT, but instead of only two rate equations (one for each defect type), a cluster dynamics approach requires an intricate network of interconnected differential equations for each allowed cluster size. For a given species *j*, the concentration is governed by

$$(5.4)\quad \frac{dC_j}{dt} = G_j + R_j(C) - \rho_d Z_j D_j C_j ,$$

where $R_j(C_j)$ is a sum of all possible interaction events

(5.5) $R_j^+(C) = \sum_{n+m\to j} k_{n,m}^+ C_n C_m - \sum_k k_{j,k}^+ C_j C_k$,

and dissociation events

(5.6) $R_j^-(C) = \sum_{n\to n-j,\,j} k_{n-j,\,j}^- C_n - \sum_k k_{j,k}^- C_j$,

which create or consume a species *j*, where *k*'s are unique rate constants encapsulating the kinetics of each reaction. This approach, while significantly more complex, allows the simplifying assumptions inherent to Mansur's correlation, most notably a static number density and the mean size approximation, to be relaxed.

While the cluster dynamics framework promises more accurate quantitative knowledge of how defects (and impurities) diffuse and aggregate in a material, the rate constants governing the system behavior are still dependent on input parameter selection. In some cases, experimental techniques like resistivity recovery experiments can be used to provide a direct measurement [5.2]. For many others, atomistic modelling techniques like density functional theory (DFT) and molecular dynamics (MD) are the best options for providing accurate estimates. The parameters of most relevance to ferritic alloys have been curated and are given in Table 5.1.

Table 5.1. Material Parameters used to describe defect evolution.

Parameter	**Value**
Dislocation Density [m^{-2}]	3×10^{14}
Grain Diameter [m]	1×10^{-6}
Helium Generation Rate [appm/dpa]	0.2
Di-vacancy Binding Energy [eV]	0.3
Vacancy Formation Energy [eV]	1.79
Vacancy Migration Energy [eV]	0.63
Interstitial Migration Energy [eV]	0.22
Helium Migration Energy [eV]	0.07
Vac. Diffusion Pre-exponential [m^2/s]	8.2×10^{-7}
Int. Diffusion Pre-exponential [m^2/s]	1.1×10^{-7}
He Diffusion Pre-exponential [m^2/s]	4×10^{-7}
Dislocation Bias for Interstitials	1%

The cluster dynamics framework accommodates the addition of second dimension to this system of equations to describe each cavity's helium content. Each rate equation for a cluster is replete with capture and emission terms as function of size. Capture reactions are directly proportional to radius and diffusivity, but emission terms take on an additional Arrhenius dependence on some binding energy. Each binding energy is a sum of contributions to stability provided by vacancies and helium atoms. Vacancies enhance stability as size is increased, asymptotically

approaching the formation energy according to capillarity. For very small cluster sizes where capillarity breaks down (entering a negative energy space), ab initio binding energies are available, starting with the least stable divacancy at 0.3 eV. The stabilizing helium pressure inside the bubble is approximated using a hard sphere equation of state and added to the vacancy contribution. These, along with other critical quantities were compiled from ab initio data for α-iron and experimental measurements into a reasonable parameter set (Table 5.1). Additionally, a single 3-dimensionally mobile interstitial equation was used to capture recombination and defect partitioning in a simple, memory-conserving manner.

Stochastic and deterministic cluster dynamics methods have been used to analyze radiation phenomena such as bubble formation, loop nucleation and growth, and precipitation [5.3–5.7]. However, existing cluster dynamics work attempting to compensate for dose rate has been confined to very low temperatures and doses due to memory limitations imposed by the large number of equations necessitated by the treatment of three clustering species (interstitials, vacancies, and helium gas atoms). This work reduces these to a computationally manageable level using a moment-based scheme that groups larger clusters such that the concentration of defects is conserved [5.8,5.9], allowing the high dose swelling behavior to be assessed. Even with the grouping scheme in place, the helium-vacancy space is very large such that a robust treatment of dislocation loops and their glide results in a model which is too memory intensive. Instead loop nucleation is replaced by a single three-dimensionally mobile interstitial equation, and a fixed dislocation network with a reasonable density of 3×10^{14} m^{-2}. Experimental experience suggest that even over the course of as much as 650 dpa, the dislocation density is unlikely to change by more than about a factor of two [5.10].

5.1. Implementation of a Simple Frenkel Pair Model

Beginning with the simplest form of such a model, and most comparable to the invariance relations, temperature distributions were generated for both fast reactor and heavy ion beam relevant dose rates (Figure 5.1). The resulting distributions exhibit peak swelling temperatures at 140˚C and 240˚C for neutron and ion dose rates respectively. These temperature peaks both manifest well below all experimental data, indicating that this preliminary model underpredicts the temperature at which void densities are optimal for growth. Size and density information (Figure 5.2) complicates this picture, as even though the low peak temperatures suggest low stability, void densities overpredict experiment by about an order of magnitude.

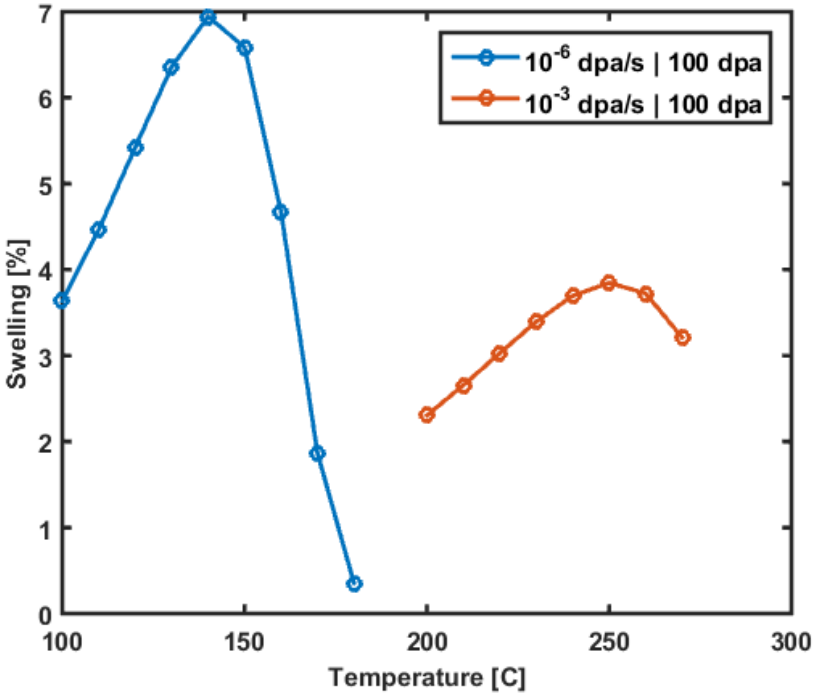

Figure 5.1. Initial temperature distributions of swelling at 100 dpa under reactor and ion beam relevant dose rates using Frenkel pair damage.

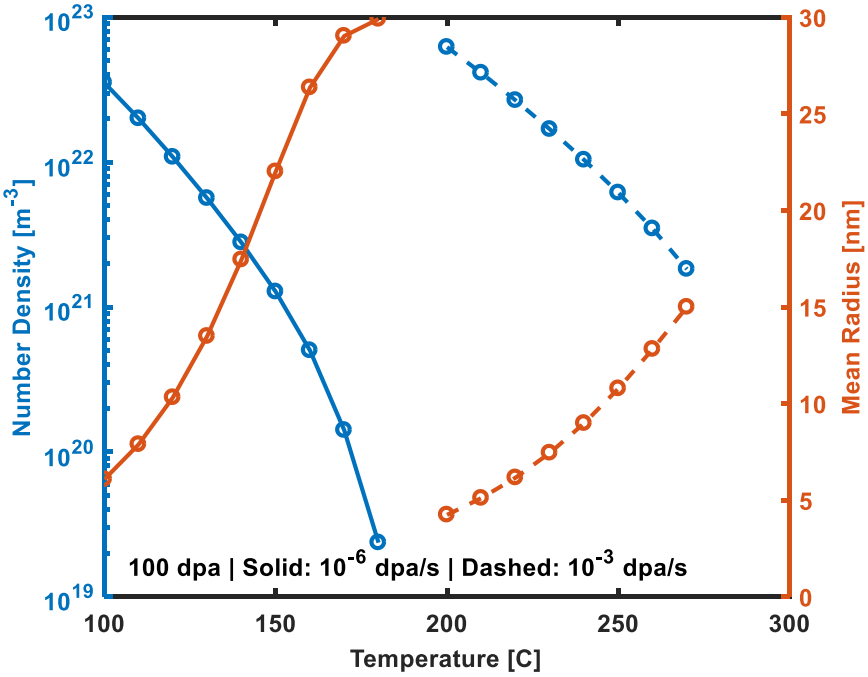

Figure 5.2. Cavity density and mean radius at reactor and ion beam relevant dose rates using Frenkel pair damage.

In addition to the peaks presented in Figure

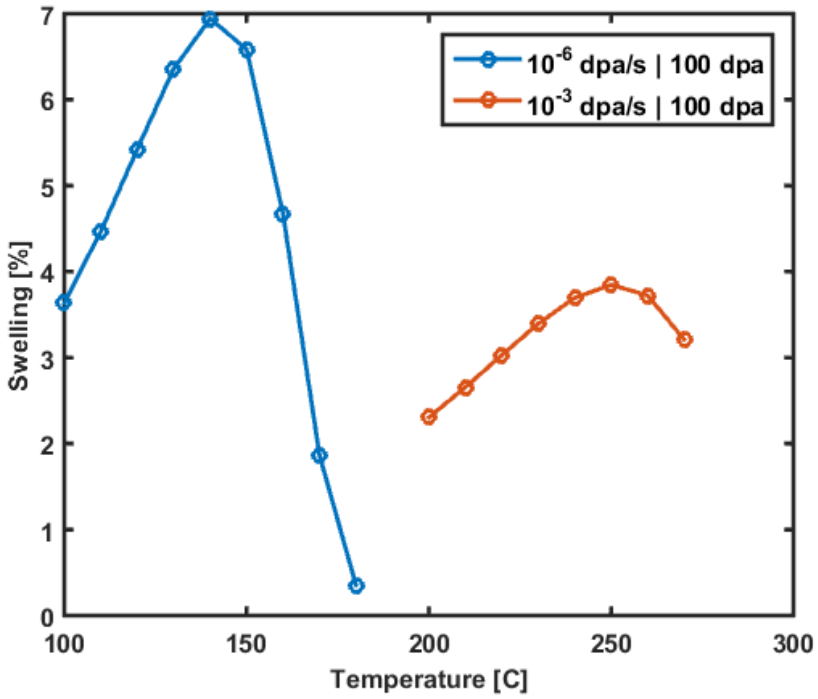

5.1

, a suite of calculations varying the parameters most intuitively connected to swelling behavior were performed. Establishing bounds of reasonability and making justifiable adjustments to these parameters is the simplest way to improve agreement. The most notable parameters in consideration for changes are cavity binding energy, vacancy mobility, dislocation bias, and unbiased sink strengths. Temperature peaks generated from these small changes are provided in Figure 5.3.

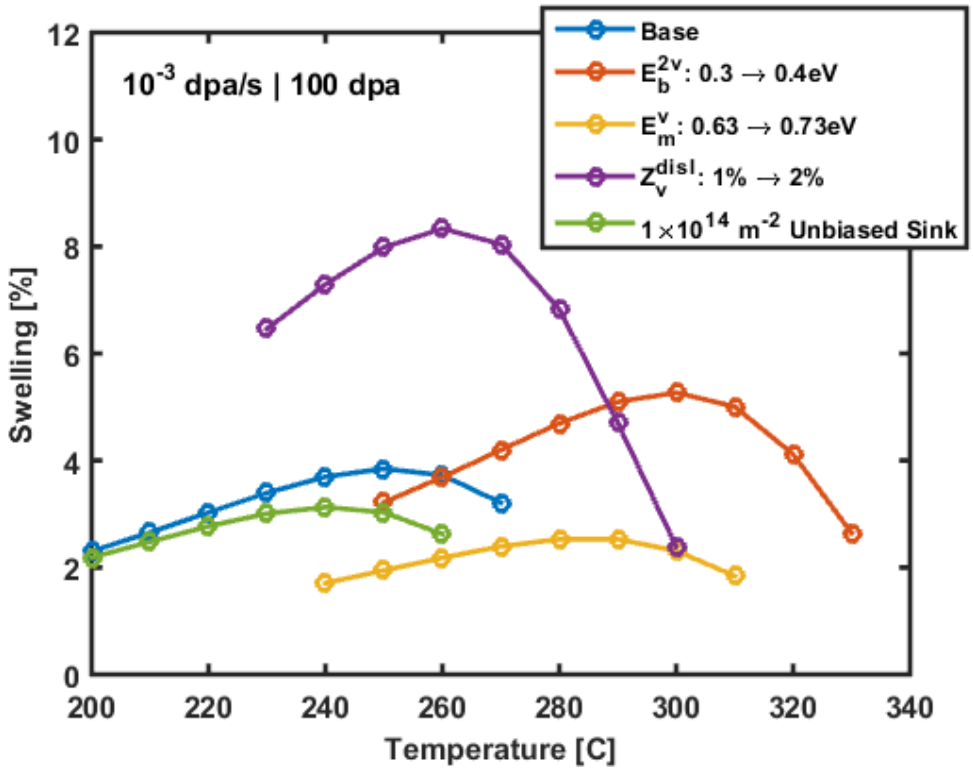

Figure 5.3. Ion-irradiated temperature distributions of swelling at 100 dpa with small variations in key material parameters.

Both vacancy migration and surface energy modifications show the ability to shift the location of temperature peaks. Unfortunately, they are incapable of addressing the large discrepancy with experiment without assuming values unreasonably out of line with measurement. Some may argue that a sufficient increase in vacancy migration could be justified by interactions with solute atoms, but it will be described in a later section that this treatment is flawed. Also, peaks tend to shift in tandem, providing no redress to the overestimate of temperature shift. Dislocation bias and unbiased sink additions exert secondary control over

5.2. Addition of Cascade Damage and Helium Cogeneration

The inadequacy of the simple Frenkel pair model motivated the addition of a more complex primary damage formation. Decades of molecular dynamics simulations of high PKA energy damage events have demonstrated their propensity to form defect clusters directly in cascades [5.11,5.12]. This can be folded into a PKA distribution from SRIM [5.13,5.14] or SPECTER calculations to generate a vector of defect cluster production terms. Two such vectors were created (Figure 5.4), one with a maximum of 9-vacancy and 20-vacancy clusters produced. The 9-vacancy maximum is representative of the direct result of an MD cascade in iron. The 20-vacancy maximum is based on a similar cascade in which the spatial correlation of the damage event promotes coalescence beyond that which would be adequately described by defects evenly distributed throughout a mean field. These larger clusters climb up the capillarity curve, making them more stable against thermal emission, and acting as preferred cavity nucleation sites. The result is temperature distributions (Figure 5.5) with peaks much closer to the experimentally

observed peaks at 420-460˚C, particularly in the ion-relevant case. The shift in temperature, however, remains much larger than the experimentally observed 20-60˚C.

In a further effort to compensate for the apparent underprediction of cavity stability, the full two-dimensional helium-vacancy system was utilized with a constant helium generation rate of 0.2 appmHe/dpa. The result as shown in Figure 5.5b was an almost negligible change in swelling. Only the least stable Frenkel Pair case showed any discernable change, and even then, only in swelling rates rather than peak locations. It seems that the stabilizing effect of vacancy clustering in primary damage overwhelms any effects of helium. This runs contrary to the wide body of experimental evidence for a stabilizing effect of helium which greatly enhances swelling, primarily by shortening incubation periods.

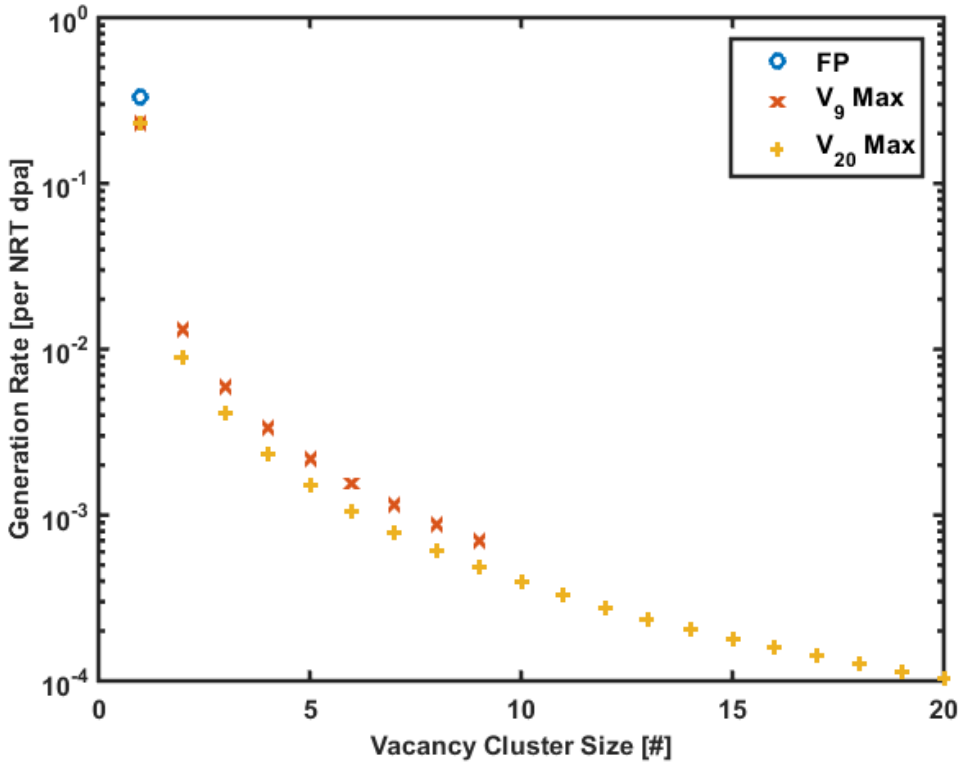

Figure 5.4. Vacancy cluster distributions used in cascade primary damage formulation as compared to Frenkel pair treatment.

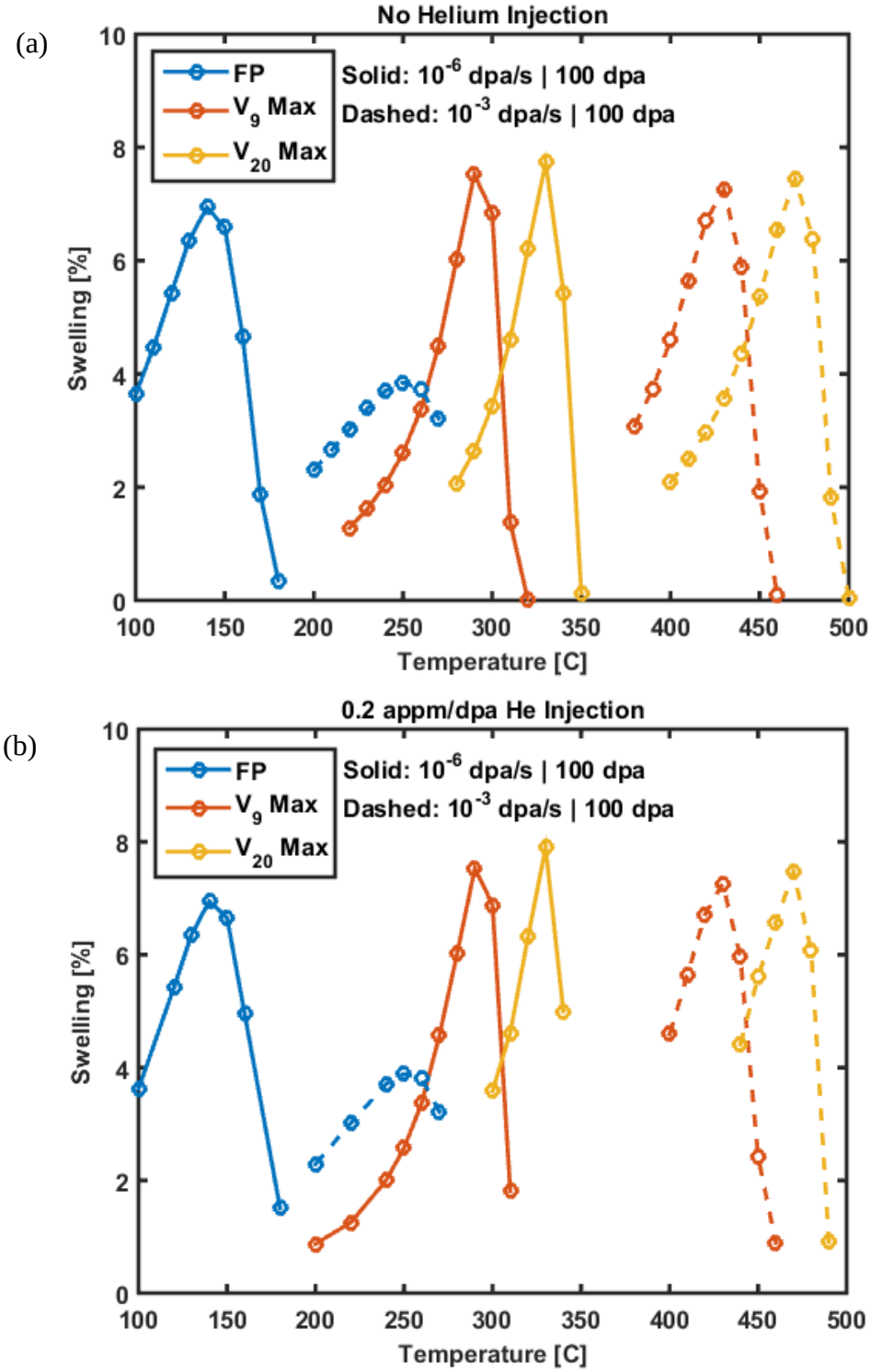

Figure 5.5. Temperature distributions of swelling with increasing cascade vacancy cluster production (a) without helium and (b) with cogenerated helium.

Helium is inherently unable to decrease incubation dose in this model, because the model fails to produce one. As shown in Figure 5.6, nucleation occurs rapidly such that a steady-state growth rate is reached within the first few dpa, which is nowhere near the hundreds of dpa observed in many ion irradiation experiments. It seems as though the mechanism impeding nucleation through this incubation is not thermal emission alone. For any reasonable increase in emission parameters, the peak simply shifts to a lower temperature, where the nucleation rate is ideally balanced against the dislocation network. Previous rate theory based modelling approaches are either consistent with this lack of incubation, or require an artificial prohibition of vacancy accumulation until a certain critical helium pressure is achieved, or unrealistically large swings in dislocation density [5.15–5.17]. If the underlying defect production and transport are to be trusted, the desired results should fall out of them naturally rather than through prescription.

Another concern raised by Figure 5.6 is that a 1% dislocation bias used to obtain reasonable linear swelling rates, and swelling exhibits an extremely high sensitivity to bias. Experimental evidence and atomistic calculations suggest that the interstitial bias of edge dislocations lies somewhere between 10-50% [5.18,5.19]. Recent work suggests screw dislocations may have vanishingly small preferences for interstitials, or even a slight preference for vacancies [5.19]. Dislocation loop nucleation is expected to generate substantial edge dislocation line length within 1-2 dpa, which is almost instant relative to swelling. Even in a case where all dislocations were screw type at the outset of irradiation, some effective bias higher than 1% would be expected.

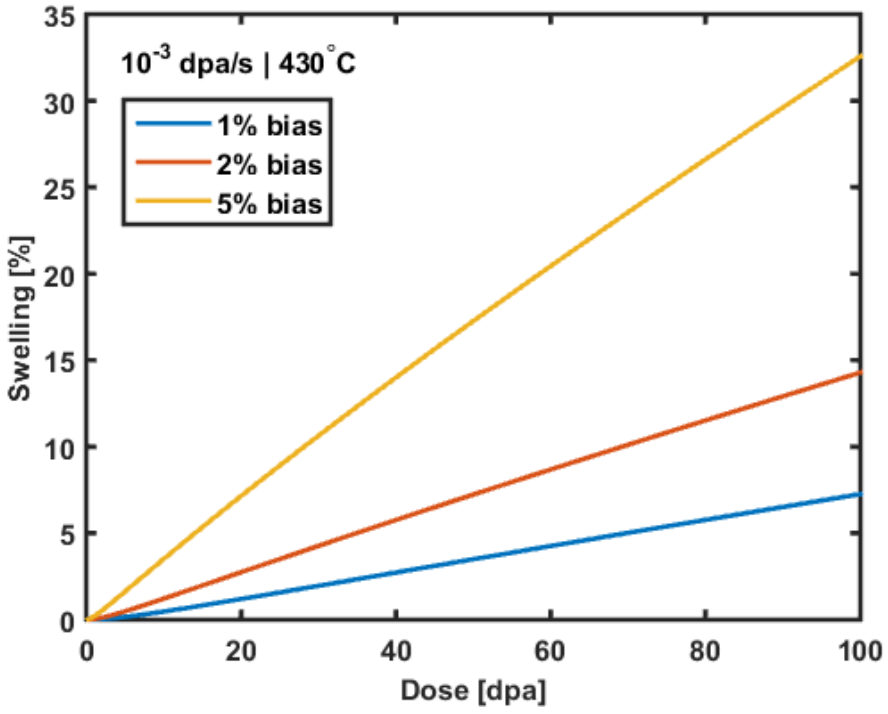

Figure 5.6. Swelling as a function of dose at assorted low dislocation biases for interstitials.

The difference in peak swelling temperature between the two dose rate conditions is much larger than experimentally observed. While the ion case peaks in an appropriate temperature range, the

reactor-relevant case manifests at temperatures well below where any neutron-irradiated ferritic steels have observed any swelling. A comparison was made to the temperature shift predicted by Eq. (5.6), modified such that instead of the simple sum of migration and formation energy, the effective energy

$$(5.7)\quad E = E_m^v + E_v^f + \Omega\left(p - \frac{2\gamma}{r}\right),$$

which has been slightly modified to use the vacancy binding energy of the largest, most stable, injected cluster rather than an infinite void (Table 5.2). This cluster dynamics approach is aligned with classical rate theory in predictions of temperature shift. Therefore, the assumptions used in the theoretical Mansur expressions hold up to scrutiny from a more rigorous cluster dynamics treatment in this case. The distinction between these large shifts and the smaller ones observed experimentally causes concern that the dominant mechanisms are being missed by each treatment.

Table 5.2. A comparison of model-generated peak swelling temperature shifts between ion and neutron dose rates with analytical predictions of Mansur

Damage Mode	**γ [J/m^2]**	**Model ΔT [K] (±10)**	**Computed Mansur ΔT [K]**
Frenkel Pair	1.7	110	106.7
	2.0	100	104.4
V_9 Max. Cascade	1.7	140	146.8
	2.0	120	142.1
V_{20} Max. Cascade	1.7	140	151.0
	2.0	140	141.4

5.3 Effect of helium pre-implantation in swelling

As in the actual ion irradiation experiments, the model was used to pre-implant various levels of helium into the material. The key pre-implantation parameters are outlined in Table 5.3. The resulting cavity distribution as a result of pre-implantation to levels of 1, 10, 100, and 1000 appm He are shown. According to the model, at 1000 appm, bubbles of ~1nm should form. It is apparent that the swelling is slightly higher than is observed experimentally. This is likely due to the fact that nucleation is occurring much more quickly in the model than experimentally. Little to no incubation dose is observed in the swelling behavior, and a high density of cavities is observed in the void distributions.

The case of 0-He has been added to the others. Previously it was difficult to nucleate voids without helium. Two options were explored to increase the stability of clusters created without helium: increasing the divacancy binding energies, and increasing the size of the input damage. Both methods may result in significant swelling with no helium present, however the more physically relevant change is an increase in the initial cluster size. Previously, the damage was simply input as the creation of Frenkel pairs. A more realistic case for ion damage would include a distribution of cluster sizes. Maximum cluster sizes from 9 vacancies to 20 vacancies were explored. Of those, measurable swelling was observed at 14 vacancies. An intermediate value was chosen at 16 vacancies. The results are plotted in Figure 5.7 along with runs containing helium. All of the pre-implanted cases were redone with the cluster size of 16, however only slight changes in their swelling behavior were observed. It appears that in the case where helium

is pre-implanted, the amount of helium dominates over the form of damage. Helium pre-implantation appears to have a peaked behavior with swelling rate. That is, a maximum in swelling occurs at intermediate helium values (10 appm He), while dropping off at high helium (100 and 1000 appm), and lower helium (0 and 1 appm). In the high helium cases, this is due to a dilution of defects among a substantial density of small cavity sinks. In the lower helium cases, the reduced density due to lower levels of pre-implantation cause an overall lower swelling rate.

Table 5.3. The key input parameters for helium preimplantation and subsequent irradiation

Parameter	**Preimplantation**	**Irradiation**
Irradiation Time [s]	$3\times10^{1\leftrightarrow4}$	1×10^{5}
NRT Damage Rate [dpa/s]	8×10^{-7}	1×10^{-3}
Helium Generation Rate [He/atom/s]	3.33×10^{-8}	0
Temperature [C]	25	460

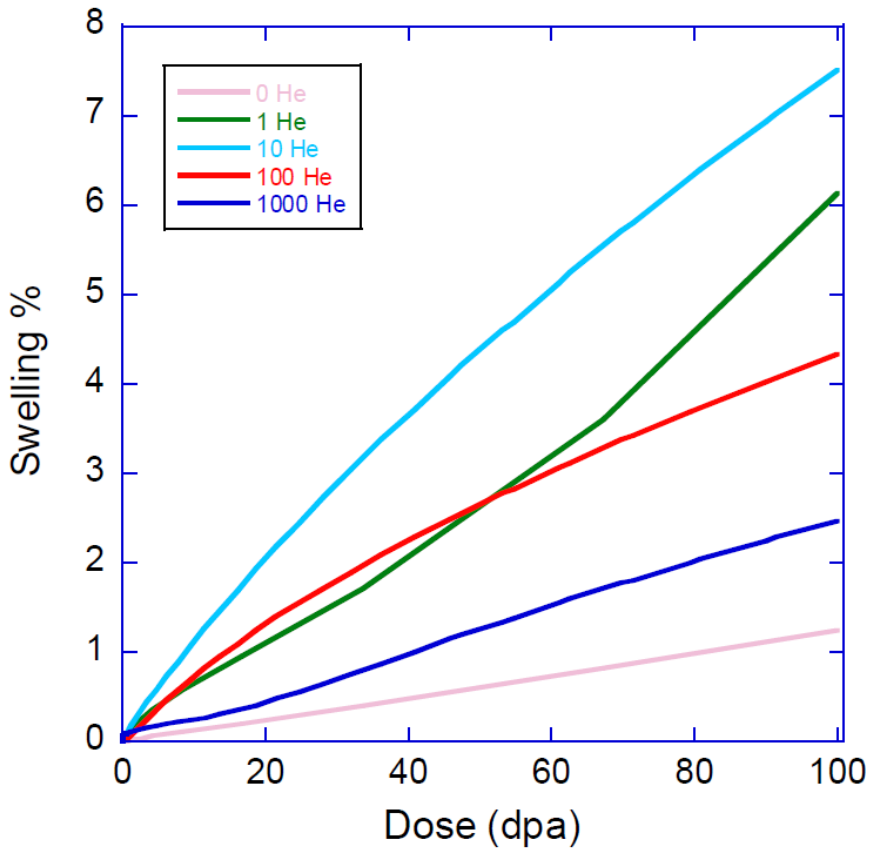

Figure 5.7. The size distributions of cavities for various levels of helium pre-implantation from the model are shown.

5.4. Carbon-Vacancy interactions:

Initially, upward shifts in these peaks toward the region of interest were accomplished by increasing the vacancy migration energy. This strategy was able to produce the desired result with increases of only about a tenth of an eV in the ion case (Figure 5.8). A departure from ab initio and desorption data, must be physically justified using an argument of impurity interactions. Since the emission rate constant is proportional to the capture rate, the reduction in peak height associated with a reduction in net vacancy flux is therefore accompanied by a strong upward shift in peak swelling temperature. This creates an artificial increase in cavity stability which falsely implies that each nucleating cluster is associated with an impurity.

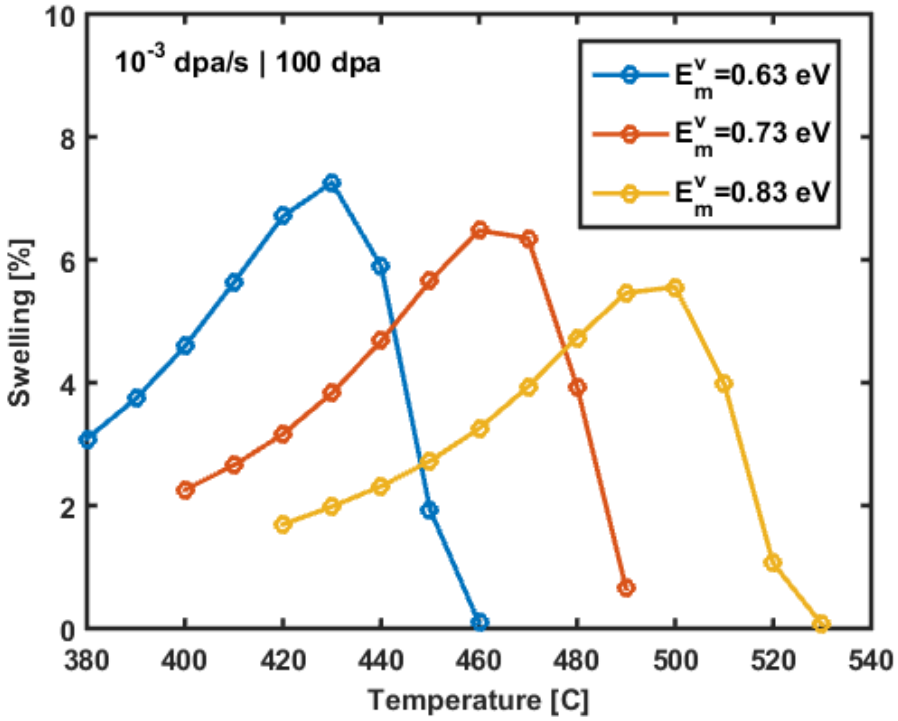

Figure 5.8. Swelling temperature distributions with small increases in vacancy migration energy.

Atomistic modelling efforts have recently computed the stabilities of these immobile complexes formed by vacancies and impurities (predominantly carbon) [5.20]. In an effort to remove the residual stability effects of the effective diffusion approach, these binding energies were utilized to determine the strength of this effect directly by including a new reaction pair for formation and dissociation of a vacancy-carbon complex. A static density of sessile carbon atoms was introduced with an input binding energy informing the stability of complexes. The resulting temperature distributions show that the primary effects are a reduction in void growth rate, and a small decrease in effective stability indicated by a small downward temperature shift (Figure 5.9). At the most likely condition, which assumes 200 appm of dissolved carbon and uses the binding energy of a V-C complex, the effect is modest. However, pushing to higher-than-expected carbon solubility or binding energies at the magnitude of V-C_2 complexes increases the capability to retard swelling in a significant way.

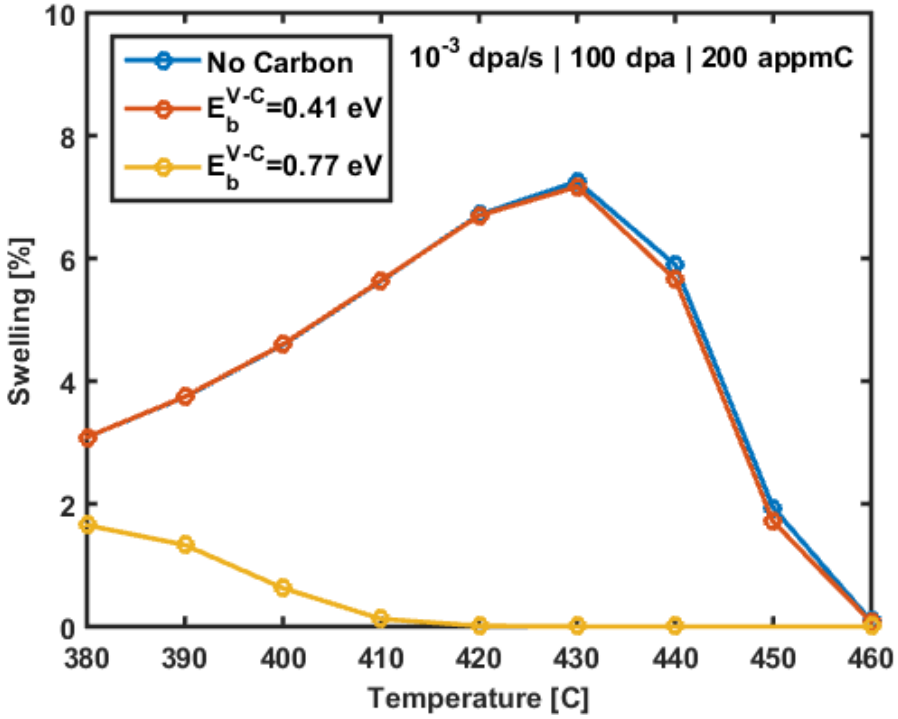

Figure 5.9. Swelling temperature distributions at the ion relevant case demonstrating the effect of carbon-vacancy complex formation with limiting monomer binding energies.

For a more rigorous treatment of these interactions, an equation was added to provide mobility to small vacancy clusters and carbon solutes [5.21], and by allowing accumulation of immobile V-C clusters up to size V_4C_2 using binding energies from ab initio calculations and simple extrapolation [5.20] (Table 5.4). The results in Figure 5.10 indicate that the primary effect of vacancy cluster mobility is to provide a small boost to net vacancy flux to cavities which slightly raises the peaks magnitude. When naturally formed through carbon accumulation, the more tightly bound complexes with two carbon atoms are not formed in densities sufficient to significantly impede cavity nucleation. The secondary nature of this effect clearly indicates that it is not the dominant physical phenomenon responsible for the incubation period. The effects of carbon on swelling are most likely relegated to the formation and coarsening of carbides which act as unbiased sinks [5.22].

Table 5.4. Vacancy and Carbon Mobilities, as well as binding energies of carbon atoms to assorted species of VxCy complexes

Species	E_m **[eV]**	D_0 **[m^2/s]**	$E_b^{V_xC}$ **[eV]**	$E_b^{V_xC_2}$ **[eV]**
V	0.63	8.2×10^{-7}	0.41	0.77
V_2	0.62	8.2×10^{-7} / 2	0.63	0.68
V_3	0.35	8.2×10^{-7} / 3	0.63	0.68
V_4	0.48	8.2×10^{-7} / 4	0.63	0.68
C	0.86	1.4×10^{-7}		

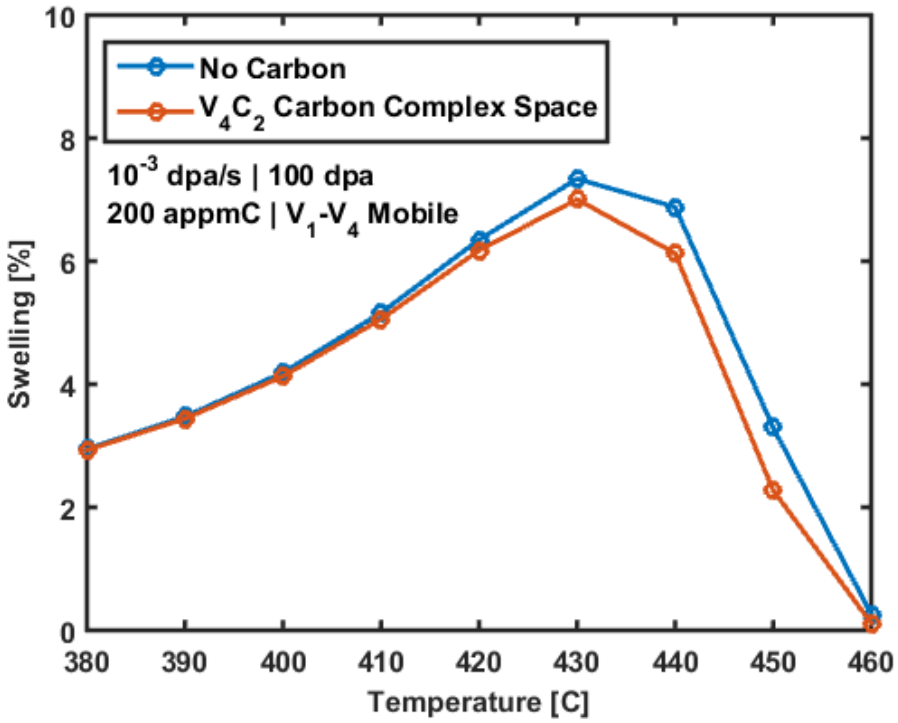

Figure 5.10. Swelling temperature distributions where clusters of up to 4 vacancies are mobile and can form complexes with up to 2 carbon solute atoms

5.5 Remaining issues

Agreement between Mansur's invariance relations and the more analytically rigorous cluster dynamics treatment indicates that they are valid for cases where homogeneous nucleation is the dominant mechanism. There is outstanding disagreement between these results and experiment, namely,

- Linear swelling rates are far higher than observed unless a very small dislocation bias for interstitials is used.
- Helium has a negligible effect on cavity nucleation at generation rates of experimental relevance, as opposed to experiments where it is observed to greatly increase cavity density and shorten incubation periods.
- Long incubations periods are effectively absent, with linear swelling being reached in only 1-2 dpa.
- Helium pre-implantation results in a peak of swelling rate at an intermediate implantation level.
- Dose rate effects are much stronger than observed, with test-reactor-relevant damage creating peaks around 300˚C, well below any experimental measurements.

Reasonable parameter variations, and the addition of impurity interactions with energetics around 0.5 eV, are incapable of rectifying these discrepancies. Currently neglected mechanisms seem to be dominant in ferritic systems, one of which acts as a powerful impediment to cavity nucleation at all temperatures until a sufficient quantity of helium is present to stabilize them, and another which weakens the temperature dependence of the cavity density, perhaps by providing a preferred site for heterogeneous nucleation which is independent of temperature and dose rate.

References:

5.1 A.D. Brailsford, R. Bullough, M.R. Hayns, J. Nucl. Mater. 60 (1976) 246–256.

5.2 D. Terentyev, P. Olsson, T.P.C. Klaver, L. Malerba, Comput. Mater. Sci. 43 (2008) 1183–1192.

5.3 A.A. Kohnert, B.D. Wirth, J. Appl. Phys. 117 (2015) 154306.

5.4 A.A. Kohnert, B.D. Wirth, J. Appl. Phys. 117 (2015) 154305.

5.5 A.Y. Dunn, L. Capolungo, E. Martinez, M. Cherkaoui, J. Nucl. Mater. 443 (2013) 128–139.

5.6 A. Dunn, B. Muntifering, R. Dingreville, K. Hattar, L. Capolungo, J. Nucl. Mater. 480 (2016) 129–137.

5.7 D. Xu, G. VanCoevering, B.D. Wirth, Comput. Mater. Sci. 114 (2016) 47–53.

5.8 S.I. Golubov, A.M. Ovcharenko, a. V. Barashev, B.N. Singh, Philos. Mag. 81 (2001) 643–658.

5.9 A.A. Kohnert, B.D. Wirth, Model. Simul. Mater. Sci. Eng. 25 (2017).

5.10 E. Getto, K. Sun, A.M. Monterrosa, Z. Jiao, M.J. Hackett, G.S. Was, J. Nucl. Mater. 480 (2016) 159–176.

5.11 R.E. Stoller, J. Nucl. Mater. 276 (2000) 22–32.

5.12 D.J. Bacon, F. Gao, Y.N. Osetsky, J. Nucl. Mater. 276 (2000) 1–12.

5.13 J.F. Ziegler, M.D. Ziegler, J.P. Biersack, Nucl. Instruments Methods Phys. Res. Sect. B Beam Interact. with Mater. Atoms 268 (2010) 1818–1823.

5.14 R.E. Stoller, M.B. Toloczko, G.S. Was, A.G. Certain, S. Dwaraknath, F.A. Garner, Nucl. Instruments Methods Phys. Res. Sect. B Beam Interact. with Mater. Atoms 310 (2013) 75–80.

5.15 N.M. Ghoniem, G.L. Kulcinski, J. Nucl. Mater. 82 (1979) 392–402.

5.16 M.P. Surh, J.B. Sturgeon, W.G. Wolfer, J. Nucl. Mater. 328 (2004) 107–114.

5.17 R.E. Stoller, G.R. Odette, ASTM Spec. Tech. Publ. 955 (1987) 371–392.

5.18 T. Okita, W.G. Wolfer, J. Nucl. Mater. 327 (2004) 130–139.

5.19 Z. Chang, D. Terentyev, N. Sandberg, K. Samuelsson, P. Olsson, J. Nucl. Mater. 461 (2015) 221–229.

5.20 C.J. Ortiz, M.J. Caturla, C.C. Fu, F. Willaime, Phys. Rev. B 80 (2009) 134109.

5.21 K. Tapasa, a. V. Barashev, D.J. Bacon, Y.N. Osetsky, Acta Mater. 55 (2007) 1–11.

5.22 E. Getto, G. Vancoevering, G.S. Was, J. Nucl. Mater. 484 (2016).

6. Discussion

6.1 Dose dependence of swelling in F-M alloys

Dose dependence of swelling in HT9, T91 and NF616 were examined at 460°C with 10 appm helium pre-implantation. Irradiations were performed at damage levels of 75 dpa, 188 dpa, 375 dpa. Additionally, alloy HT9 was irradiated at 140 dpa, 250 dpa, 350 dpa and 450 dpa as part of TerraPower irradiation program conducted at University of Michigan [6.1]. As shown in Figure 6.1, no welling was observed in either of the alloys, indicating that the incubation dose for significant swelling in the three F-M alloys is greater than 75 dpa. Voids were overserved in HT9 irradiated at 140 dpa but significant swelling was not observed until 188 dpa. A nearly linear swelling rate was observed after 188 dpa. A swelling-dose curve typically has three characteristic regimes – cavity incubation regime, transition regime and cavity linear swelling (or steady-state swelling) regime. In the incubation regime, cavities are in the form of nucleus or sub-nanometer features that can not be easily resolved by conventional TEM. Cavities are observable in TEM after reaching the incubation dose and both cavity size and density increase slowly with dose in the transition regime. The swelling rate in the transition regime is typically small. In the cavity linear swelling regime, swelling is dominated by cavity growth with a swelling rate much higher than that in the transition regime.

Both HT9 and T91 showed very similar swelling behavior through 375 dpa at 460°C. A linear swelling rate of about 0.03%/dpa was observed in both the T91 and HT9 samples. Irradiation to higher dose of 650 dpa [6.1] did not change the swelling rate significantly in HT9. At 188 dpa, T91 exhibited a swelling of 3.15% in 10 appm He condition while HT9 exhibited swelling values of 2.9%. By 375 dpa, swelling in T91 grew to 9.5% for 10 appm He, while HT9 experienced 8.4% swelling. Over this large range of doses, the swelling values for the two ferritic-martensitic alloys were very similar. It appeared that T91 may have swelled slightly more than HT9 at the damage levels considered, however the values are within the experimental error of each other, so no significant difference can be claimed. Alloy NF616 shows lower swelling rate at ~0.015%/dpa, about half of that for T91 and HT9.

Swelling rate in ion irradiated F-M alloys varied significantly in the literature. Smidt et al. [6.2] irradiated HT9 and EM12 steel with 2.8 MeV Fe+ ions up to 250 dpa at 500°C and alloys were preimplanted with 1 appm He. The linear swelling rate was calculated to be 0.017%/dpa for HT9 and 0.011%/dpa for EM12. Toloczko et al. [6.3] examined swelling in Cr^{3+} -irradiated HT9 up to 600 dpa at 450°C. The authors determined that steady state/linear swelling in HT9 was not reached until approximately 400-600 dpa and the swelling rate was determined to be approximately 0.2%/dpa. It is interesting though the swelling for HT9 at 400 dpa was ~10%, which is very comparable to our study (8.4% at 375 dpa). The swelling rate was ~0.03%/dpa if only dose range of 200-400 dpa was considered. It was hypothesized that there exist an ultimate swelling rate of 0.2%/dpa for F-M alloys [6.4]. If this is the case, the alloys might be still in the transition regime as the swelling rate is still an order of magnitude lower than 0.2%/dpa. Whether it will reach the ultimate swelling rate at much high doses (>650 dpa) is unknown but it would be beyond the life dose limits of fast reactors (say, ~600 dpa the most). The actual swelling rate in the dose range of interest would be important for the application of the materials. The swelling rate can be affected by a number of factors, including alloys and heats and it can

also be affected by pre-implanted helium levels and irradiation temperatures. These two will be discussed in the next sections.

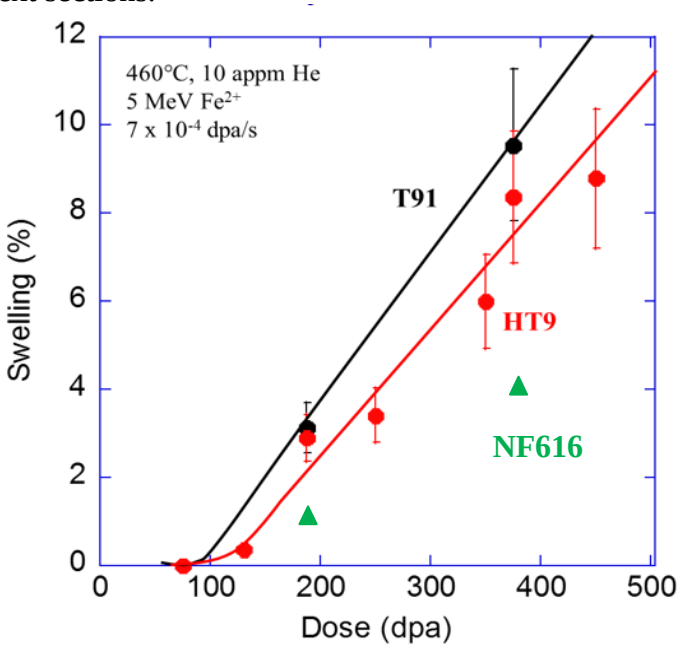

Figure 6.1. The swelling behavior of T91 and HT9 implanted with 10 appm He, irradiated up to 375 dpa is shown.

6.2 Helium effect on swelling

The effect of helium on swelling in HT9 can be seen in Figure 6.2. At lower damage levels of 75 dpa (see the magnified dose range in the insert), the maximum of swelling occurs at 100 appm He while negligible swelling observed for the 1 and 10 appm He cases. As helium promotes cavity nucleation, nucleation dominates the swelling behavior at the dose. Only 1 and 10 appm helium were studied at higher doses. At high doses, 10 appm case not only shows higher swelling values but also higher linear swelling rate compared to the 1 appm helium case. Figure 6.3 show the comparison of void size and density for the two different helium levels. There is virtually no different in the average void size but the number density of voids is significantly higher in the 10 appm helium case. Therefore, the higher swelling and swelling rate in 10 appm helium is mainly due to the higher number of voids nucleated. With higher levels of helium, the onset of measurable swelling is pushed to lower doses. Higher helium levels result in an earlier onset of growth: linear swelling was achieved ~50 dpa earlier at 10 appm He compared to 1 appm He in HT9. Additionally, it appears that the amount of pre-implanted helium may as well affect the steady-state swelling rate. A lower steady-state swelling rate of 0.009%/dpa in 1 appm helium was observed compared to 0.03%/dpa in 10 appm He.

In the case of T91, 10 appm helium shows highest swelling at low dose of 50 dpa. After further irradiation, the swelling behavior in the 0 appm He case eventually overtook that of the pre-implanted cases as growth began to dominate. The 100 appm and 1000 appm helium show low swelling and swelling rate even at high dose. It is likely that further additions of helium only serve to boost the nucleation at the cost of growth at higher damage levels. This behavior

suggests that the nucleation of the 0 appm He case took place over hundreds of dpa, rather than the tens of dpa in the pre-implanted cases. While the nucleation was slower for the 0 appm He case, it appeared that this allowed the cavities which did nucleate to grow uninhibited.

In general, higher levels of helium produce a higher density of voids. When the helium is very high (say >100appm). Suppression of growth occurs due to a substantial void sink density at high helium levels. When suppression of growth does not occur (in the case of 1 and 10 appm helium), higher helium levels increase the swelling rate.

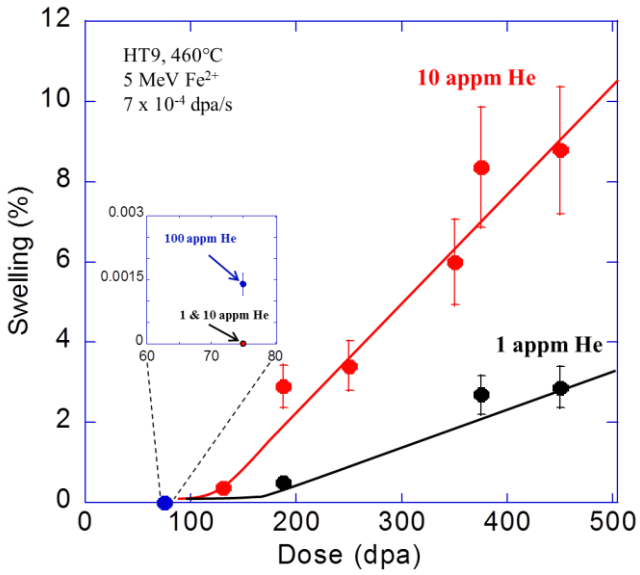

Figure 6.2. Helium effect on swelling rate in HT9 irradiated at 460°C.

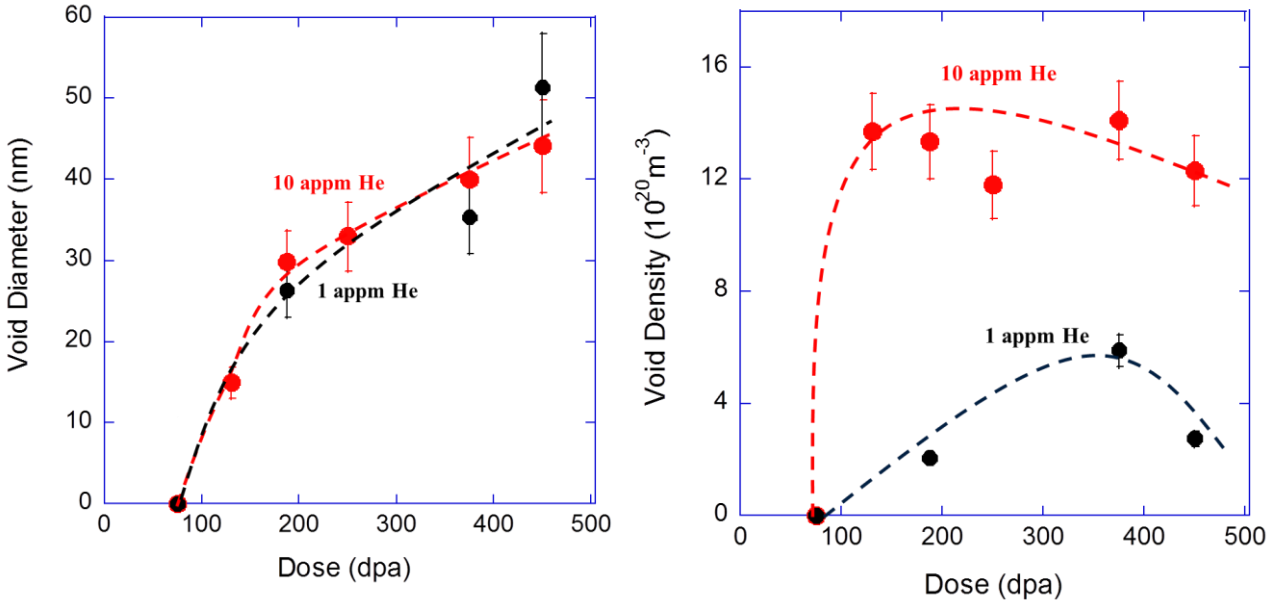

Figure 6.3. Helium effect on void size (left) and density (right) in Fe^{++} irradiated HT9 at different doses.

6.3 Temperature shift for F-M alloys

To compensate the high production rate of interstitials and vacancies (therefore, the recombination rate) at high dose rate, a temperature shift to higher temperature is required for self-ion irradiations to match microstructures of low dose rate reactor irradiations. To determine the temperature shift, it is necessary to understand the dependence of swelling on irradiation temperatures. In this project, self-ion irradiations were conducted at 400, 420, 440 and 460°C to explore the effect of temperature on swelling. In addition, irradiation was conducted at 480°C as part of other project at the University of Michigan [6.1]. Temperature dependence of swelling was therefore evaluated in the temperature range of 400-480°C. For the 400°C irradiation up to 250 dpa, none of the four alloys (T91, HT9, NF616 and 14YWT) showed void swelling. At 420°C:150 dpa, no voids were observed in either of the alloys. A very low amount of swelling, with only a few cavities (see Table 4.2 and Table 4.3) were observed when irradiated at 440°C at 188dpa. A considerable amount of swelling was observed at 460°C — approximately 3% with 10 appm He, and 0.5% with 1 appm He in HT9. At 480°C:188dpa, void swelling again became minimal. The temperature dependence of swelling, number density, and diameter for HT9 at 188 dpa, with 10 appm He implanted is shown in Figure 6.4 and was published in [6.5]. It appeared that 440°C and 480°C were at the ends of the swelling peak. These results suggested that a sharp temperature peak for swelling in ion irradiations occurred near 460°C.

The peak swelling temperature of 460°C is consistent with literature for ion irradiations in F-M alloys. Multiple irradiation experiments [6.2,6.3,6.5,6.7-6.12] have been done to show the temperature dependence of swelling in ion irradiated F-M alloys. Toloczko *et al*. [6.3] performed a study on MA957 tube up to 500 dpa with no pre-injected helium at a variety of temperatures (400ºC, 420ºC, 450ºC, 500ºC). The peak swelling temperature was determined to be near 450ºC at doses of 100 and 500 dpa. Ayrault [6.8] studied the effect of irradiation temperatures above 450°C on a 9Cr-1Mo steel. No swelling peak was found, but the highest swelling occurred at 450ºC. This may suggest that the tail-end of a temperature peak was caught in this study and the peak would appear somewhere close to 450ºC.

Swelling peak in neutron irradiated HT9 was not fully determined due to the limitation of available neutron irradiated conditions. For the HT9 duct material it is impossible to find the same dose at three different tempratures. However, there was minimal swelling at 410°C:100 dpa and 466:92 dpa and much higher swelling at 443C:155dpa. The peak swelling temperature of HT9 in FFTF appears to be ~443ºC. It must be noted that the dose was also highest at this temperature, which make the peak temperature not ultimately determined. From the available neutron data by Gelles [6.14], the swelling peak for neutrons was estimated to be around 440°C. Therefore, the swelling temperature peak for neutron irradiation appears to be around 440°C. This results in a temperature shift of ~20°C for HT9. This is small compared to austenitic steels (>100°C). Mansur [6.13] theorized the existence of this temperature shift due to differences in damage rate between neutron and ion irradiations. For ferritic-martensitic steels, it was supposed that the temperature shift would be small or non-existent due to a high sink density in the material.

The swelling curve is consistent with theory which has shown that swelling follows a bell-curve temperature dependence [6.6]. The existence of swelling peak is mainly due to the fact that void

nucleation rate is strongly dependent on irradiation temperature. At low temperatures, the effective amount of vacancies available to form voids is reduced due to low point defect diffusivities. Vacancies have limited mobility at these temperatures and will recombine with interstitials before clustering into voids. Nucleation of cavities decreases with high temperatures due to a high emission of vacancies. At some optimal intermediate temperature there is a maximum swelling where the inward vacancy flux is largest compared to the vacancy emission.

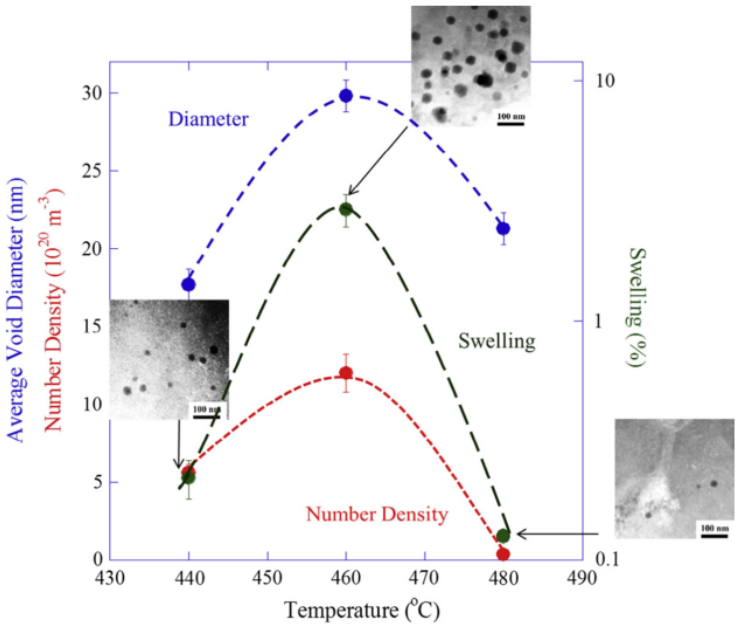

Figure 6.4. The temperature dependence of swelling, number density, and diameter for HT9 at 188 dpa, with 10 appm He implanted.

6.4. Benchmarking with reactor irradiation

Based on the temperature shift and the effect of helium on swelling, Fe^{++} irradiation at 460°C:188dpa with 1 appm pre-injected helium was selected to compare with FFTF-irradiation at 443°C:155dpa. The detailed comparison was published in [6.15]. Qualitatively, dislocation loops, voids and G-phase that were observed in FFTF irradiated HT9 were also generated by Fe^{++} irradiation. A quantitative comparison including the volume fraction of swelling and precipitates and the total loop line length for the ion irradiation relative to reactor irradiation is shown in Figure 6.5a. A comparison of defect size and number density as a ratio of ion irradiation to reactor irradiation is shown in Figure 6.5b. The void swelling is nearly identical between the two irradiations, and the size and density of precipitates and loops following ion irradiation are within a factor of two of those for reactor irradiation. A factor of two is a reasonable agreement considering the level of confidence in the damage level and temperature of the reactor irradiation. The ACO-3 duct was in reactor for a total of 7 cycles consisting of 26 segments during which it resided in 4 different locations in the FFTF reactor core over the period 8/17/85-3/19/92 [6.15]. As a result, it was subjected to variations in the neutron flux spectrum and temperature between cycles, resulting in a complicated damage-temperature history and an

unknown level of uncertainty in the reported dose and temperature. Available data indicates that the temperature experienced by this duct over its lifetime may range between 40-50°C. It is well known that irradiated microstructures can be quite sensitive to the damage rate-temperature history of the reactor and that start-ups and shut-downs can introduce complexity in the irradiated microstructure not seen when both are fixed for the entire irradiation. Kiratani et al. [6.17] showed that both the dislocation and void microstructures of Ni-base alloys could vary by factors of up to 2x in size and 20x in number density just by varying the temperature during reactor startup and shutdown. Due to uncertainty in the neutron irradiation conditions, additional efforts to refine the ion irradiation conditions are probably not warranted. Rather, experiments are under way to generate reactor data in a more controlled fashion on a range of model and commercial alloys to improve the fidelity of the comparison with, and the validation of ion irradiation as an effective tool for emulation of reactor irradiation [6.18]. In fact, commercial reactor components will always undergo complicated damage rate-temperature histories during their operation. Due to the much higher degree of control over the irradiation processes in an ion irradiation, the challenge for increasing the fidelity of the emulation then becomes one of capturing the effects of damage rate-temperature variations in-reactor.

The self-ion and neutron microstructure comparison results confirmed that the reactor-irradiated microstructure can be emulated by ion irradiation with only a modest temperature increment (17°C) in HT9. The damage increment (33 dpa) over the reactor irradiation is also small. These results indicate that an Fe^{++} irradiation at 460°C with pre-injection of 1 appm He closely emulates the irradiated microstructure, both qualitatively and quantitatively, created by fast reactor irradiation at an average temperature of 443°C and to a similar damage level.

The temperature shift for T91 seems to be higher than 20°C. In the neutron irradiated sample, there was 1.6% of swelling after irradiation to 184 dpa at 413°C (Table 3.1). There was no swelling in self-ion irradiated T91 at 420°C up to 200 dpa with 10 appm helium pre-implantation. Swelling was 3.15% after irradiation to 188 dpa at 460°C. The swelling is much more comparable with neutron irradiation when irradiated at 460°C. In addition the average void size was within statistical errors (29 nm by neutron vs. 28 nm by self-ions) and the number density is about 2 times higher in self ion irradiated samples. The temperature shift appears to be ~50°C for T91.

It is likely that there is no universal temperature shift for F-M alloys. Just as the variation in swelling which is dependent on alloys, heat, pre-existing microstructures, etc., the temperature shift may also depend on those factors. Particularly, the pre-existing and radiation-induced microstructures (defect sinks) can be a critical factor for temperature. As indicated by Mansurs's analysis, high density sinks would result in smaller temperature shift. Compared to T91, HT9 has higher carbon content (0.21% vs 0.08%) and higher Ni and Si content (Table 2.1). Sinks due to carbides and radiation-induced Ni/Si precipitates in HT9 are expected to be much higher than T91, which may result in smaller temperature shift. However, further study is needed to verify this.

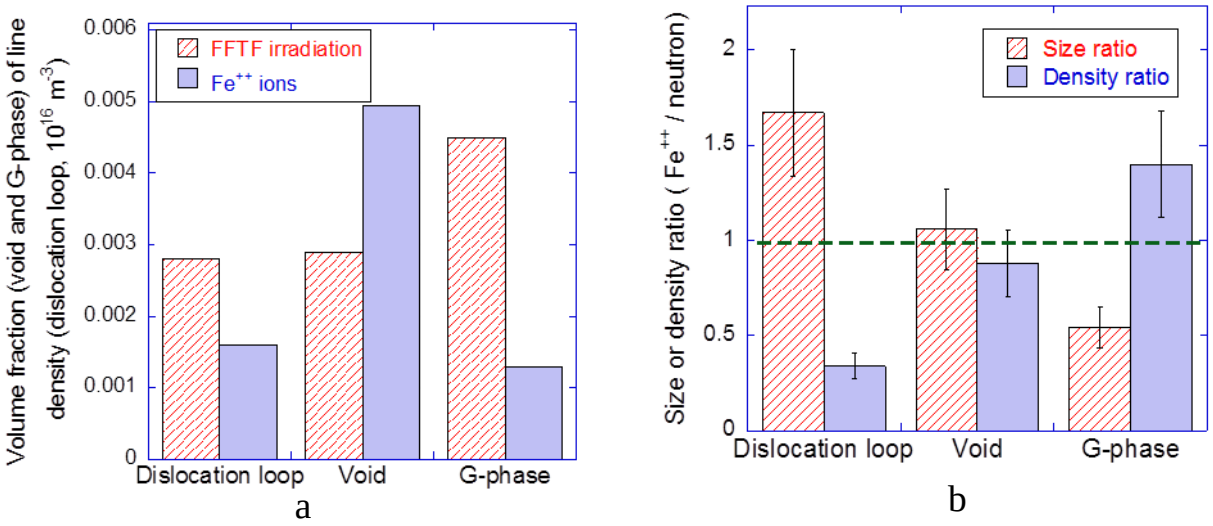

Figure 6.5. Comparison of (a) volume (voids, precipitates) fraction or line density (loops), and (b) size and number density ratios for ion and neutron irradiation of ACO3 under similar conditions.

6.5 Carbon effect on swelling

It is clear that ion-induced carbon uptake in the samples played a significant role in suppressing the nucleation of cavities, and thus the swelling was sequestered as well. This project provided the first concrete evidence of this potentially compromising phenomenon occurring in ion-beam laboratories around the world, and also provided a solution to the problem using alumina coating.

As shown in Figure 4.43-Figure 4.45, T91 with (bare sample) and without (coated sample) carbon uptake showed different trends with helium—likely caused by the presence or absence of carbon and Cr_2C carbides. The difference in swelling is mostly significant at low helium levels. Suppression of swelling is still noticeable at high helium level (100 and 1000 appm) but is much less than low helium cases. Overall the effect of carbon's suppression on swelling in the bare samples is very apparent as the total swelling achieved by 450 dpa in the bare samples for any given helium level does not exceed that of the coated samples by 300 dpa. Furthermore, the 0 appm He bare sample did not show an increase in swelling when going from 300 to 450 dpa—further showing the deleterious effect on swelling that carbon can have over the course of achieving high damage levels.

While the behavior in the carbon-uptake samples was not intended, it may shed some light on microstructures which are very resistant to nucleation. Based on these results, it appears that excess carbon due to carbon uptake may efficiently suppress void nucleation and growth thus result in swelling resistance. Ultimately, this is an important finding when considering swelling resistant alloy design for reactor concepts in high helium environments.

References:

6.1 E. Getto, The Co-evolution of Microstructure Features in Self-ion Irradiated HT(at Very High Damage Levels, Ph.D. thesis, University of Michigan, 2016
6.2 P. Schmidt, P. R. Malmberg, J. a. Sprague, and J. E. Westmoreland, "Swelling Behavior of Commercial Ferritic Alloys, EM-12 and HT-9, as Assessed by Heavy Ion Bombardment," Irradiat. Eff. Microstruct. Prop. Met., p. 227, 1976.
6.3 M. B. Toloczko, F. Garner, V. N. Voyevodin, V. V. Bryk, O. V. Borodin, V. V. Mel'Nychenko, and a. S. Kalchenko, "Ion-induced swelling of ODS ferritic alloy MA957 tubing to 500 dpa," J. Nucl. Mater., vol. 453, no. 1–3, pp. 323–333, 2014.
6.4 F. Garner, M. . Toloczko, and B. . Sencer, "Comparison of swelling and irradiation creep behavior of fcc-austenitic and bcc-ferritic/martensitic alloys at high neutron exposure," J. Nucl. Mater., vol. 276, no. 1–3, pp. 123–142, Jan. 2000.
6.5 E. Getto, Z. Jiao, A. M. Monterrosa, K. Sun, and G. S. Was, "Effect of pre-implanted helium on void swelling evolution in self-ion irradiated HT9," *J. Nucl. Mater.*, vol. 462, pp. 458–469, 2015.
6.6 G. S. Was, Fundamentals of Radiation Materials Science: Metals and Alloys. Springer, 2007.
6.7 A. Dvoriashin, S. . Porollo, Y. . Konobeev, and F. A. Garner, "Influence of high dose neutron irradiation on microstructure of EP-450 ferritic–martensitic steel irradiated in three Russian fast reactors," J. Nucl. Mater., vol. 329–333, pp. 319–323, Aug. 2004.
6.8 G. Ayrault, "Cavity Formation During Single and Dual-Ion Irradiation in a 9Cr-1Mo Ferritic Alloy," J. Nucl. Mater., vol. 114, pp. 34–40, 1983.
6.9 R. Hide, K. Kusanagi, and M. Taguchi, "Microstructural Change in Ferritic Steels Under Heavy Ion Irradiation," Eff. Radiat. Mater. 14th Int. Symp. ASTM STP 1046, pp. 61–72, 1989.
6.10 J. J. Kai and G. L. Kulcinski, "14 MeV nickel-ion irradiated HT-9 ferritic steel with and without helium pre-implantation," J. Nucl. Mater., vol. 175, no. 3, pp. 237–243, 1990.
6.11 B. H. Sencer, J. R. Kennedy, J. I. Cole, S. a. Maloy, and F. a. Garner, "Microstructural stability of an HT-9 fuel assembly duct irradiated in FFTF," J. Nucl. Mater., vol. 414, no. 2, pp. 237–242, Jul. 2011.
6.12 E. Wakai, T. Sawai, K. Furuya, a. Naito, T. Aruga, K. Kikuchi, S. Yamashita, S. Ohnuki, S. Yamamoto, H. Naramoto, and S. Jistukawa, "Effect of triple ion beams in ferritic/martensitic steel on swelling behavior," J. Nucl. Mater., vol. 307–311, pp. 278–282, Dec. 2002.
6.13 L. K. Mansur, "Theory of transitions in dose dependence of radiation effects in structural alloys," J. Nucl. Mater., vol. 206, no. 2–3, pp. 306–323, Nov. 1993.
6.14 D. S. Gelles, "Microstructural examination of commercial ferritic alloys at 200 dpa," J. Nucl. Mater., vol. 237, pp. 293–298, 1996.
6.15 G.S. Was; Z. Jiao; E. Getto; K. Sun; A.M. Monterrosa; S.A. Maloy; O. Anderoglu; B.H. Sencer; M. Hackett, Emulation of reactor irradiation damage using ion beams, Scripta Materialia 88(2014)33.
6.16 B. H. Sencer, J. R. Kennedy, J. I. Cole, S. A. Maloy, F. A. Garner, J. Nucl. Mater. 393, 235-241 (2009).
6.17 M. Kiritani, T. Yoshiie, S. Kojima, Y. Satoh, K. Hamada, J. Nucl. Mater. 174, 327-351 (1990).
6.18 U. S. Department of Energy, https://inlportal.inl.gov/portal/server.pt/community/neup_home/600/fy13_irp_awards.

7. Conclusions

Ferritic-martensitic alloys including HT9, T91, NF616 and 14YWT were irradiated up to 450 dpa at a temperature range of 400-480°C using 5 MeV Fe^{++} to investigate their swelling behavior at high damage levels. The effect of irradiation dose, temperature, pre-implanted helium level on swelling behavior was investigated. The temperature shift was determined based on comparison of ion irradiated microstructures with those by neutron irradiation in FFTF. Clusters dynamics modeling was used to investigate the peak swelling temperature and temperature shift for high dose rate ion irradiations. Here is the list of important findings.

- The swelling behavior in the F-M alloys was greatly affected by irradiation temperature. The void swelling peaked at around 460°C in HT9. No cavities were observed in all the alloys when irradiated at 400°C and 420°C. Much lower swelling was observed at 440°C and 480°C. NF616 shows less swelling than T91 and HT9 at 460°C. However, all the three alloys showed relatively low swelling rate. The swelling rate at 460°C up to 450 dpa was in the range of 0.01-0.03 %/dpa, much lower than the hypothesized ultimate swelling rate of 0.2%/dpa.
- G-phase precipitates were found to be the major irradiation-induced phase in HT9 and they were not found to be affected by the implanted helium level. . No significant change of ODS particles was observed in 14YWT after irradiation at 400°C to 250 dpa by atom probe tomography. The oxygen content in the ODS particles appeared to decrease after irradiation to 80 dpa at 420°C. Segregation N, C, and P to grain boundaries were also revealed in 14YWT after ion irradiation.
- The effect of pre-implanted helium on swelling behavior was investigated. 10 appm helium pre-implantation resulted in higher swelling and swelling rate than 1 appm helium pre-implantation in HT9, T91 and NF616 irradiated at 460°C. The higher swelling and swelling rate are mainly due to the higher number of voids nucleated in samples with 10 appm helium pre-implantation. T91 was studied with a broader helium pre-implantation levels (0, 1, 10, 100 and 1000 appm) at 460°C. 10 appm helium initially showed the highest swelling at low dose of 50 dpa but after irradiation to 150 dpa and above the highest swelling shifted to the 0 appm He case. The 100 appm and 1000 appm helium cases show low swelling and swelling rate at all the doses examined. It appeared that suppression of growth occurred at high helium levels due to a substantially increased void sink density.
- Fe^{++} irradiation at 460°C:188 dpa with 1 appm helium yields the best overall microstructure agreement with the FFTF irradiation at 443°C:155 dpa. The temperature shift for ion irradiation to emulate reactor irradiation appears to be ~20°C for HT9. The moderate temperature shift is believed to be linked to the high sink density in F-M alloys.
- Temperature dependent of swelling and temperature shift for high dose rate self-ion irradiations were investigated using cluster dynamics modeling. The experimentally observed peak temperature could not be simulated by implementation of a simple Frenkel pair model. By addition of cascade damage and helium cogeneration, the resulted temperature distributions with peaks were much closer to the experimentally observed peaks at 420-460˚C in the ion-relevant case. The shift in temperature (~150°C), however, remains much larger than the experimentally observed 20-60˚C in F-M alloys.

- The phenomenon of carbon uptake during ion irradiation was discovered. Carbon uptake in the samples played a significant role in suppressing the nucleation of cavities, and thus the swelling was sequestered as well.